PNAS
www.pnas.org

Supplementary Information for

Recombinant *Escherichia coli* as a biofactory for various single- and multi-element nanomaterials

Yoojin Choi, Tae Jung Park, Doh C. Lee, and Sang Yup Lee

Sang Yup Lee and Tae Jung Park
Email: leesy@kaist.ac.kr and tjpark@cau.ac.kr

This PDF file includes:

Materials and Methods
Figs. S1 to S54
Tables S1 to S4
Text S1 to S16
References for SI reference citations

Other supplementary materials for this manuscript include the following:

Datasets S1 to S2

www.pnas.org/cgi/doi/10.1073/pnas.1804543115

SI Appendix Materials and Methods

Bacterial strains and plasmids. All the bacterial strains and plasmids used in this study are listed in *SI Appendix*, Table S1. Primers used in this study are listed in *SI Appendix*, Table S3 and were purchased from Macrogen (Seoul, Korea). All the DNA manipulations including restriction enzyme digestion, ligation and agarose gel electrophoresis followed standard procedures (1). For the construction of plasmids and strains, bacteria routinely grew in Luria-Bertani (LB) broth containing (per liter) 10 g tryptone, 5 g yeast extract and 10 g NaCl or on LB-agar medium containing 1.5% (w/v) agar. Kanamycin (Km; 30 μg ml^{-1}) was added to the medium when required. Polymerase chain reactions (PCRs) were conducted using C1000 Touch^{TM} Thermal Cycler (Bio-Rad, Hercules, CA, USA). Restriction enzymes were purchased from New England Biolabs (Ipswich, MA, USA) or Enzynomics (Daejeon, Korea). To clone the *MT* gene, the DNA fragment encoding bacterial MT corresponding to *PP_3262* gene of *Pseudomonas putida* KT2440 was amplified by PCR using primers P1 and P2 with the genomic DNA of *P. putida* KT2440 as a template. The amplified *MT* gene fragment was digested using *Eco*RI and *Pst*I and was ligated to plasmid pTac15K digested using the same restriction enzymes, resulting in plasmid pYJ-MT (*SI Appendix*, Table S1). To clone the *PCS* gene, the DNA fragment encoding PCS in *Arabidopsis thaliana* ecotype Columbia (leaves) was amplified by PCR using primers P3 and P4 with the cDNA library of *A. thaliana* as a template. The amplified *PCS* gene was digested using *Pst*I and *Sal*I and was ligated to plasmid pTac15K digested using the same restriction enzymes, constructing pYJ-PCS (*SI Appendix*, Table S1). To co-express *MT* and *PCS* genes in a single plasmid, a gene fragment containing *tac* promoter, *MT* gene and *rrnB* terminator in the plasmid pYJ-MT as a template and *tac* promoter and

PCS were ligated using the primers P5 and P6, constructing a co-expression plasmid pYJ-MT-PCS (*SI Appendix*, Table S1). Colonies were selected on LB-agar plates with Km supplemented. Recombinant strains harboring correct plasmid pYJ-MT-PCS were selected by colony PCR and were further confirmed by sequencing.

Induction of MT and PCS expression. Seed culture of the recombinant *E. coli* DH5α harboring pYJ-MT-PCS was prepared in 25-ml test tubes containing 10 ml LB medium supplemented with Km at 37 °C overnight in a rotary shaker with continuous shaking at 200 rpm. One milliliter of overnight culture was transferred to 100 ml of LB medium supplemented with Km in a 250-ml Erlenmeyer flask. Cell growth was monitored by measuring the absorbance at 600 nm (OD_{600}) using Ultrospec 3000 spectrophotometer (Amersham Biosciences, Uppsala, Sweden). When OD_{600} reached about 0.6, the co-expression of MT and PCS in the cells was induced by the adding 0.5 mM of isopropyl β-D-1-thiogalactopyranoside (IPTG; Sigma-Aldrich, St. Louis, MO, USA). The induced cells were further incubated depending on purposes.

Expression of MT and PCS. The expression of MT and PCS was examined with tricine-sodium dodecyl sulfate polyacrylamide gel electrophoresis (SDS-PAGE) (Schägger, 2006). To prepare samples for tricine-SDS-PAGE, *E. coli* DH5α and *E. coli* DH5α harboring pYJ-MT-PCS were incubated in 25-ml tubes containing10 ml of LB medium and Km at 37°C and 200 rpm for 12 h. After seed culture, cells were transferred to a 250 ml flask containing 100 ml of LB medium. When the OD_{600} was reached at 0.6, 0.5 mM, IPTG was added for induction of MT and PCS. After induction of MT and PCs expression, 0.5 mM of Sn

precursor (i.e. $SnCl_2 \cdot 2H_2O$) was added and further incubated for 12 h. Harvested cell pellets were resuspended in 300 µL of lysis buffer (20 mM Tris-HCl pH 8.0, 300 mM NaCl and 5 mM imidazole) in 1.5 ml microcentrifuge tubes to give a final OD_{600} of 1. The resuspended cells were lysed by sonication and boiled at 100°C for 5 min after addition of the loading buffer. The samples were electrophoresed on 16% tricine-SDS-PAGE gel and were analyzed after staining with Coomassie Brilliant Blue R-250 for 60 min at 80 V and for 30 min at 250 V.

***In vivo* synthesis of NMs.** For *in vivo* synthesis of NM, the recombinant *E. coli* DH5α harboring pYJ-MT-PCS induced for MT and PCS co-expression was further cultivated for 1 h and then corresponding precursors (*SI Appendix*, Table S4) were supplemented to the medium at final concentrations of 0.5 mM. After supplementing the precursors, the pH of the culture medium range from 6.3 to 6.5. To exclude any possible impact of different initial pH on NM biosynthesis while minimizing the possible influence on the NM synthesis during pH adjusting procedure with OH^- ions, the pH of the culture medium was standardized to pH 6.5 using 1 M NaOH solution, which requires minimum amount of base. After additional cultivation at 37 °C in a rotary shaker with continuous shaking at 200 rpm for 12 h. The culture medium was centrifuged at 1,290*g* for 15 min at 4 °C to collect the NMs synthesized from the recombinant cells. The supernatant was discarded and the pellet was resuspended in distilled water.

Cell growth of recombinant *E. coli* in the presence of different precursors. Seed culture of the recombinant *E. coli* DH5α harboring pYJ-MT-PCS was prepared by growing cells

in 25 mL test tubes containing 10 mL of LB medium supplemented with Km at 37°C and 200 rpm overnight in a rotary shaker. One mL of overnight culture was transferred to 250 mL flask containing100 mL of LB medium supplemented with Km. Cell growth was monitored by measuring the OD_{600} using UV-vis spectrophotometer. When OD_{600} reached about 0.6, cells were induced with 0.5 mM of IPTG for MT and PCS expression and further cultivated for 1 h. Next, the corresponding precursors (i.e. Ag, Sn, Fe, Ni, Ag/S and Fe/Ni) were supplemented to the medium at a final concentration of 0.5 mM. Cells were cultured at 37°C and 200 rpm for additional 12 h (Fig. S1).

Preparation of cell extract. Recombinant *E. coli* cells were harvested after cultivation by centrifugation at 1,290*g* for 15 min at 4 °C and washed three times with 10 ml each of wash buffer containing (per liter) 181.8 g urea, 11.25 g glycine, 0.37 g ethylenediaminetetraacetic acid and 0.77 g dithiothreitol. The washed pellet was resuspended in distilled water and disrupted by sonication using Vibra-Cell VCX 600 (Sonics & Materials Inc., Newtown, CT, USA) equipped with a titanium probe (13 mm, Sonics and Materials Inc., Newtown, CT, USA). Cell debris was separated and removed by centrifugation at 1,290*g* for 15 min at 4 °C. The soluble proteins in the final cell extract solutions were quantified by the Bio-Rad Protein Assay Kit (Bio-Rad, Hercules, CA, USA) with bovine serum albumin as a standard.

***In vitro* synthesis of NMs**. To prepare cell extract for *in vitro* NM biosynthesis, the recombinant *E. coli* DH5α harboring pYJ-MT-PCS induced for MT and PCS co-expression was further cultivated for 12 h. Cell extract was prepared from the resulting cells. For the

in vitro NM synthesis, various precursors for NM biosynthesis (*SI Appendix*, Table S4) were added at a final concentration of 1 mM into the cell extract diluted with distilled water (protein concentration of 1 mM) in a 50-ml test tubes. The pH of *in vitro* reaction solution was adjusted to 6.5 as same to *in vivo* NM synthesis, using 1 M NaOH solution. The precursors and the cell extract were incubated at 25 °C in a rotary shaker for 12 h with shaking at 200 rpm.

***In vivo* synthesis of crystalline NMs at initial pH 7.5.** To synthesize crystalline NMs *in vivo* at higher initial pH of 7.5, the recombinant *E. coli* DH5α harboring pYJ-MT-PCS induced for MT and PCS co-expression were further cultivated for 1 h with IPTG induction and corresponding precursor (*SI Appendix*, Table S4) was added to a final concentration of 0.5 mM into the culture medium. The pH of culture medium was adjusted to pH 7.5 using 1M NaOH solution. After further cultivation for 12 h, the culture medium was centrifuged at 1,290*g* and 4 °C for 15 min to collect the NMs from the recombinant cells. The supernatant was discarded and the pellet was resuspended in distilled water.

***In vitro* synthesis of crystalline NM at initial pH 7.5.** To synthesize crystalline NM *in vitro* at increase initial pH, the recombinant *E. coli* DH5α harboring pYJ-MT-PCS induced for MT and PCS co-expression was further cultivated for 12 h. Cell extract was prepared from the resulting cells. Corresponding precursor (*SI Appendix*, Table S4) was added at final concentrations of 1 mM into the cell extract diluted with distilled water to its protein concentration of 1 mM in a 50-ml test tubes. The pH of *in vitro* reaction solution was

adjusted to pH 7.5 using 1 M NaOH solution. The precursors and the cell extract were incubated at 25 °C in a rotary shaker for 12 h with shaking at 200 rpm.

***In vivo* and *in vitro* synthesis of crystalline α-Fe_2O_3 NM.** To biosynthesize crystalline α-Fe_2O_3 NM *in vivo*, the recombinant *E. coli* DH5α harboring pYJ-MT-PCS induced for MT and PCS co-expression were further cultivated for 1 h with IPTG induction and the Fe precursor ($FeCl_2 \cdot 6H_2O$) was added to the culture medium (final ion concentration of 0.5 mM). The pH of culture medium was adjusted to pH 6.5 using 1M NaOH solution. After further cultivation at 37 °C in a rotary shaker for 6 h with shaking at 200 rpm, the culture medium was centrifuged at 1,290*g* and 4 °C for 15 min to collect the α-Fe_2O_3, β-FeOOH and α-FeOOH NMs from the recombinant cells. The supernatant was discarded and the pellet was resuspended in distilled water. To obtain α-Fe_2O_3 NM, the two byproducts of β-FeOOH and α-FeOOH were removed by calcination at 800 °C for 2 h in the presence of air with a heating rate of 2° min^{-1}. To obtain crystalline α-Fe_2O_3 NM *in vitro*, the recombinant *E. coli* DH5α harboring pYJ-MT-PCS induced for MT and PCS co-expression was further cultivated at 37 °C in a rotary shaker for 12 h with shaking at 200 rpm. Cell extract was prepared from the resulting cells. The $FeCl_2 \cdot 6H_2O$ was added to the final ion concentration of 1 mM into the cell extract diluted with distilled water (protein concentration of 1 mM) in a 50-ml test tubes. The pH of *in vitro* reaction solution was set at pH 6.5 using 1M NaOH solution. The precursor and the cell extract were incubated at 25 °C in a rotary shaker at 200 rpm for 6 h. To obtain α-Fe_2O_3 NM, calcination was performed as before.

Characterization of the biosynthesized NMs. The structure and morphology of the biosynthesized NMs were observed by field emission transmission electron microscopy (TEM); Tecnai F20 and Tecnai F30 (FEI Company, Frankfurt, Germany) were operated at accelerating voltages of 200 and 300 kV, respectively. The biosynthesized NMs for TEM samples were prepared by dispersing them in distilled water on a carbon-Cu grid, except for the biosynthesized Cu NM which was placed on a Ni grid. The average sizes of the biosynthesized NMs were determined by TEM analysis. Each grain up to a certain maximum diameter was manually measured to minimize counting errors one-by-one and sequentially recorded for about 100 NMs. Measurements of interplanar distance of biosynthesized crystalline NMs lattice were performed using DiffTools suite in DigitalMicrograph software (3). To identify element composition of the biosynthesized NMs, energy dispersive spectrometer (EDS) analysis was performed simultaneously. For X-ray diffraction (XRD) analysis, the NMs synthesized *in vivo* were resuspended in distilled water and disrupted by sonication. Then, they were centrifuged at 16,100 ×*g* and 4 °C for 10 min to collect the precipitates. The supernatant was discarded, and the precipitates were then resuspended in distilled water. In the case of NMs synthesized *in vitro*, the samples were resuspended in distilled water and subsequently centrifuged at 16,100 ×*g* and 4 °C for 10 min to collect the precipitates. The supernatant was discarded, and the precipitates were resuspended in distilled water. The prepared samples were drop-cast on a glass substrate and dried in 70 °C oven. We repeated these steps for several times until a thick film or powder was obtained. The XRD patterns were characterized by X-ray diffractometer (D/MAX-2,500, Rigaku, Japan) with CuKa radiation (λ=1.5406Å), 2Θ range 20-70° and a scanning rate of 2° min^{-1}. Surface characterization of biosynthesized

NMs was conducted in the form of KBr tablets by Fourier transform infrared (FTIR) spectrometry (Nicolet™ iS™50, Thermo Scientific, Waltham, MA, USA). The magnetization of biosynthesized magnetic crystalline NMs, including Mn_3O_4, Fe_3O_4, $CoFe_2O_4$, $NiFe_2O_4$, $ZnMn_2O_4$ and $ZnFe_2O_4$ were investigated by superconducting quantum interference device-vibrating sample magnetometer (SQUID-VSM; Quantum Design, San Diego, CA, USA). The magnetic properties were measured at 300 K in an applied magnetic field sweeping from −50,000 Oe to +50,000 Oe. To remove surface-bound functional groups, *in vivo* synthesized magnetic crystalline NMs were calcinated at 800 °C for 2 h in the presence of air with a heating rate of 2° min^{-1}.

Generation of Pourbaix diagrams. To predict NM producibility, Pourbaix diagram analyses of each element at an ionic concentration of 0.5 (*in vivo*) or 1 mM (*in vitro*) were performed in aqueous solution at 37 °C (*in vivo*) or 25 °C (*in vitro*) with the Eh range of −1.046 to +1.046 V and pH range of 6 to 10 using Hydra/Medusa chemical equilibrium database and plotting software (4). It has been reported that precursor ions can form complexes and thus interfere with NM biosynthesis (5, 6). The input for generating Pourbaix diagrams includes all the precursor species and their concentrations, and temperatures and pressure (1 bar) of each *in vivo* or *in vitro* biosynthesis condition in the database. The results of Pourbaix diagrams can vary depending on the conditions such as the precursor species and their concentrations, temperatures, and pressures, respectively.

Measurement of Eh and pH. The Eh and pH were measured during *in vivo* and *in vitro* biosynthesis of NM of each element for 12 h. The time series measurements (0, 1, 2, 4, 6,

9 and 12 h) of the Eh and pH values were performed using electrochemistry benchtop meters (Orion ^{TM} star A211, Thermo Scientific,S11 Waltham, MA, USA).

Measurement of NADH level. Seed cultures of the wildtype *E. coli* DH5α strain harboring pTac15K (control) and recombinant *E. coli* DH5α strain harboring pYJ-MT-PCS were prepared in 25-ml test tubes containing 10 ml LB medium and 30 μg ml^{-1} of Km (for recombinant strain) at 37 °C overnight in a rotary shaker at 200 rpm. One milliliter of overnight culture was used to inoculate a 250-ml flask containing 100 ml of LB medium; for recombinant strain, Km (30 μg ml^{-1}) was supplemented. Cells were grown to an OD_{600} of 0.6, and were induced with 0.5 mM of IPTG. Cells were further cultivated for 1 h after IPTG induction. The NADH levels in the wildtype and recombinant strains were measured at 0 and 12 h using a colorimetric kit (K337-100, BioVision, Milpitas, CA, USA) by recording the absorbance at 450 nm (SpectraMax M2, Molecular Devices, Sunnyvale, CA, USA). The NADH levels of cell extract were measured using the cell extract prepared as described above. Measurements of NADH levels were conducted in triplicates.

SI Appendix Figures

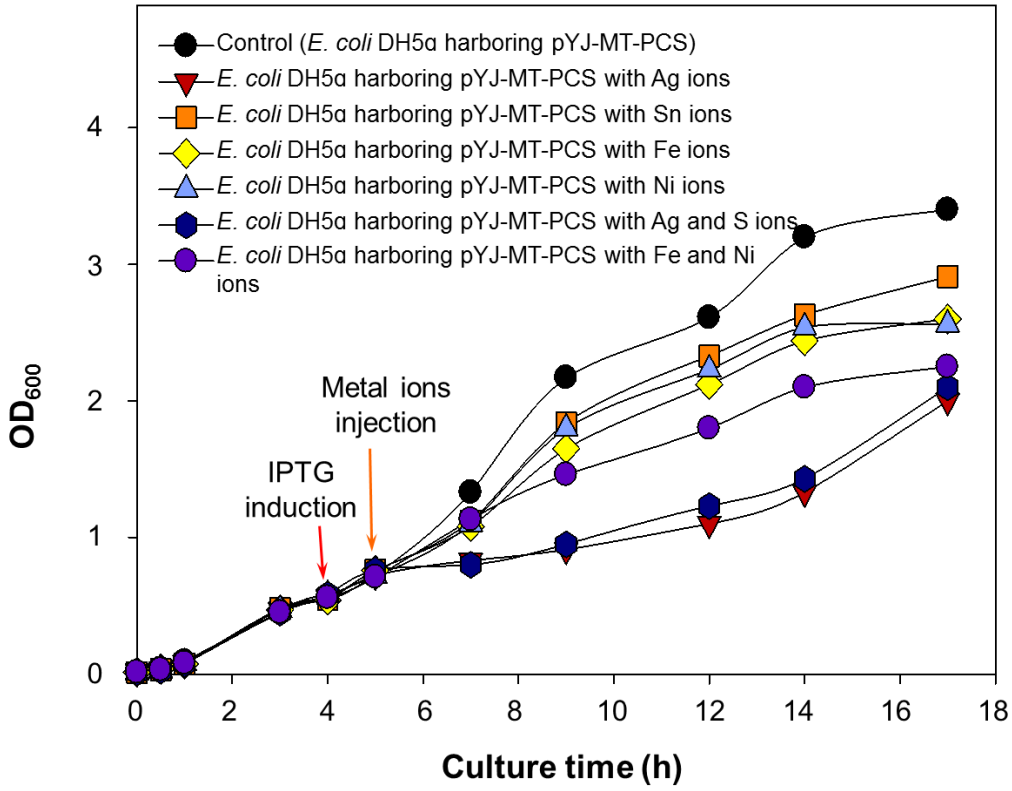

Fig. S1. Growth curves of *E. coli* DH5α harboring pYJ-MT-PCS cells in the presence of 0.5 mM of Ag, Sn, Fe, Ni, Ag/S and Fe/Ni. The control (*E. coli* DH5α harboring pYJ-MT-PCS) growth curve without precursor is shown with black circles. As can be seen, the extent of growth inhibition varies with different ions.

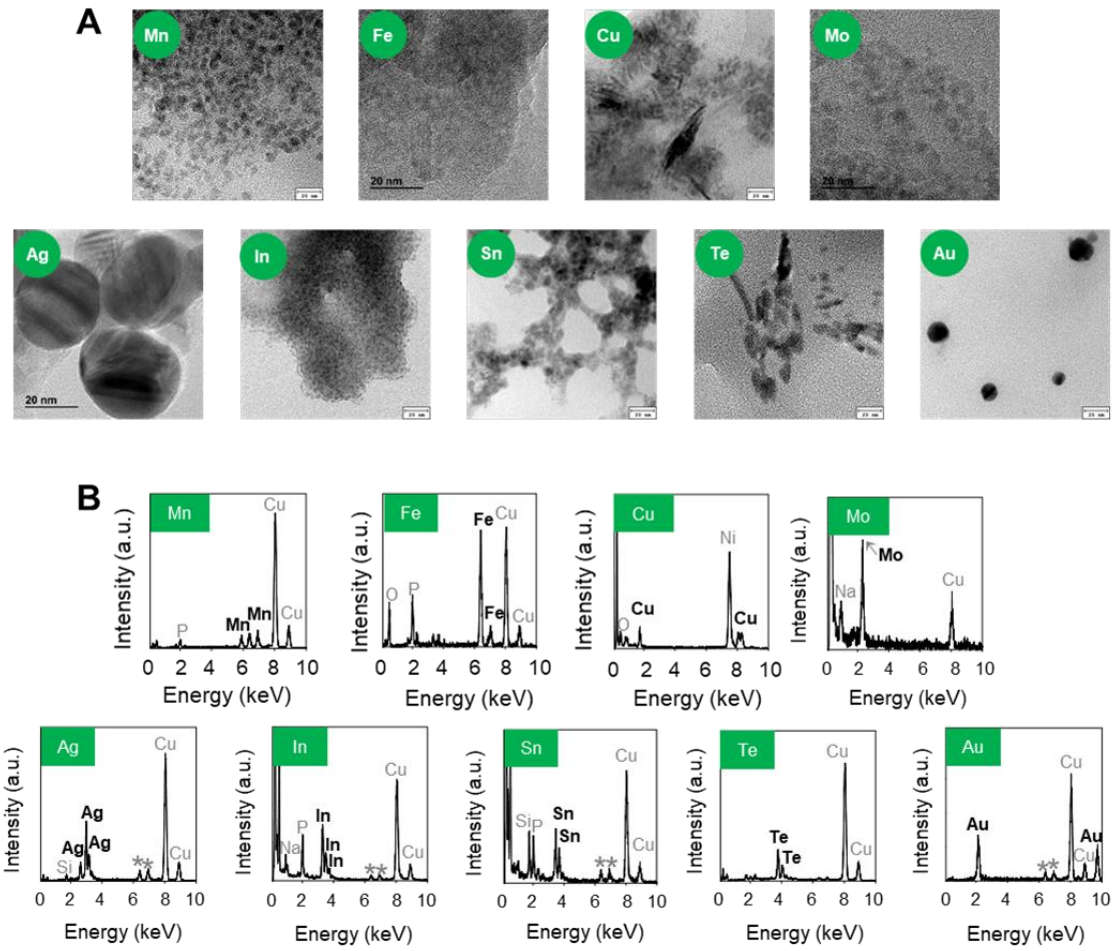

Fig. S2. TEM images and EDS graphs of the nine crystalline NMs synthesized *in vivo*. (*A*), TEM images of the crystalline NMs synthesized *in vivo* with their corresponding elements labeled in green circle. Scale bar, 20 nm. (*B*), The EDS graphs of the crystalline NMs synthesized *in vivo*. The crystalline NMs synthesized *in vivo* with their corresponding elements labeled in green square. The presence of P signal is likely due to the presence of cell debris bound to the surface of the crystalline NMs. There was Cu NM placed on a Ni grid. "**" indicates the presence of minor peaks, at around 6.4 keV and 6.9 keV from the instrument.

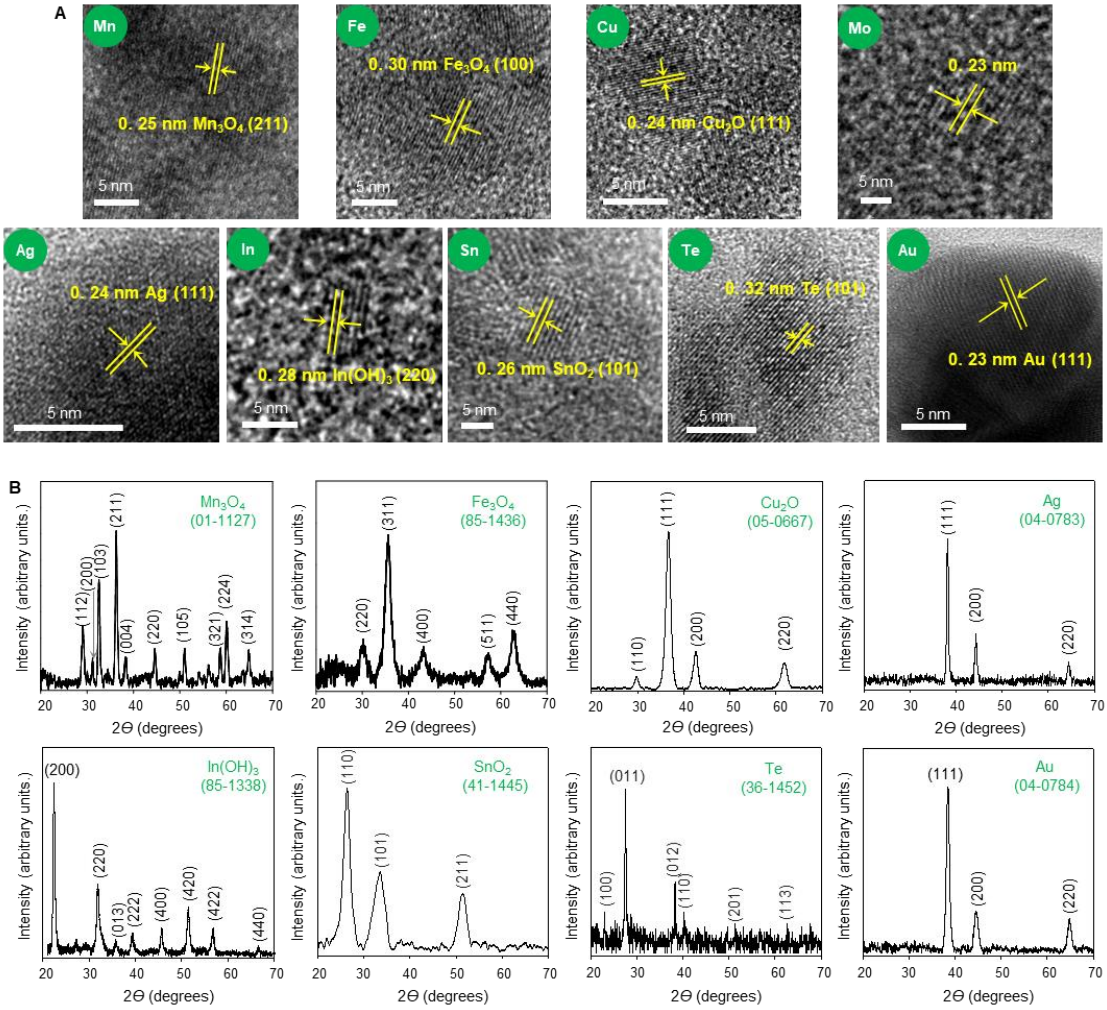

Fig. S3. HR-TEM images and the XRD patterns of the nine crystalline NMs synthesized *in vivo*. (*A*) HR-TEM images of the crystalline NMs synthesized *in vivo* with their corresponding elements labeled in green circle. The interplanar distance of the biosynthesized crystalline NM lattice and the Miller indices of crystallographic planes within parentheses are shown together. (*B*) The crystalline compositions of the biosynthesized crystalline NMs were analyzed by XRD. The green numbers in parenthesis represent the joint committee on powder diffraction standards (JCPDS) cards. The black numbers in parentheses represent Miller indices corresponding to each scattering peak. Because cell debris existed for NMs synthesized *in vivo*, background scattering from the some organic components was also recorded in the XRD patterns.

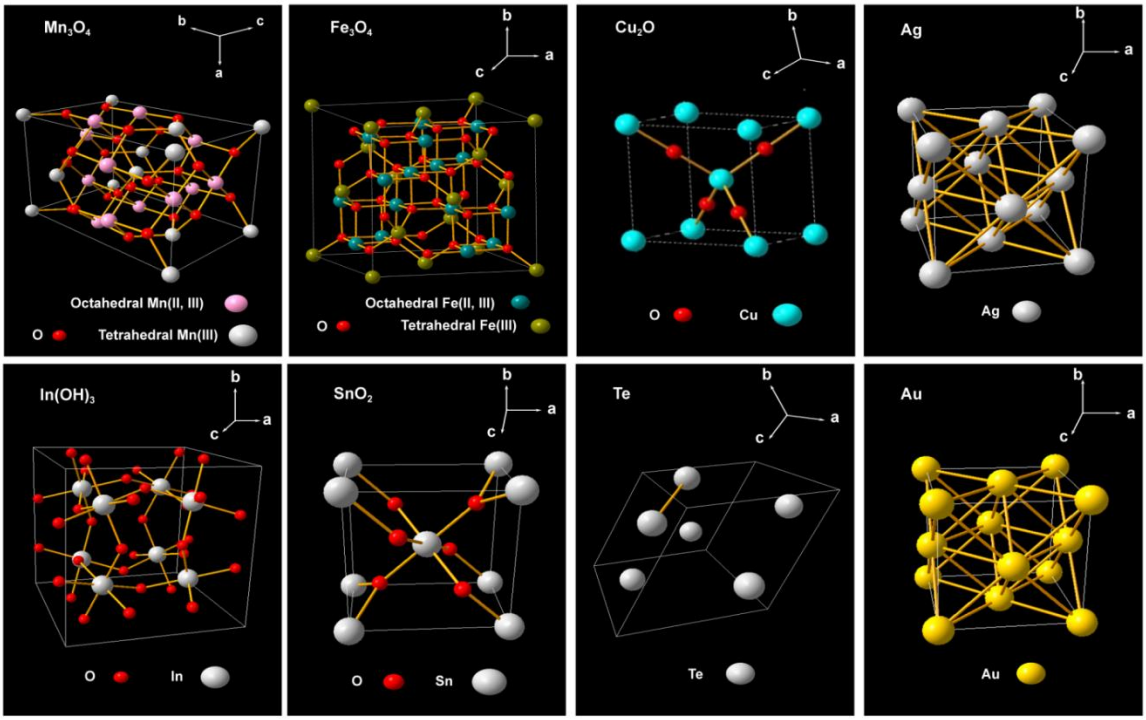

Fig. S4. Reconstructed crystal structures of the eight biosynthesized crystalline NMs. Illustrations of crystalline structures of the biosynthesized crystalline NMs based on the XRD data. Colored spheres and sticks represent individual atoms and chemical bonds between the atoms, respectively.

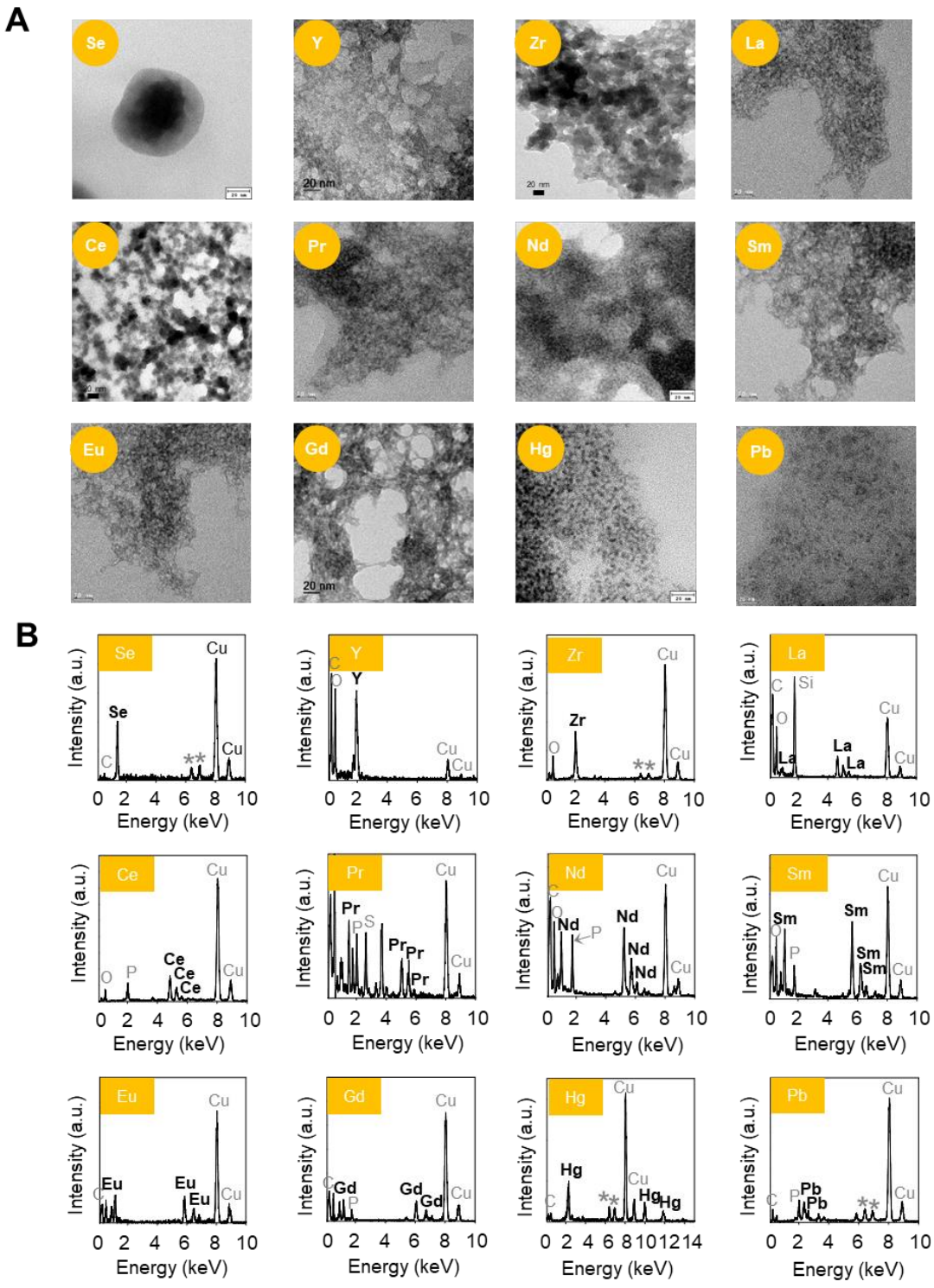

Fig. S5. TEM images and EDS graphs of the 12 amorphous NMs synthesized *in vivo*. (*A*) TEM images of the amorphous NMs synthesized *in vivo* with their corresponding elements labeled in yellow circle. Scale bar, 20 nm. (*B*) The EDS graphs of the amorphous NMs synthesized *in vivo*. The amorphous NMs synthesized *in vivo* with their corresponding elements labeled in yellow square.

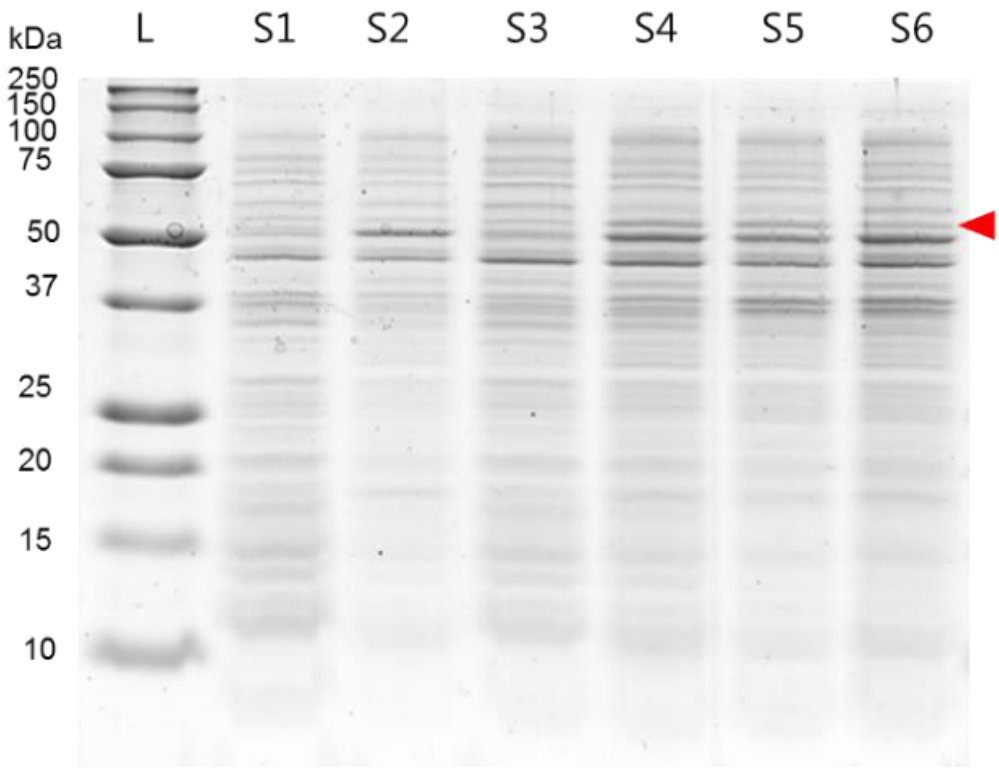

Fig. S6. SDS-PAGE analysis of MT and PCS expression in *E. coli* DH5α strain. Expression of MT (~7.9 kDa) and PCS (~54.5 kDa) in *E. coli* DH5α harboring pYJ-MT-PCS strain during cultivation. Red arrow indicates the PCS band (~54.5 kDa). The lanes are: L, molecular weight marker (kDa); S1, soluble protein fraction of *E. coli* DH5α cultivated for 12 h; S2, soluble protein fraction of recombinant *E. coli* DH5α harboring pYJ-MT-PCS cultivated for 2 h (before induction); S3-S6, soluble protein fractions of the recombinant *E. coli* at 2, 4, 8 and 12 h post induction in the presence of Sn precursor, respectively.

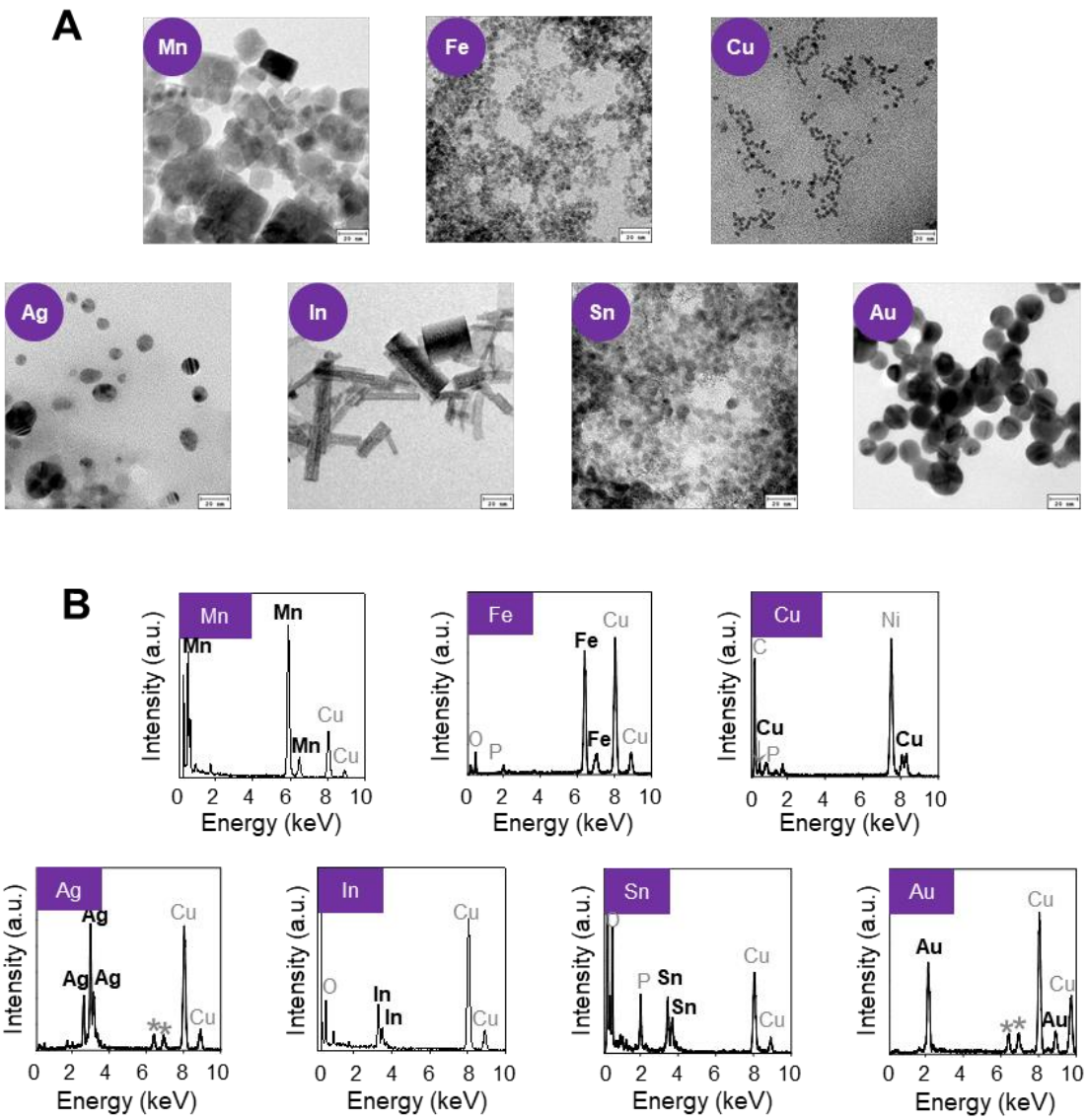

Fig. S7. TEM images and EDS graphs of the seven crystalline NMs synthesized *in vitro*. (*A*) TEM images of the crystalline NMs synthesized *in vitro* with their corresponding elements labeled in purple circle. Scale bar, 20 nm. (*B*) The EDS graphs of the crystalline NMs synthesized *in vitro*. The amorphous NMs synthesized *in vitro* with their corresponding elements labeled in purple square.

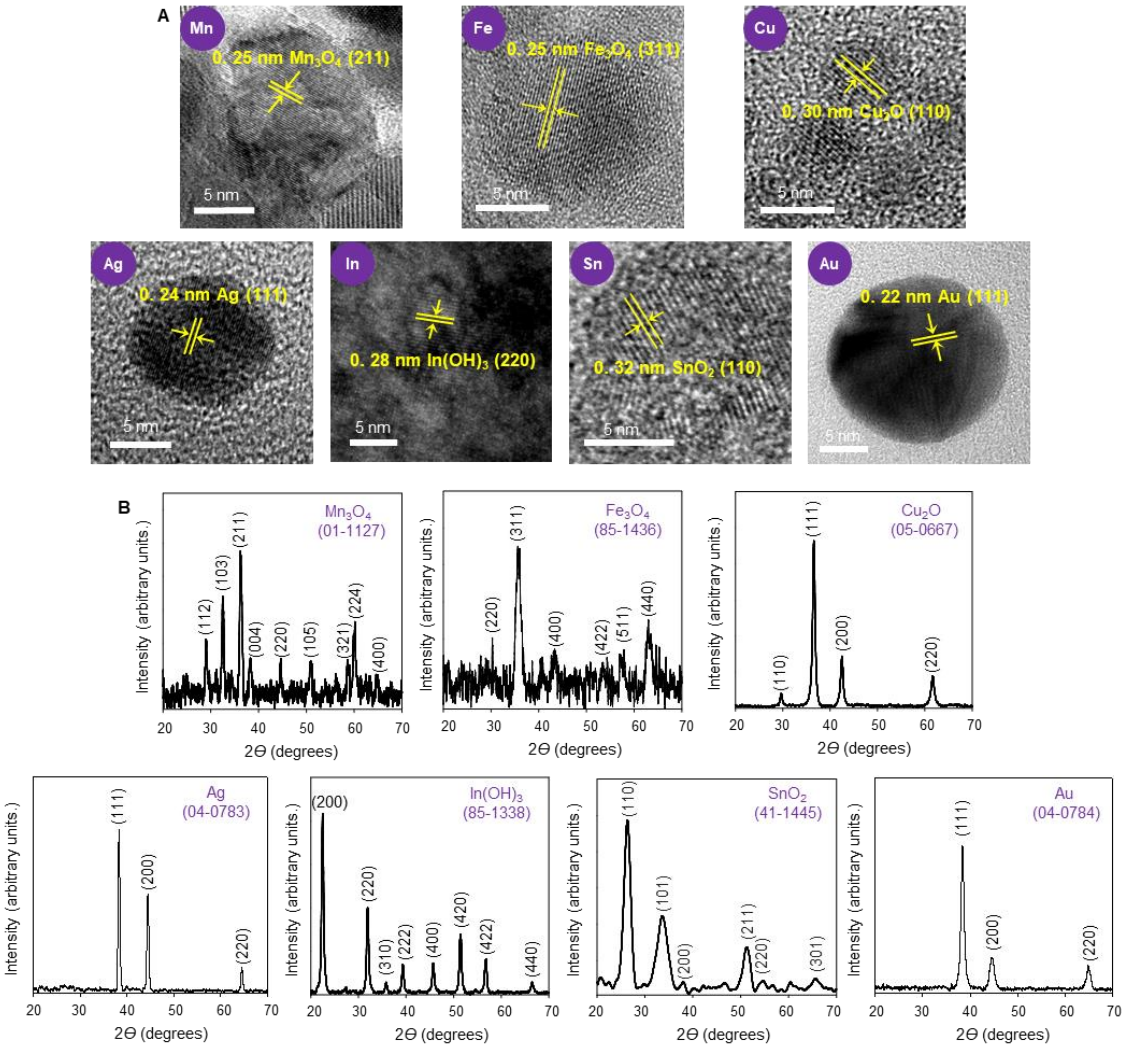

Fig. S8. HR-TEM images and the XRD patterns of the seven crystalline NMs synthesized *in vitro*. (*A*) HR-TEM images of the crystalline NMs synthesized *in vitro* with their corresponding elements labeled in purple circle. The interplanar distance of the crystalline NM lattice and the Miller indices of crystallographic planes within parentheses are shown together. (*B*) The crystalline composition confirmation of the crystalline NMs synthesized *in vitro* were analyzed using XRD. The purple numbers in parentheses represent the JCPDS cards. The black numbers in parentheses represent Miller indices corresponding to each scattering peak.

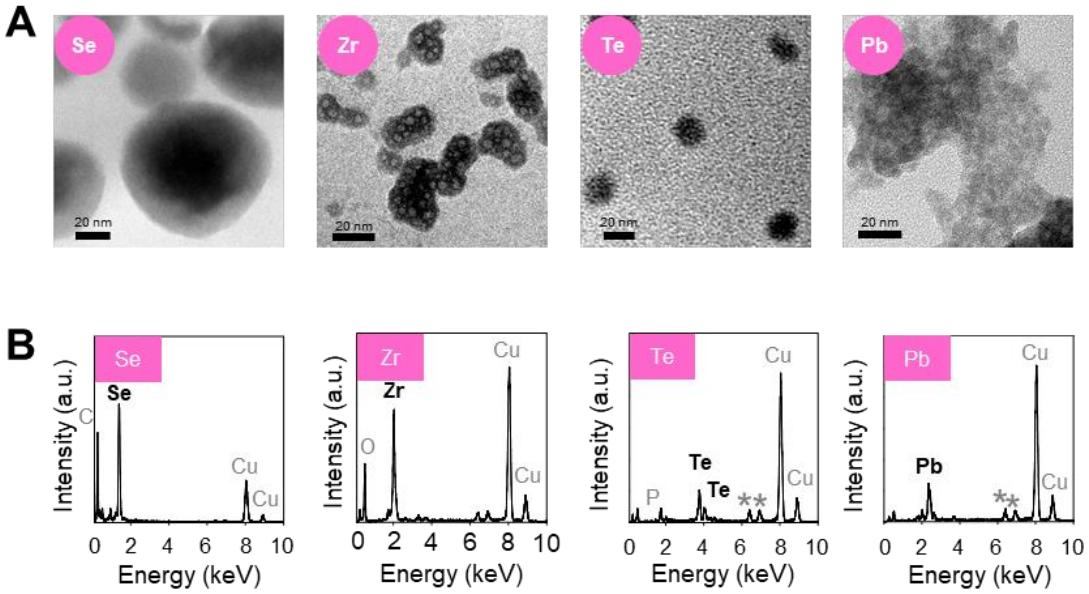

Fig. S9. TEM images and EDS graphs of the four amorphous NMs synthesized *in vitro*. (*A*) TEM images of the amorphous NMs synthesized *in vitro* with their corresponding elements labeled in pink circle. Scale bar, 20 nm. (*B*) The EDS graphs of the amorphous NMs synthesized *in vitro*. The amorphous NMs synthesized *in vitro* with their corresponding elements labeled in pink square.

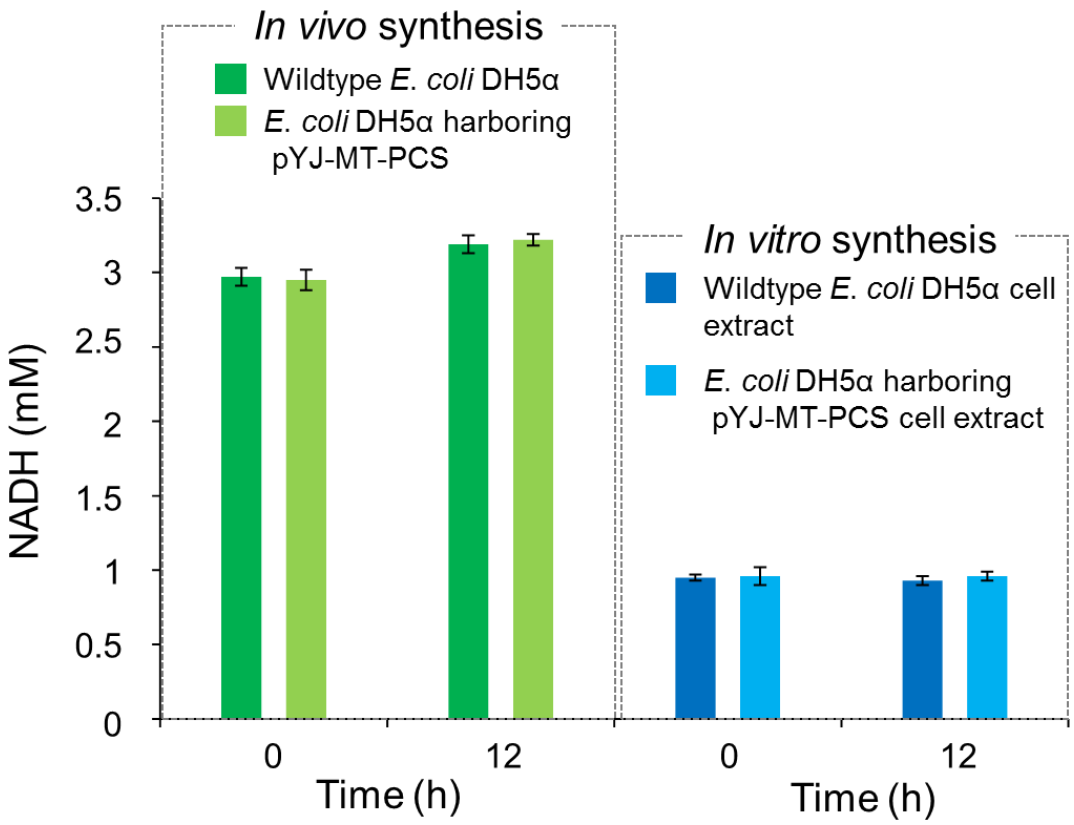

Fig. S10. NADH levels in wildtype *E. coli* DH5α strain harboring pTac15K, recombinant *E. coli* DH5α harboring pYJ-MT-PCS and that of their cell extract. NADH levels *in vivo* were measured in wildtype *E. coli* DH5α harboring a control vector pTac15K and the recombinant *E. coli* DH5α harboring pYJ-MT-PCS under 37°C at 0 h and 12 h. The NADH levels *in vitro* were measured from the cell extracts of the above strains under 25°C at 0 h and 12 h. Experiments were conducted in triplicates. Error bar indicates standard deviation (s.d).

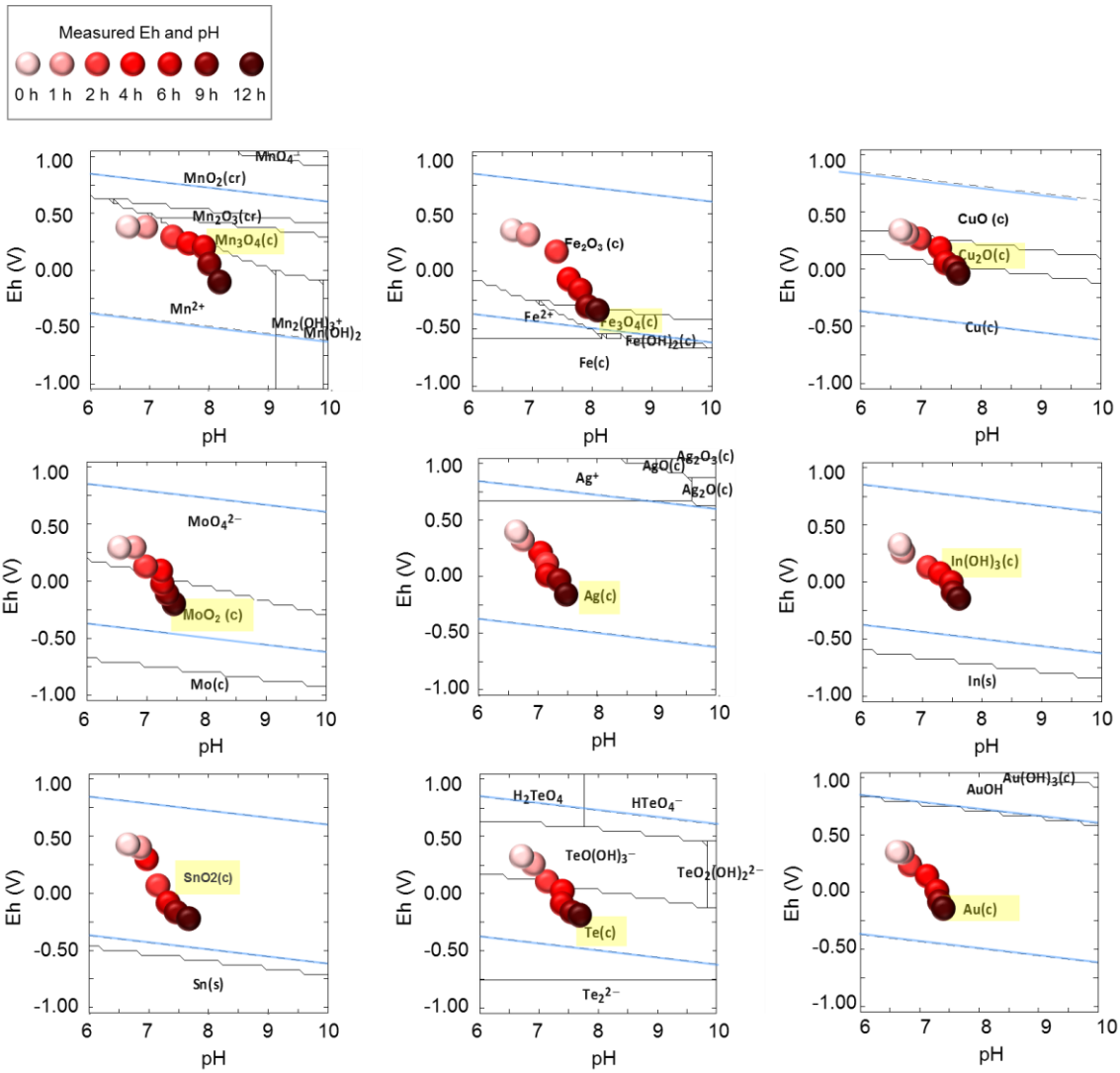

Fig. S11. Pourbaix diagram analyses and measurements of the Eh and pH during *in vivo* biosynthesis of nine crystalline NMs. In Pourbaix diagram analyses, the upper blue dashed line denotes the Eh for the oxygen evolution reaction, while the lower blue dashed line corresponds to the Eh for the hydrogen evolution reaction. Between the two blue dashed lines represent the stability region of H_2O. The phase type is indicated at the end of the name, such as (c) or (cr) for crystalline and (s) for solid. The chemical species taken into account include: MnO_4^-, MnO_2 (cr), Mn_2O_3 (cr), Mn_3O_4 (c), Mn^{2+}, $Mn_2(OH)_3^+$ and $Mn(OH)_2$ for Mn; Fe_2O_3 (c), Fe_3O_4 (c), Fe^{2+}, $Fe(OH)_2$ (c) and Fe (c) for Fe; CuO (c), Cu_2O (c) and Cu (c) for Cu; MoO_4^{2-}, MoO_2 (c) and Mo (c) for Mo; Ag_2O_3 (c), AgO (c), Ag^+, Ag_2O (c) and Ag (c) for Ag; $In(OH)_3$ (c) and In (s) for In; SnO_2 (c) and Sn (s) for Sn; H_2TeO_4, $HTeO_4^-$, $TeO(OH)_3^-$, $TeO_2(OH)_2^{2-}$, Te (c) and Te_2^{2-} for Te; $Au(OH)_3$ (c), AuOH and Au (c) for Au. The Eh and pH of the *in vivo* reactions were mapped (shown in the circle with the pink to red). The compositions of the *in vivo* synthesized crystalline NMs according to the XRD results [Mn_3O_4, Fe_3O_4, Cu_2O, Ag, $In(OH)_3$, SnO_2, Te and Au], which are indicated by the yellow box.

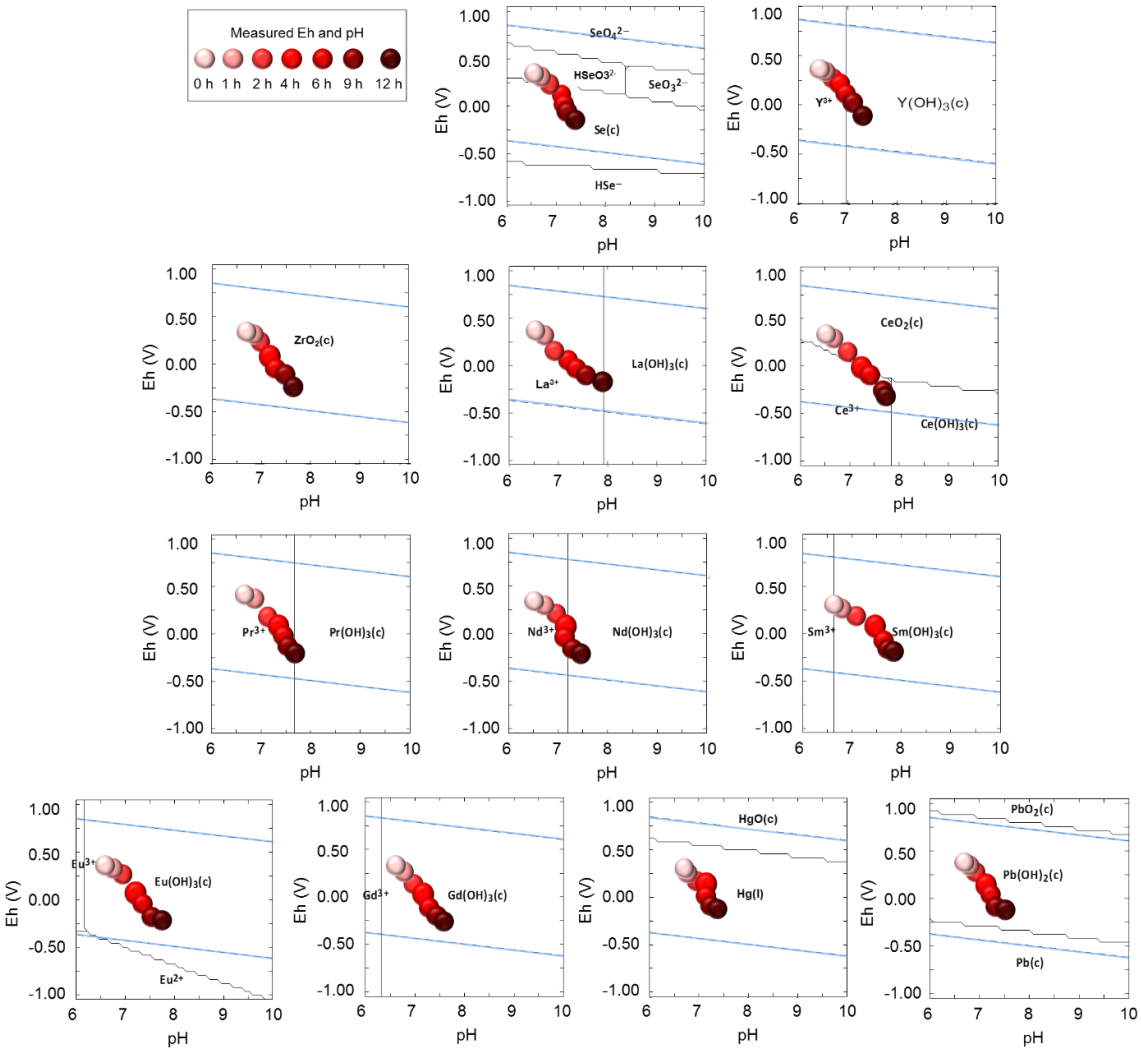

Fig. S12. Pourbaix diagram analyses and measurements of the Eh and pH during *in vivo* biosynthesis of 12 amorphous NMs. The chemical species taken into account include: SeO_4^{2-}, $HSeO_3^{2-}$, $SeO_3^{2-,}$ Se (c) and HSe^- for Se; Y^{3+} and $Y(OH)_3$ (c) for Y; ZrO_2 (c) for Zr; La^{3+} and $La(OH)_3$ (c) for La; CeO_2 (c), Ce^{3+} and $Ce(OH)_3$ (c) for Ce; Pr^{3+} and $Pr(OH)_3$ (c) for Pr; Nd^{3+} and $Nd(OH)_3$ (c) for Nd; Sm^{3+} and $Sm(OH)_3$ (c) for Sm; Eu^{3+}, $Eu(OH)_3$ (c) and Eu^{2+} for Eu; Gd^{3+} and $Gd(OH)_3$ (c) for Gd; HgO (c) and Hg (l) for Hg; PbO_2 (c), $Pb(OH)_2$ (c) and Pb (c) for Pb. The Eh and pH of the *in vivo* reactions were mapped (shown in the circle with the pink to red).

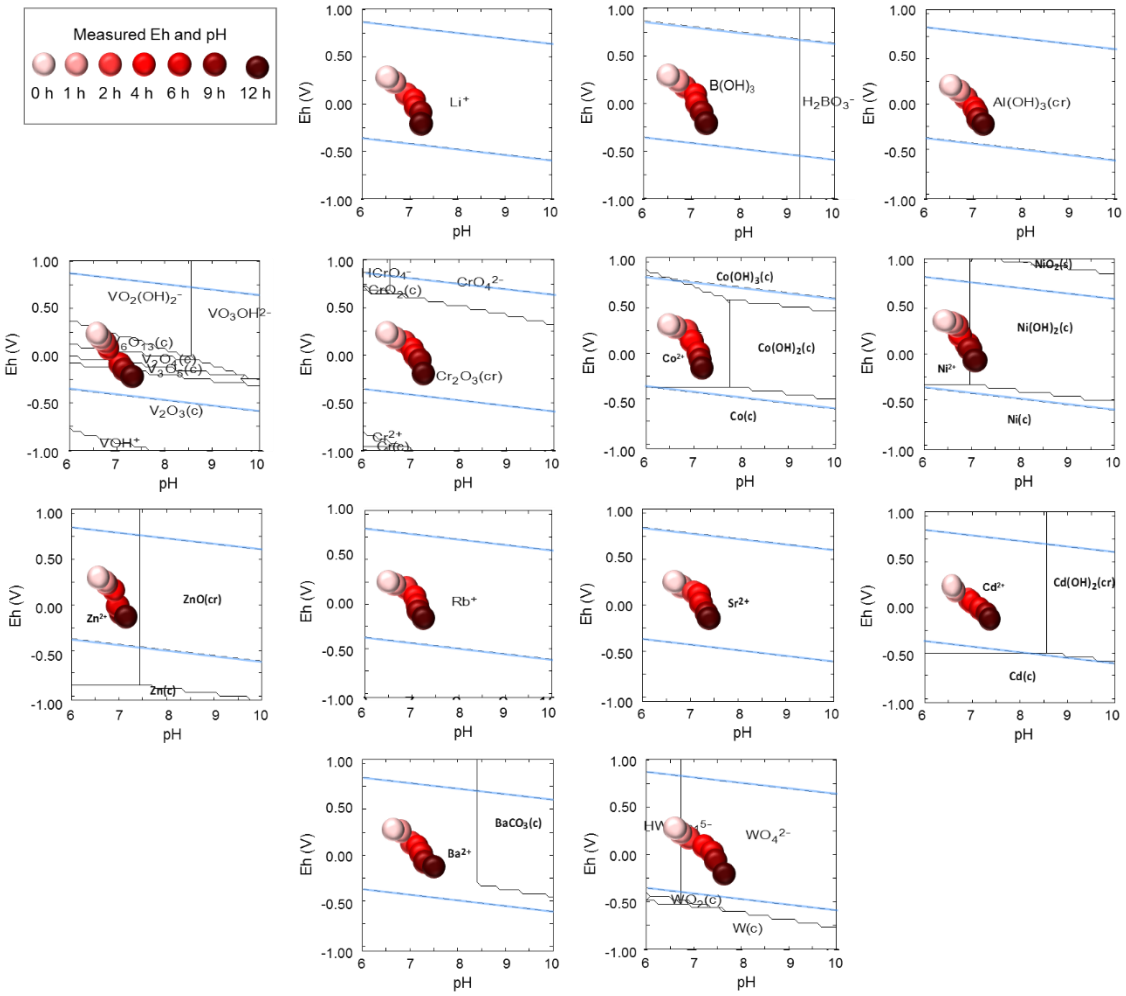

Fig. S13. Pourbaix diagram analyses and measurements of the Eh and pH in the *in vivo* conditions of no NM formation. The chemical species taken into account include: Li^+ for Li; $B(OH)_3$ and H_2BO_3 for B; $Al(OH)_3$ (cr) for Al; $VO_2(OH)_2^-$, VO_3OH^{2-}, V_6O_{13} (c), V_2O_4 (c), V_3O_5 (c), V_2O_3 (c) and VOH^+ for V; $HCrO_4^-$, CrO_2 (c), CrO_4^{2-}, Cr_2O_3 (cr) and Cr^{2+} for Cr; $Co(OH)_3$ (c), Co^{2+}, $Co(OH)_2$ (c) and Co (c) for Co; NiO_2 (s), Ni^{2+}, $Ni(OH)_2$ (c) and Ni (c) for Ni; Zn^{2+}, ZnO (cr) and Zn (c) for Zn; Rb^+ for Rb; Sr^{2+} for Sr; Y^{3+} and $Y(OH)_3$ (c) for Y; Cd^{2+}, $Cd(OH)_2$ (cr) and Cd (c) for Cd; Ba^{2+} and $BaCO_3$ (c) for Ba; $HW_6O_{21}^{5-}$, WO_4^{2-}, WO_2 (c) and W (c) for W. The Eh and pH of the *in vivo* reactions were mapped (shown in the circle with the pink to red).

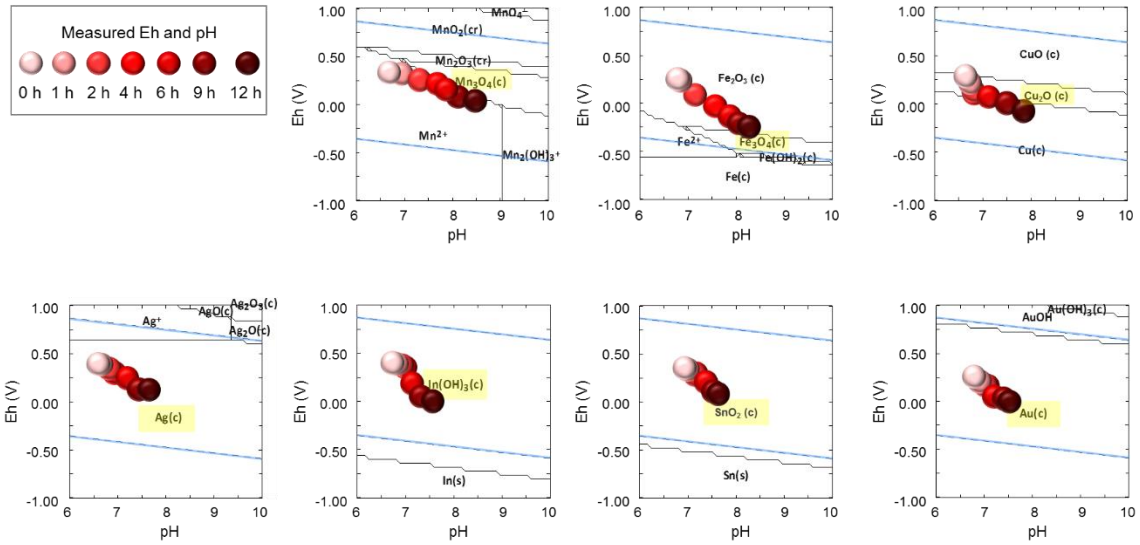

Fig. S14. Pourbaix diagram analyses and measurements of the Eh and pH during *in vitro* biosynthesis of seven crystalline NMs. The chemical species taken into account include: MnO_4^-, MnO_2 (cr), Mn_2O_3 (cr), Mn_3O_4 (c), Mn^{2+}, $Mn_2(OH)_3^+$ and $Mn(OH)_2$ for Mn; Fe_2O_3 (c), Fe_3O_4 (c), Fe^{2+}, $Fe(OH)_2$ (c) and Fe (c) for Fe; CuO (c), Cu_2O (c) and Cu (c) for Cu; MoO_4^{2-}, MoO_2 (c) and Mo (c) for Mo; Ag_2O_3 (c), AgO (c), Ag^+, Ag_2O (c) and Ag (c) for Ag; $In(OH)_3$ (c) and In (s) for In; SnO_2 (c) and Sn (s) for Sn; $Au(OH)_3$ (c), AuOH and Au (c) for Au. The Eh and pH of the *in vitro* reactions were mapped (shown in the circle with the pink to red). The compositions of the *in vitro* synthesized crystalline NMs according to the XRD results [Mn_3O_4, Fe_3O_4, Cu_2O, Ag, $In(OH)_3$, SnO_2 and Au], which are indicated by the yellow box.

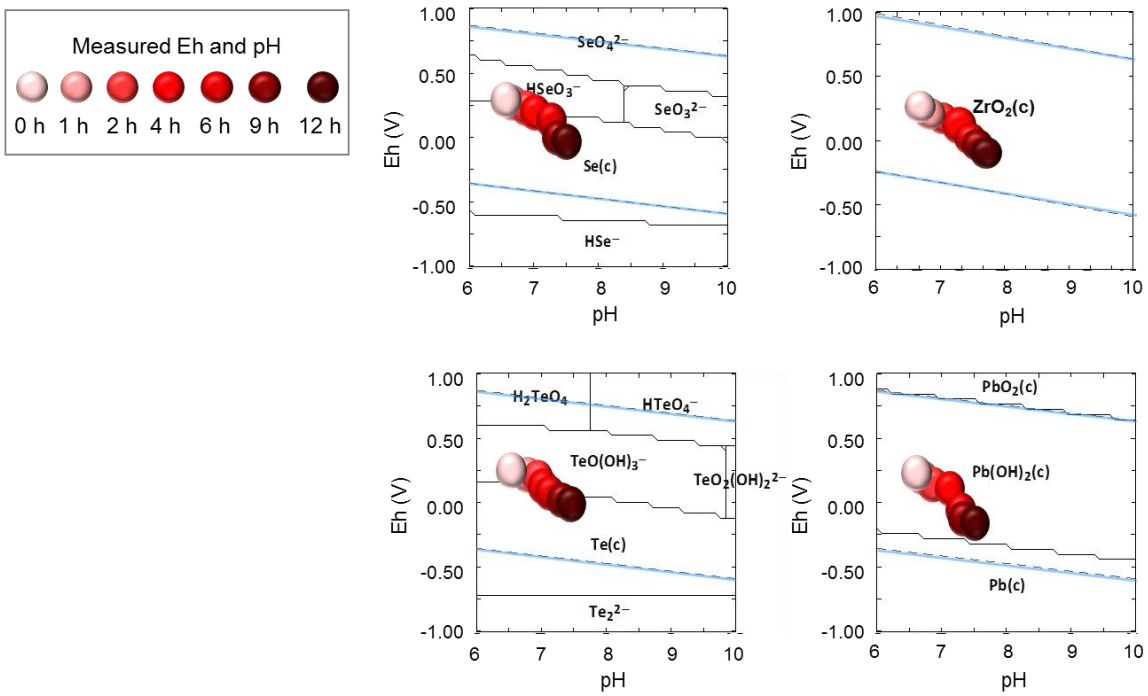

Fig. S15. Pourbaix diagram analyses and measurements of the Eh and pH during *in vitro* biosynthesis of four amorphous NMs. The chemical species taken into account include: SeO_4^{2-}, $HSeO_3^{2-}$, SeO_3^{2-}, Se (c) and HSe^- for Se; ZrO_2 (c) for Zr; H_2TeO_4, $HTeO_4^-$, $TeO(OH)_3^-$, $TeO_2(OH)_2^{2-}$, Te (c) and Te_2^{2-} for Te; PbO_2 (c), $Pb(OH)_2$ (c) and Pb (c) for Pb. The Eh and pH of the *in vitro* reactions were mapped (shown in the circle with the pink to red).

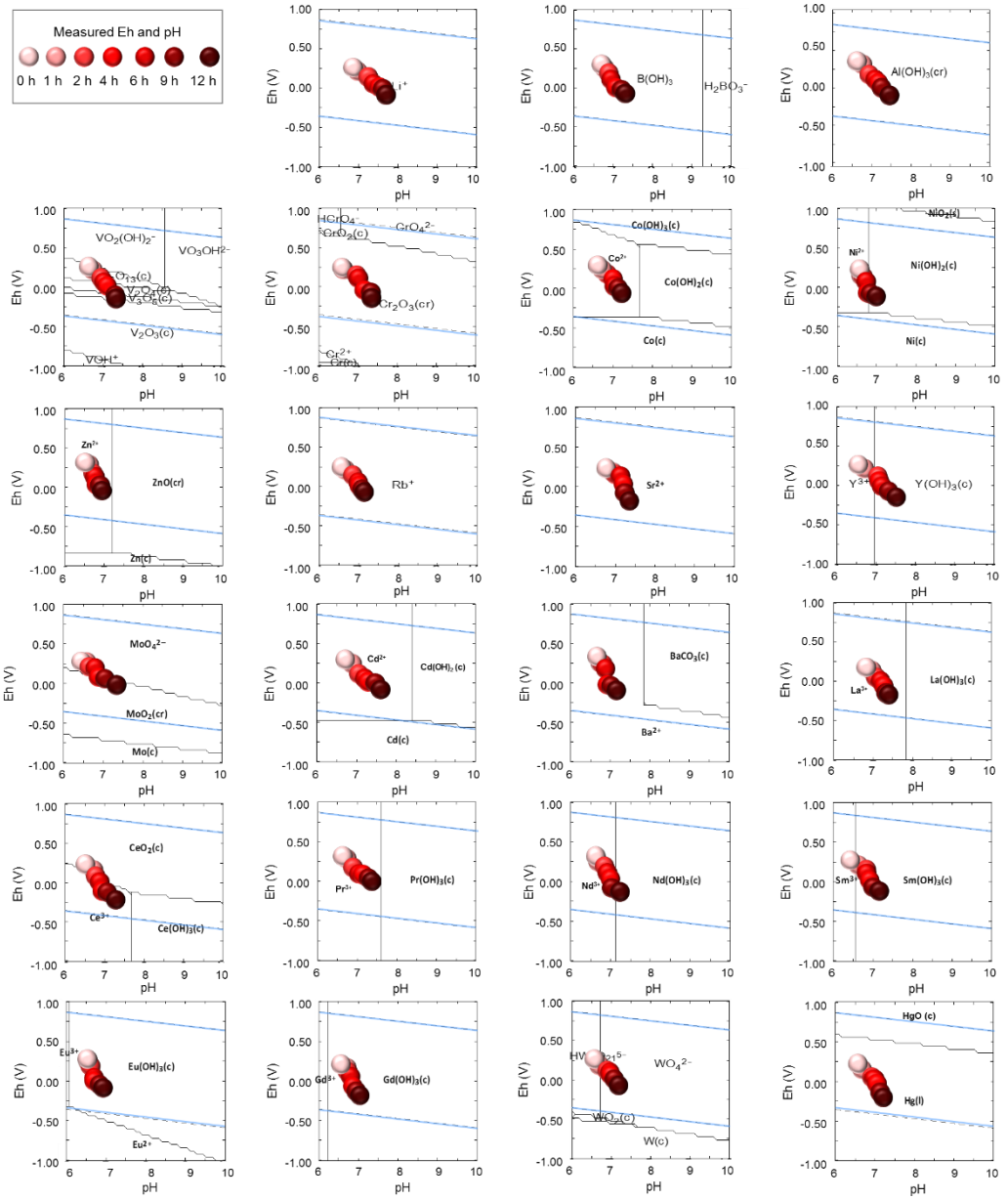

Fig. S16. Pourbaix diagram analyses and measurements of the Eh and pH in the *in vitro* conditions of no NM formation. The chemical species taken into account include: Li^+ for Li; $B(OH)_3$ and H_2BO_3 for B; $Al(OH)_3$ (cr) for Al; $VO_2(OH)_2^-$, VO_3OH^{2-}, V_6O_{13} (c), V_2O_4 (c), V_3O_5 (c), V_2O_3 (c) and VOH^+ for V; $HCrO_4^-$, CrO_2 (c), CrO_4^{2-}, Cr_2O_3 (cr) and Cr^{2+} for Cr; $Co(OH)_3$ (c), Co^{2+}, $Co(OH)_2$ (c) and Co (c) for Co; NiO_2 (s), Ni^{2+}, $Ni(OH)_2$ (c) and Ni (c) for Ni; Zn^{2+}, ZnO (cr) and Zn (c) for Zn; Rb^+ for Rb; Sr^{2+} for Sr; Y^{3+} and $Y(OH)_3$ (c) for Y; MoO_4^{2-}, MoO_2 (cr) and Mo (c) for Mo; Cd^{2+}, $Cd(OH)_2$ (c) and Cd (c) for Cd; Ba^{2+} and $BaCO_3$ (c) for Ba; La^{3+} and $La(OH)_3$ (c) for La; CeO_2 (c), Ce^{3+} and $Ce(OH)_3$ (c) for Ce; Pr^{3+} and $Pr(OH)_3$ (c) for Pr; Nd^{3+} and $Nd(OH)_3$ (c) for Nd; Sm^{3+} and $Sm(OH)_3$ (c) for Sm; Eu^{3+}, $Eu(OH)_3$ (c) and Eu^{2+} for Eu; Gd^{3+} and $Gd(OH)_3$ (c) for Gd; $HW_6O_{21}^{5-}$, WO_4^{2-}, WO_2 (c) and W (c) for W; HgO (c) and Hg (l) for Hg. The Eh and pH of the *in vitro* reactions were mapped (shown in the circle colored in pink to red).

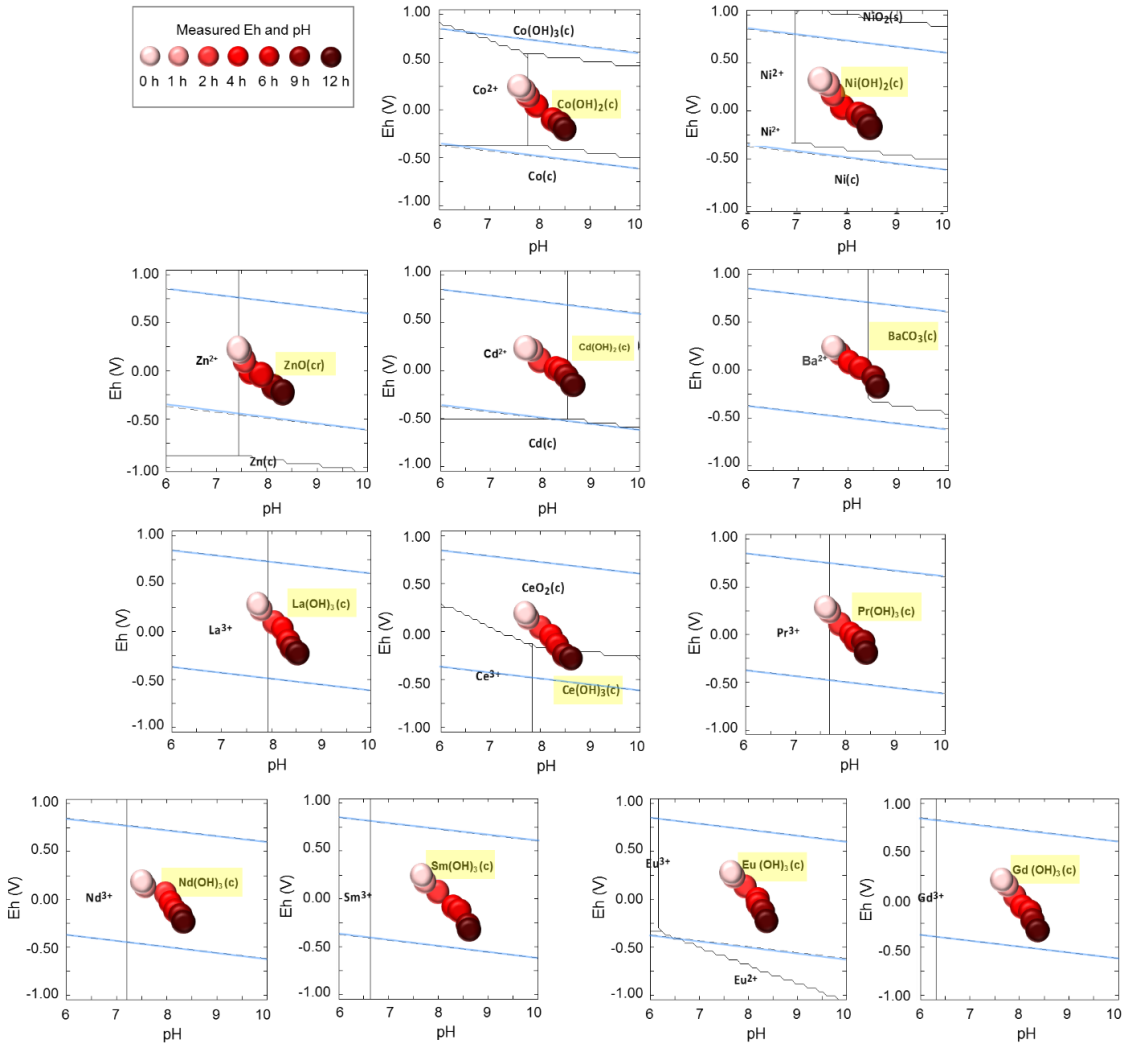

Fig. S17. Pourbaix diagram analyses and measurements of the Eh and pH during *in vivo* biosynthesis of 12 crystalline NMs at pH 7.5. The chemical species taken into account include: $Co(OH)_3$ (c), Co^{2+}, $Co(OH)_2$ (c) and Co (c) for Co; NiO_2 (s), Ni^{2+}, $Ni(OH)_2$ (c) and Ni (c) for Ni; Zn^{2+}, ZnO (cr) and Zn (c) for Zn; Cd^{2+}, $Cd(OH)_2$ (c) and Cd (c) for Cd; Ba^{2+} and $BaCO_3$ (c) for Ba; La^{3+} and $La(OH)_3$ (c) for La; CeO_2 (c), Ce^{3+} and $Ce(OH)_3$ (c) for Ce; Pr^{3+} and $Pr(OH)_3$ (c) for Pr; Nd^{3+} and $Nd(OH)_3$ (c) for Nd; Sm^{3+} and $Sm(OH)_3$ (c) for Sm; Eu^{3+}, $Eu(OH)_3$ (c) and Eu^{2+} for Eu; Gd^{3+} and $Gd(OH)_3$ (c) for Gd. The Eh and pH of the *in vivo* reactions were mapped (shown in the circle with the pink to red). The compositions of *in vivo* synthesized crystalline NMs at pH 7.5 according to the XRD results [β-$Co(OH)_2$ and Co_3O_4, β-$Ni(OH)_2$, ZnO, β-$Cd(OH)_2$, $Cd(OH)_2$, $BaCO_3$, $La(OH)_3$, CeO_2 and $Ce(OH)_3$, $Pr(OH)_3$, $Nd(OH)_3$, $Sm(OH)_3$, $Eu(OH)_3$ and $Gd(OH)_3$], which are indicated by the yellow box.

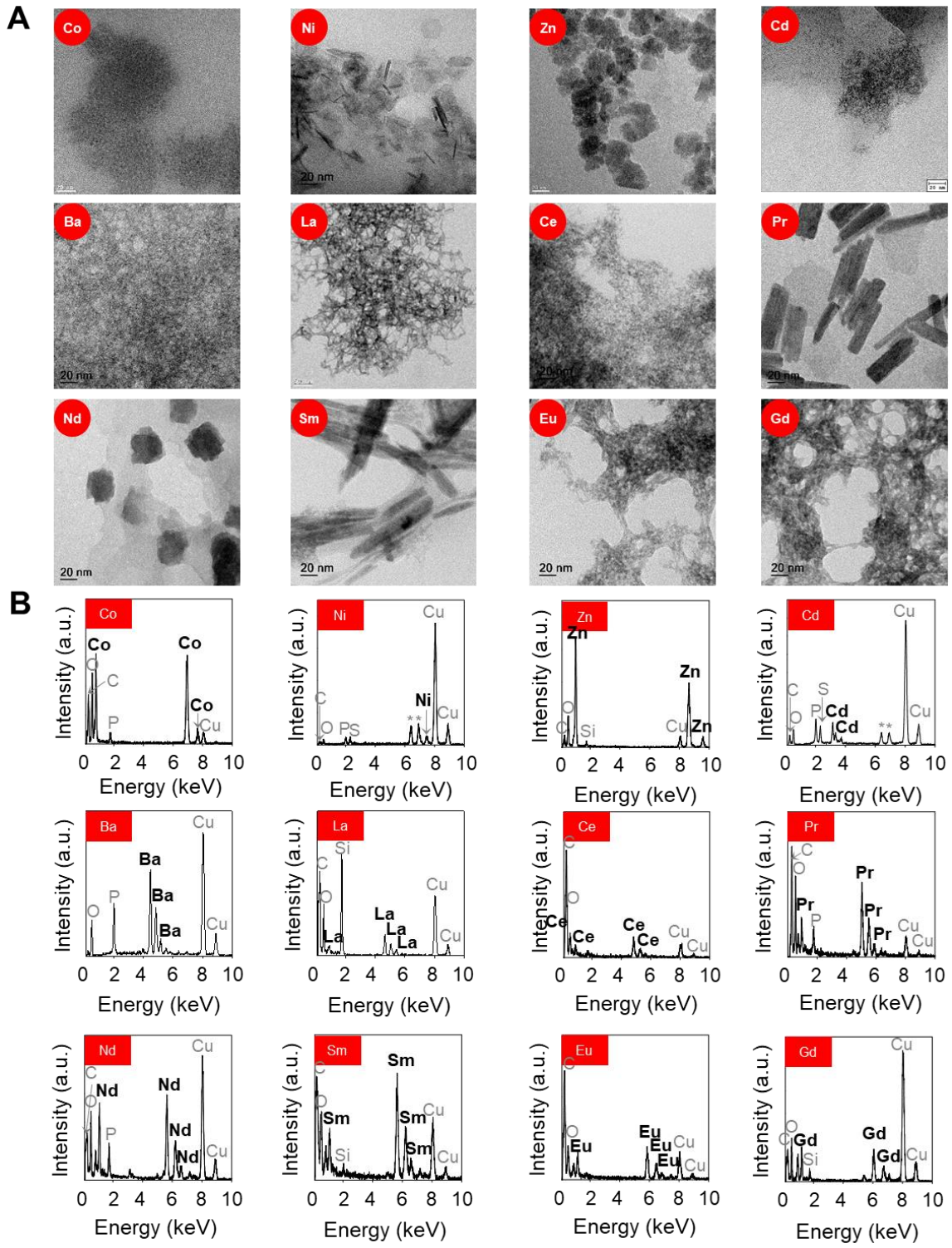

Fig. S18. TEM images and EDS graphs of the 12 crystalline NMs synthesized *in vivo* at the pH 7.5. (*A*) TEM images of the crystalline NMs synthesized *in vivo* with their corresponding elements labeled in red circle. Scale bar, 20 nm. (*B*) The EDS graphs of the crystalline NMs synthesized *in vivo*. The crystalline NMs synthesized *in vivo* with their corresponding elements labeled in red square.

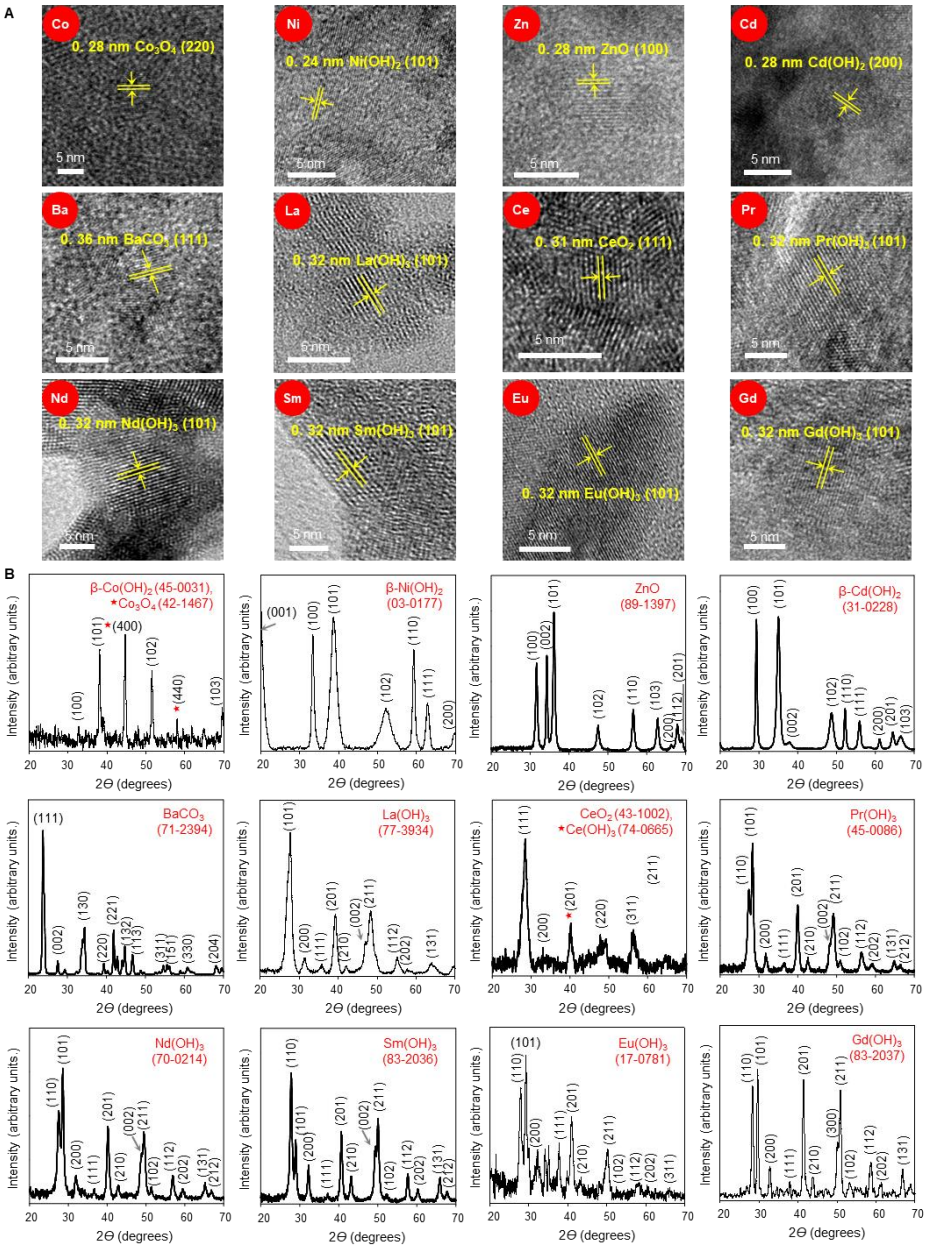

Fig. S19. HR-TEM images and the XRD patterns of 12 crystalline NMs synthesized *in vivo* at pH 7.5. (*A*) HR-TEM images of the crystalline NMs synthesized *in vivo* at pH 7.5 with their corresponding elements labeled in red circle. The interplanar distance of the crystalline NM lattice and the Miller indices of crystallographic planes within parentheses are shown together. (*B*) The crystalline compositions of the biosynthesized crystalline NMs were analyzed using XRD. The red numbers in parentheses represent JCPDS cards. The black numbers in parentheses represent Miller indices corresponding to each scattering peak. Because cell debris existed for NMs synthesized *in vivo*, background scattering from the some organic components was also recorded in the XRD patterns.

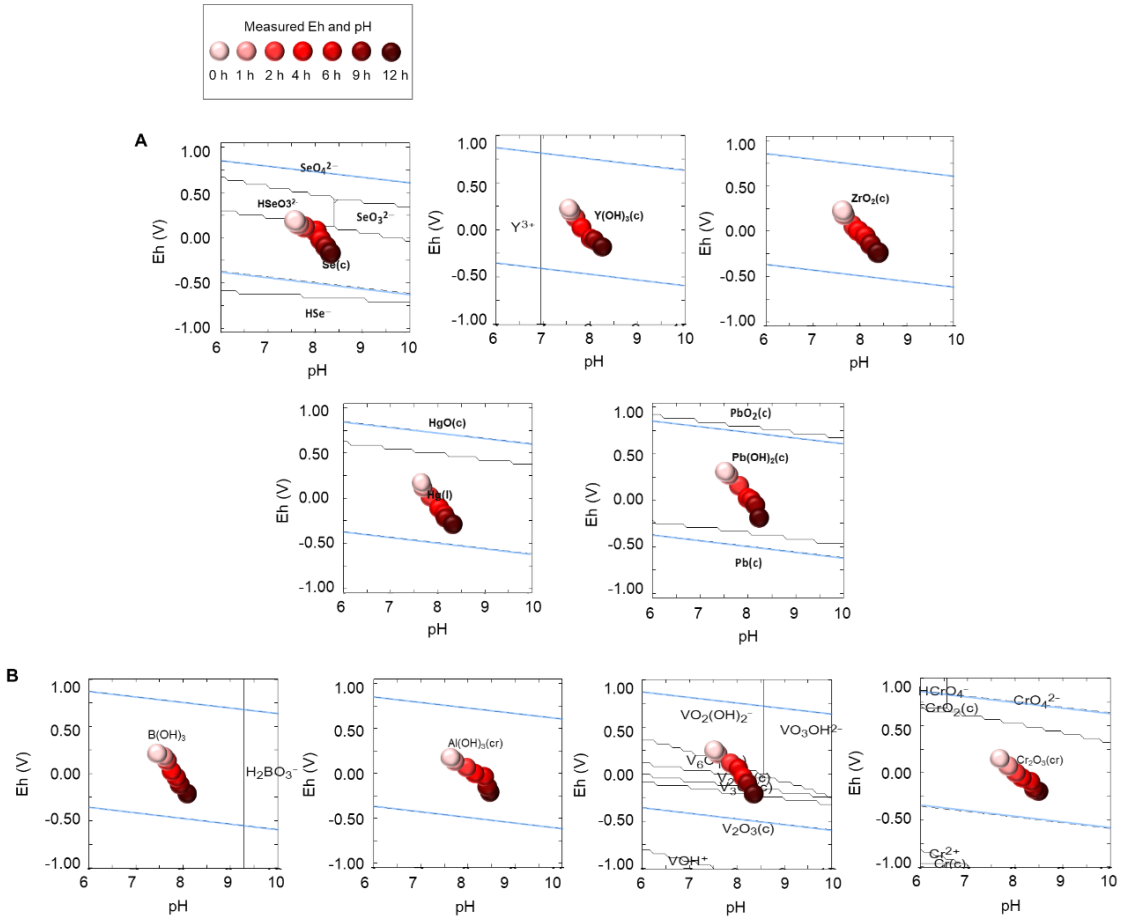

Fig. S20. Pourbaix diagram analyses and measurements of the Eh and pH in the *in vivo* conditions of amorphous NMs or no NM formation at pH 7.5. (*A*) Formation of amorphous NMs at pH at 7.5. The species taken into account include: SeO_4^{2-}, $HSeO_3^{2-}$, SeO_3^{2-}, Se (c) and HSe^- for Se; Y^{3+} and $Y(OH)_3$ (c) for Y; ZrO_2(c) for Zr; HgO (c) and Hg (l) for Hg; PbO_2 (c), $Pb(OH)_2$ (c) and Pb (c) for Pb. (*B*) No NM synthesis at pH 7.5. The species taken into account include: $B(OH)_3$ and H_2BO_3 for B; $Al(OH)_3$ (cr) for Al; $VO_2(OH)_2^-$, VO_3OH^{2-}, V_6O_{13} (c), V_2O_4 (c), V_3O_5 (c), V_2O_3 (c) and VOH^+ for V; $HCrO_4^-$, CrO_2 (c), CrO_4^{2-}, Cr_2O_3 (cr) and Cr^{2+} for Cr. The Eh and pH of the *in vivo* reactions were mapped (shown in the circle with the pink to red).

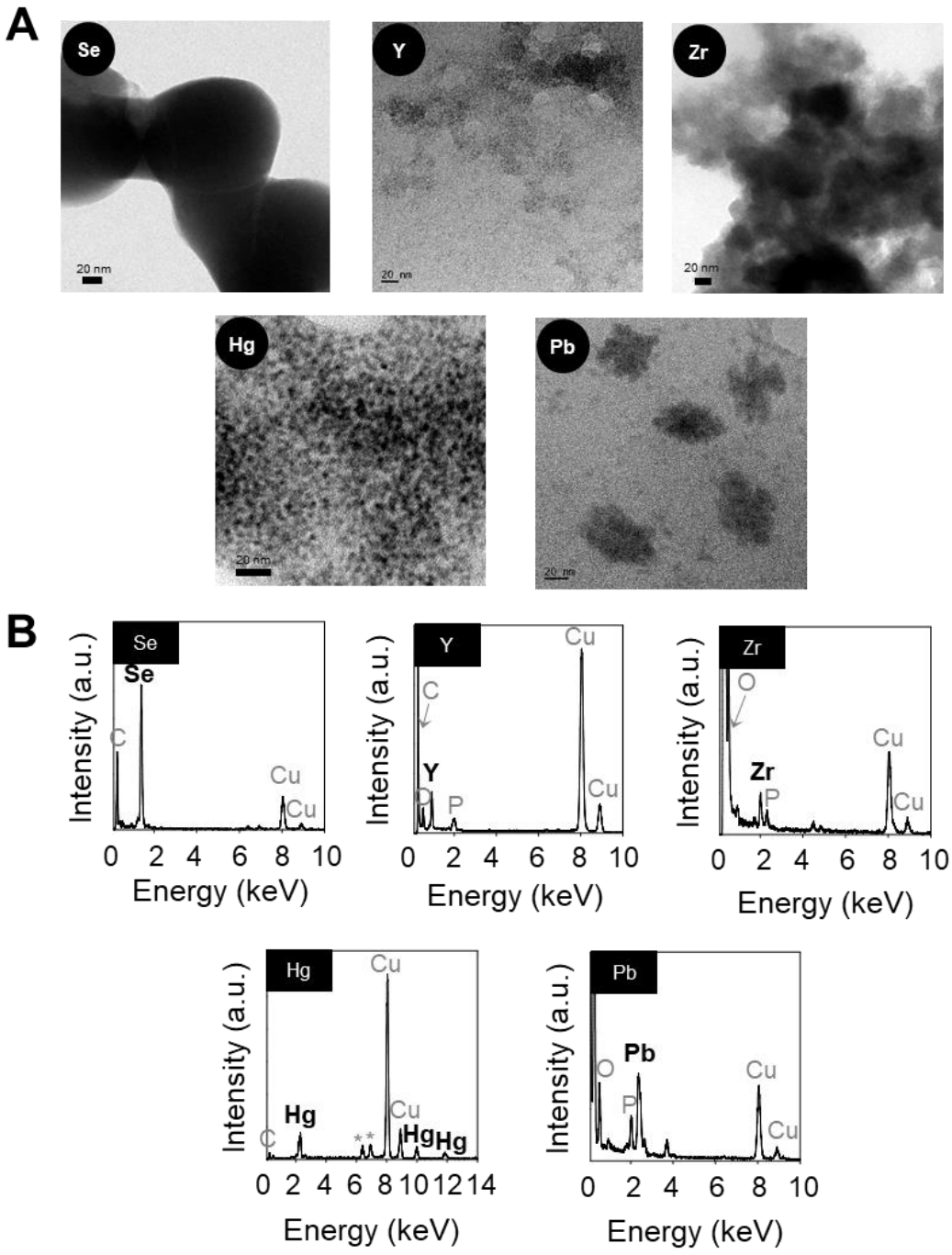

Fig. S21. TEM images and EDS graphs of the amorphous NMs synthesized *in vivo* at pH 7.5. (*A*) TEM images of the amorphous NMs synthesized *in vivo* with their corresponding elements labeled in black circle. Scale bar, 20 nm. (*B*) The EDS graphs of the amorphous NMs synthesized *in vivo*. The amorphous NMs synthesized *in vivo* with their corresponding elements labeled in black square.

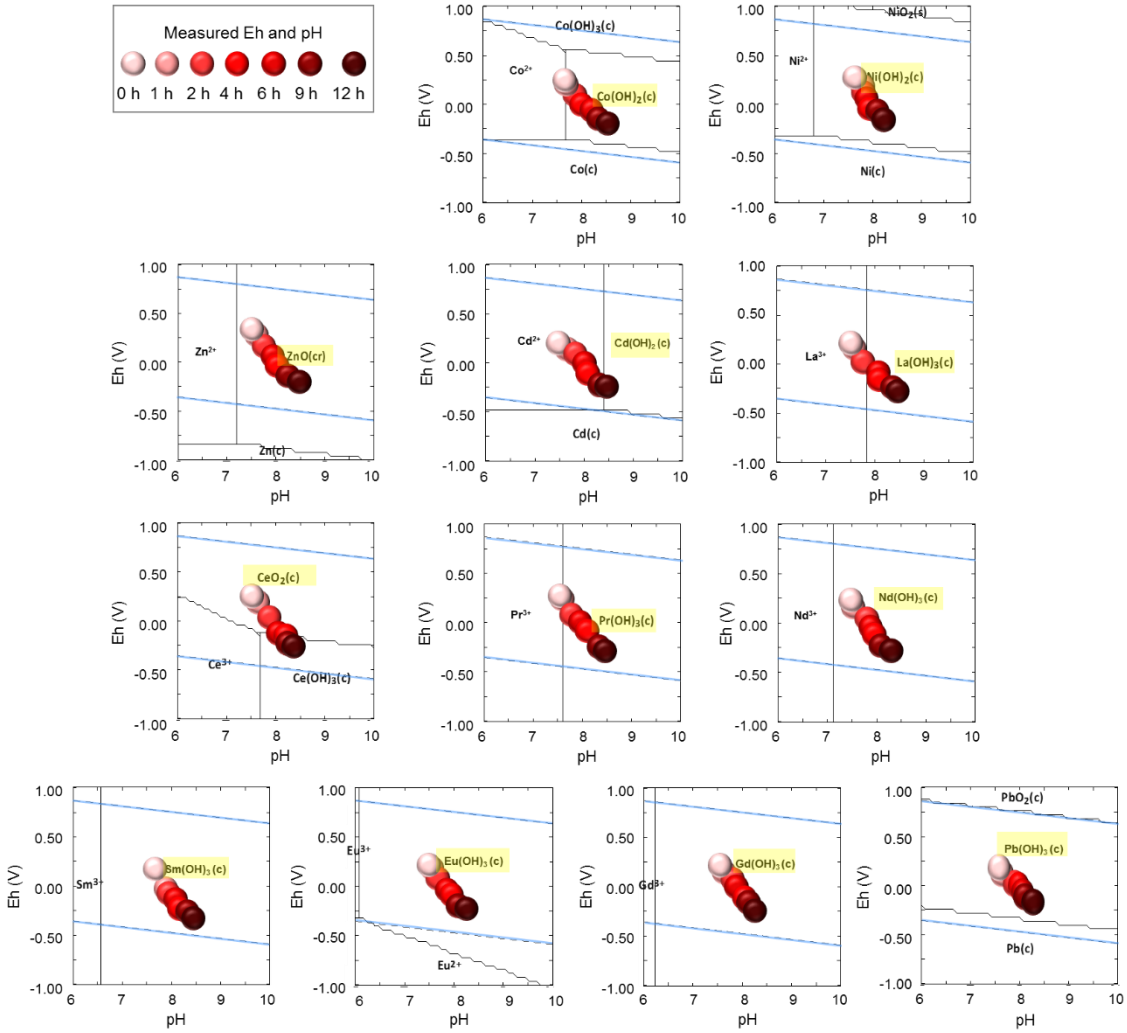

Fig. S22. Pourbaix diagram analyses and measurements of the Eh and pH during *in vitro* biosynthesis of 12 crystalline NMs at pH 7.5. The chemical species taken into account include: $Co(OH)_3$ (c), Co^{2+}, $Co(OH)_2$ (c) and Co (c) for Co; NiO_2 (s), Ni^{2+}, $Ni(OH)_2$ (c) and Ni (c) for Ni; Zn^{2+}, ZnO (cr) and Zn (c) for Zn; Cd^{2+}, $Cd(OH)_2$ (c) and Cd (c) for Cd; La^{3+} and $La(OH)_3$ (c) for La; CeO_2 (c), Ce^{3+} and $Ce(OH)_3$ (c) for Ce; Pr^{3+} and $Pr(OH)_3$ (c) for Pr; Nd^{3+} and $Nd(OH)_3$ (c) for Nd; Sm^{3+} and $Sm(OH)_3$ (c) for Sm; Eu^{3+}, $Eu(OH)_3$ (c) and Eu^{2+} for Eu; Gd^{3+} and $Gd(OH)_3$ (c) for Gd; PbO_2 (c), $Pb(OH)_2$ (c) and Pb (c) for Pb. The Eh and pH of the *in vitro* reactions were mapped (shown in the circle with the pink to red). The compositions of *in vitro* synthesized crystalline NMs using the cell extract at pH 7.5 according to the XRD results [β-$Co(OH)_2$, β-$Ni(OH_2$, ZnO, β-$Cd(OH)_2$, $Cd(OH)_2$, $La(OH)_3$, CeO_2, $Pr(OH)_3$, $Nd(OH)_3$, $Sm(OH)_3$, $Eu(OH)_3$, $Gd(OH)_3$ and $Pb_3(NO)_3(OH)_5$ and $Pb_2(NO)_3(OH)_3$], which are indicated by the yellow box.

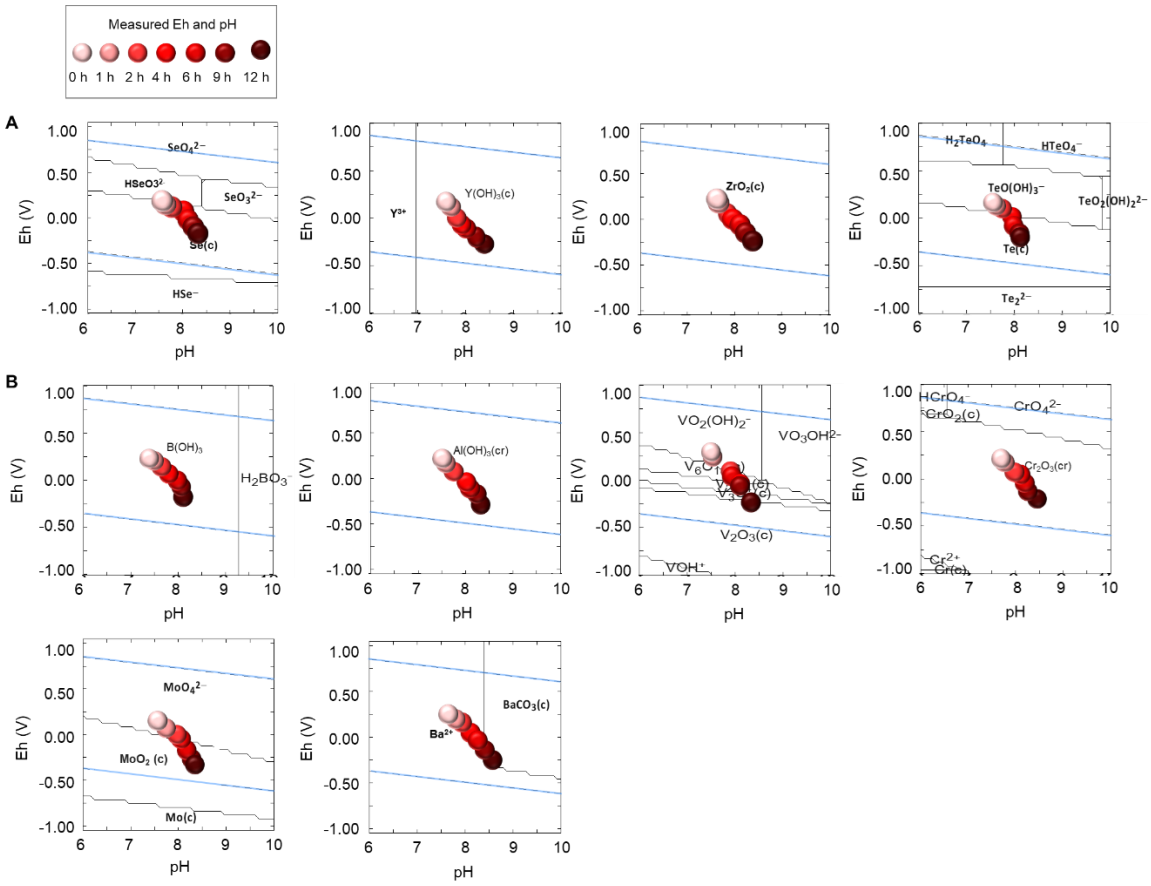

Fig. S23. Pourbaix diagram analyses and measurements of the Eh and pH in the *in vivo* conditions of amorphous NMs or no NM formation at pH 7.5. (*A*) Formation of amorphous NMs at pH 7.5. The species taken into account include: SeO_4^{2-}, $HSeO_3^{2-}$, SeO_3^{2-}, Se (c) and HSe^- for Se; Y^{3+} and $Y(OH)_3$ (c) for Y; ZrO_2(c) for Zr; H_2TeO_4, $HTeO_4^-$, $TeO(OH)_3^-$, $TeO_2(OH)_2^{2-}$, Te (c) and Te_2^{2-} for Te. (*B*) No NM formation pH at 7.5. The species taken into account include: $B(OH)_3$ and H_2BO_3 for B; $Al(OH)_3$ (cr) for Al; $VO_2(OH)_2^-$, VO_3OH^{2-}, V_6O_{13} (c), V_2O_4 (c), V_3O_5 (c), V_2O_3 (c) and VOH^+ for V; $HCrO_4^-$, CrO_2 (c), CrO_4^{2-}, Cr_2O_3 (cr) and Cr^{2+} for Cr; MoO_4^{2-}, MoO_2 (cr) and Mo (c) for Mo; Ba^{2+} and $BaCO_3$ (c) for Ba. The Eh and pH of the *in vitro* reactions were mapped (shown in the circle with the pink to red).

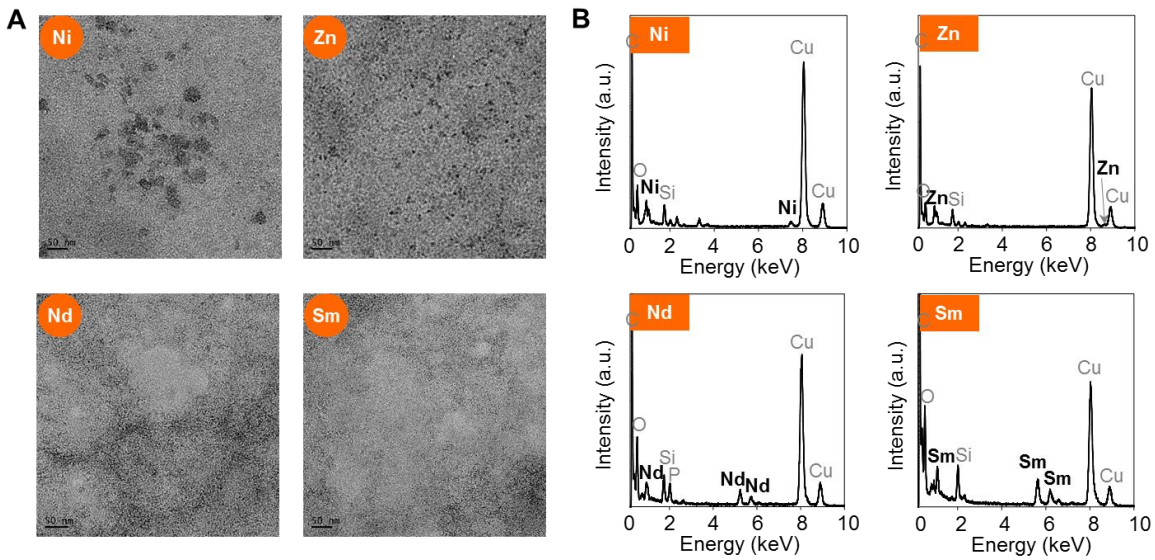

Fig. S24. TEM images and EDS graphs of the Ni, Zn, Nd and Sm NMs synthesized *in vitro* at initial pH 7.5 for 30 min. (*A*) TEM images of the NMs synthesized *in vitro* with their corresponding elements labeled in orange circle. (*B*) The EDS graphs of the NMs synthesized *in vitro*. The NMs synthesized *in vitro* with their corresponding elements labeled in orange square.

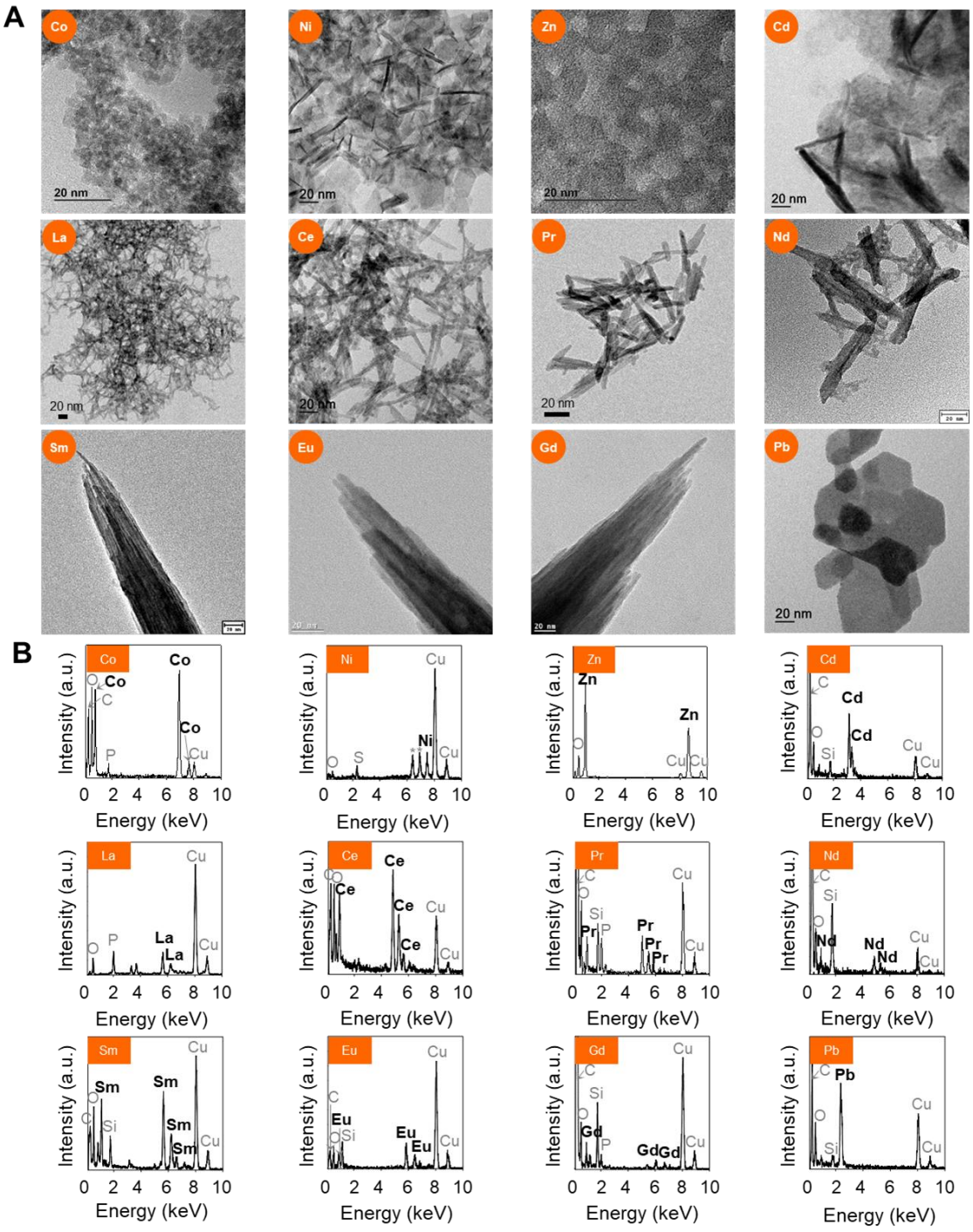

Fig. S25. TEM images and EDS graphs of the 12 crystalline NMs synthesized *in vitro* at the pH 7.5. (*A*) TEM images of the crystalline NMs synthesized *in vitro* with their corresponding elements labeled in orange circle. Scale bar, 20 nm. (*B*) The EDS graphs of the crystalline NMs synthesized *in vitro*. The amorphous NMs synthesized *in vitro* with their corresponding elements labeled in orange square.

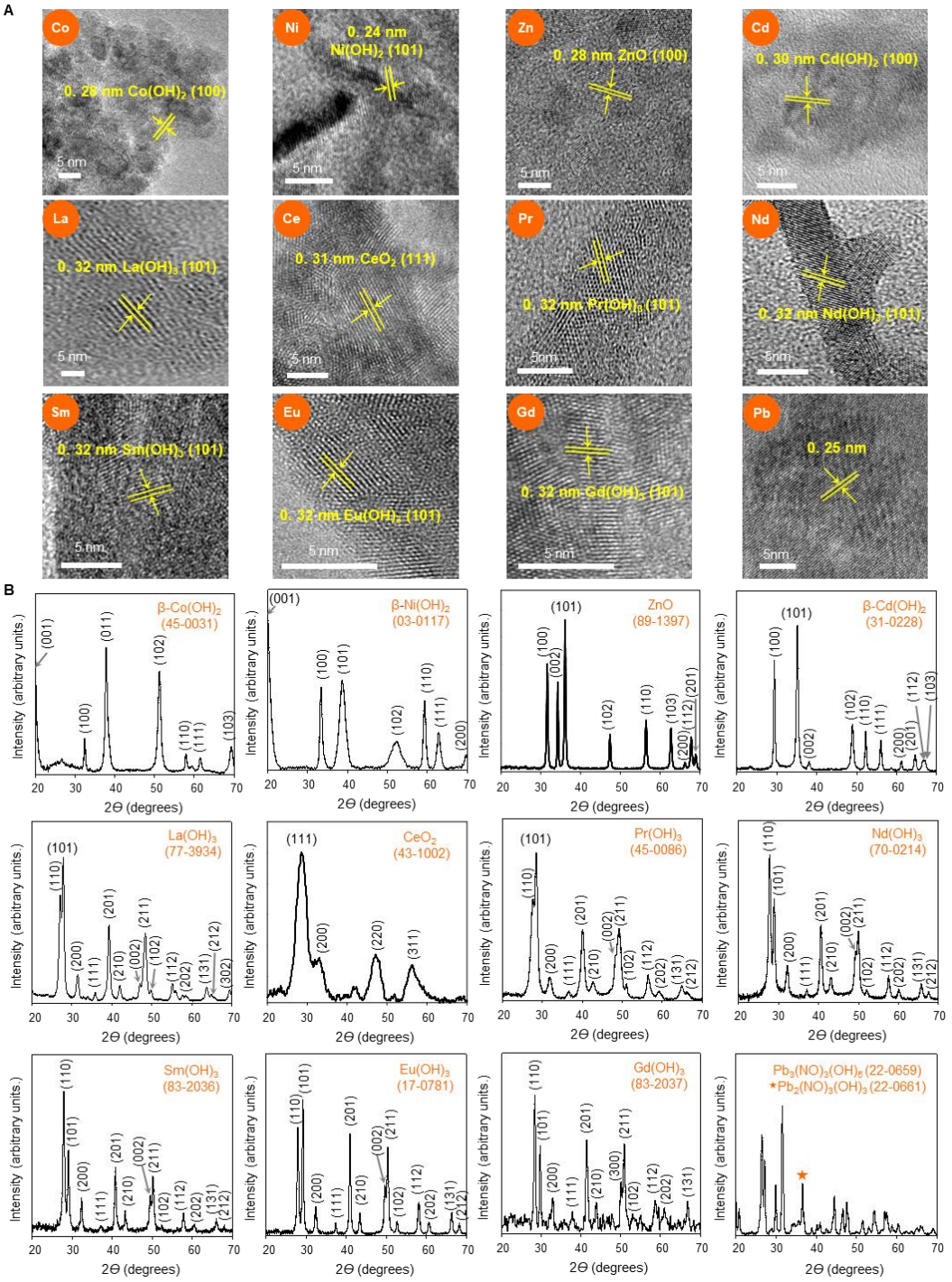

Fig. S26. HR-TEM images and the XRD patterns of 12 crystalline NMs synthesized *in vitro* at pH 7.5. (*A*) HR-TEM images of the crystalline NMs synthesized *in vitro* at pH 7.5 with their corresponding elements labeled in orange circle. The interplanar distance of the crystalline NM lattice and the Miller indices of crystallographic planes within parentheses are shown together. (*B*) The crystalline composition confirmation of the biosynthesized crystalline NMs were analyzed using XRD. The orange numbers in parentheses represent the JCPDS cards. The black numbers in parentheses represent Miller indices corresponding to each scattering peak.

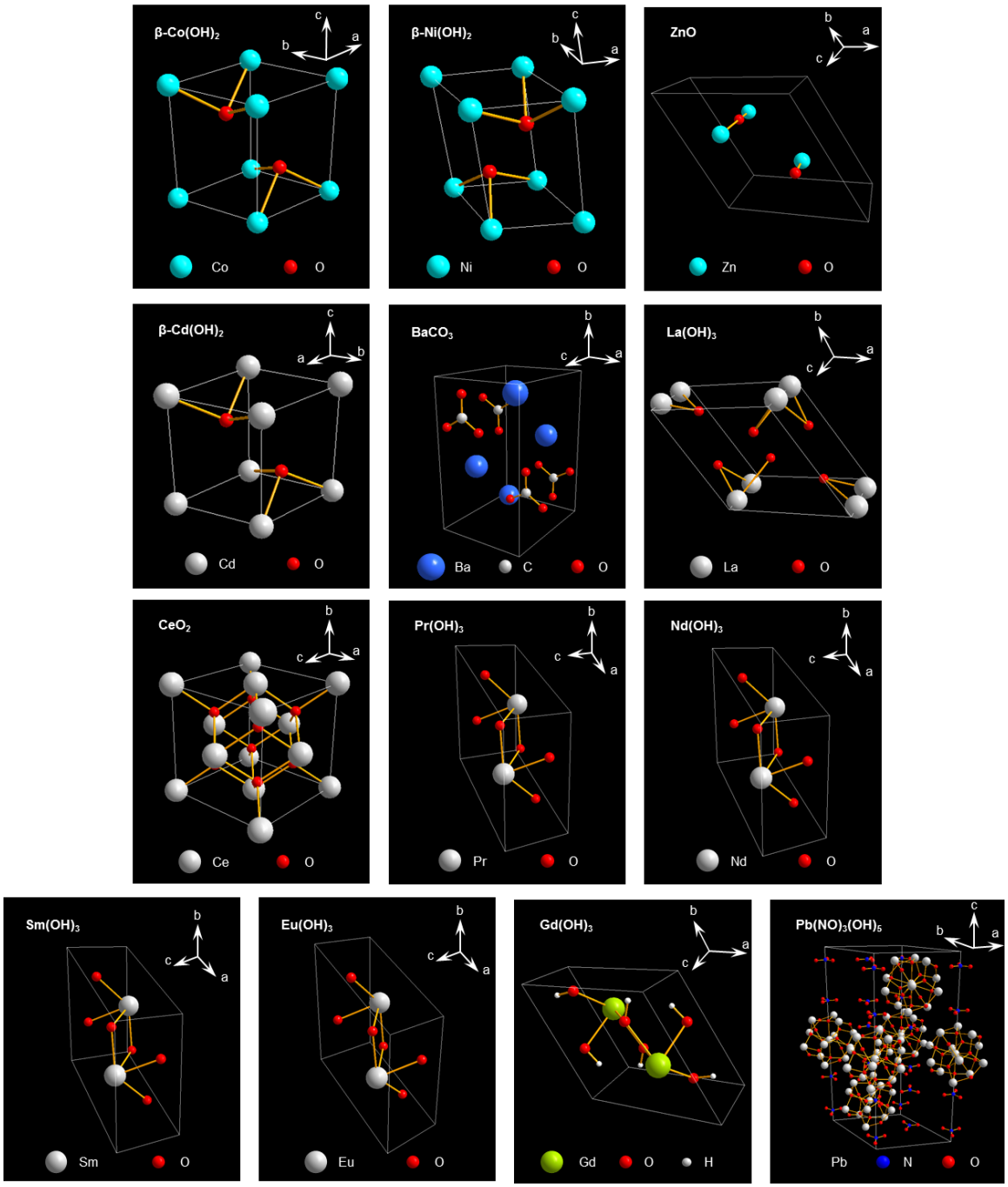

Fig. S27. Reconstructed crystal structures of 13 biosynthesized crystalline NMs at initial pH 7.5. Illustrations of crystalline structures of the biosynthesized crystalline NMs at initial pH 7.5 based on the XRD data. Colored spheres and sticks represent individual atoms and chemical bonds between the atoms, respectively.

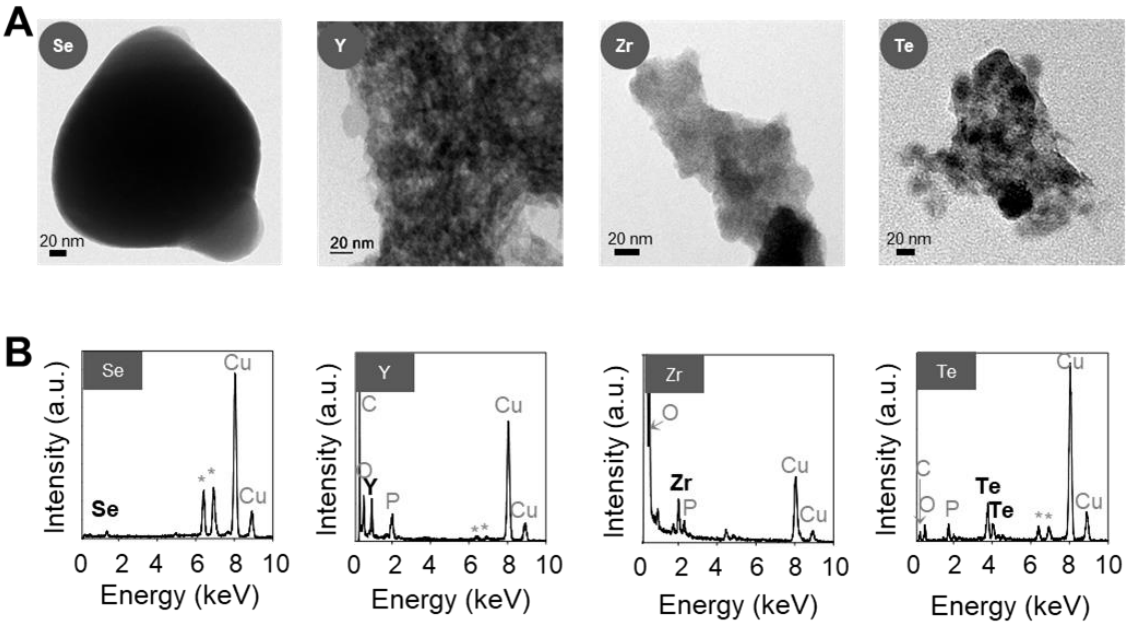

Fig. S28. TEM images and EDS graphs of the amorphous NMs synthesized *in vitro* at pH 7.5. (*A*) TEM images of the amorphous NMs synthesized *in vitro* with their corresponding elements labeled in gray circle. Scale bar, 20 nm. (*B*) The EDS graphs of the amorphous NMs synthesized *in vitro*. The amorphous NMs synthesized *in vitro* with their corresponding elements labeled in gray square.

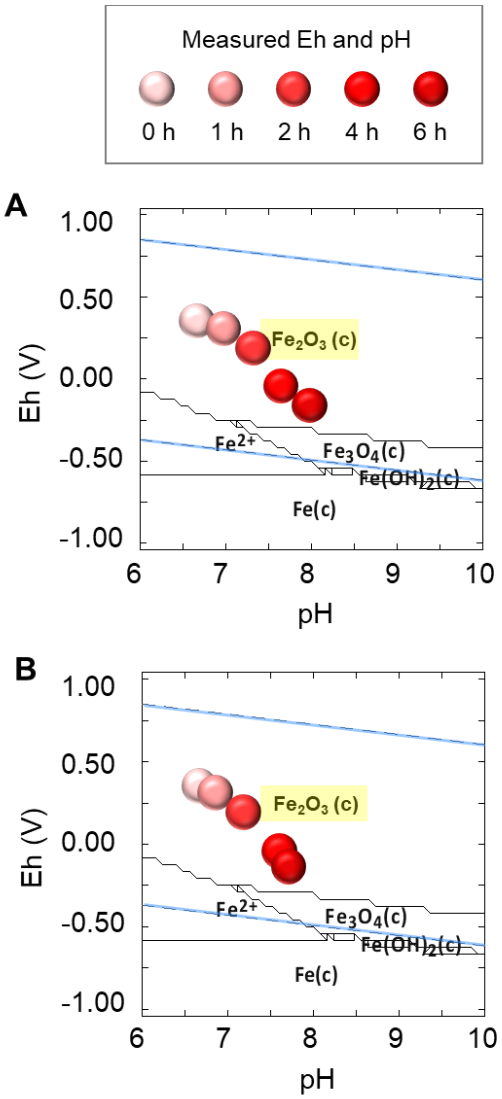

Fig. S29. Pourbaix diagram analyses and measurements of Eh and pH during *in vivo* and *in vitro* biosynthesis of α-Fe_2O_3 NM. (*A*) *In vivo* synthesis of α-Fe_2O_3 NM. The Eh and pH of the *in vivo* reactions were mapped (shown in the circle with the pink to red). (*B*) *In vitro* synthesis of α-Fe_2O_3 NM. The species taken into account include: Fe_2O_3 (c), Fe_3O_4 (c), Fe^{2+}, $Fe(OH)_2$ (c) and Fe (c) for Fe. The Eh and pH of the *in vitro* reactions were mapped (shown in the circle with the pink to red). The compositions of biosynthesized NM according to the XRD result (α-Fe_2O_3) is indicated by the yellow box.

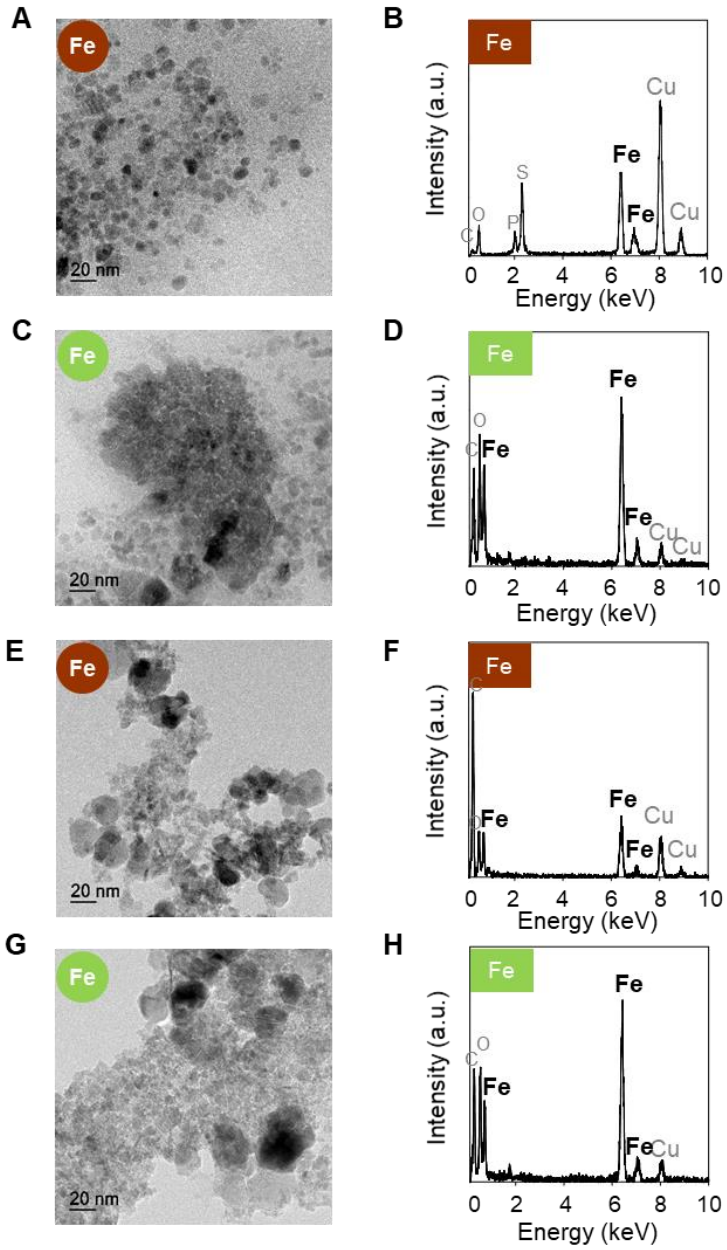

Fig. S30. TEM images and EDS analysis of α-Fe_2O_3, β-FeOOH and α-FeOOH NMs synthesized *in vivo* and *in vitro*. TEM image (*A*; shown with 20 nm scale bar) and EDS graph (*B*; with their corresponding element labeled in brown square) of α-Fe_2O_3, β-FeOOH and α-FeOOH NMs synthesized *in vivo*. TEM image (*C*; shown with 20 nm scale bar) and EDS graph (*D*; with their corresponding element labeled in light green square) of α-Fe_2O_3, β-FeOOH and α-FeOOH NMs synthesized *in vitro*. TEM image (*E*; shown with 20 nm scale bar) and EDS graph (*F*; with their corresponding element after calcination labeled in brown square) of α-Fe_2O_3 NM synthesized *in vivo* after calcination. TEM image (*G*; shown with 20 nm scale bar) and EDS graph (*H*; with their corresponding element after calcination labeled in light green square) of α-Fe_2O_3 NM synthesized *in vitro* after calcination.

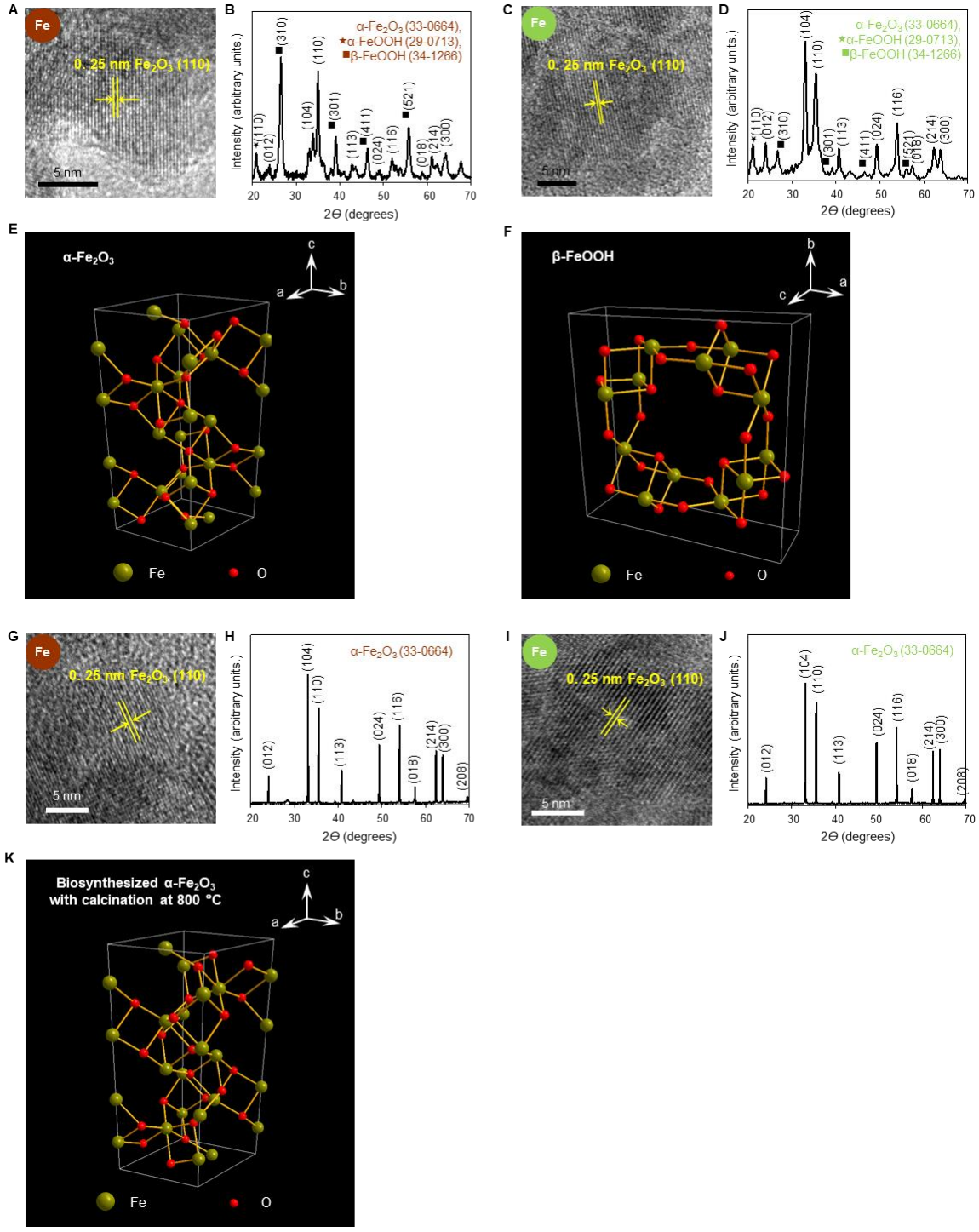

Fig. S31. HR-TEM images, XRD patterns and reconstructed crystal structures of the biosynthesized Fe NM. (*A*) HR-TEM image of α-Fe_2O_3, β-FeOOH and α-FeOOH NMs synthesized *in vivo* by 6-hour reaction with the corresponding element labeled in brown circle. (*B*) XRD analysis of the α-Fe_2O_3, β-FeOOH and α-FeOOH NMs synthesized *in vivo*. The brown numbers in parentheses represent the JCPDS cards. (*C*) HR-TEM image of the α-Fe_2O_3, β-FeOOH and α-FeOOH NMs synthesized *in vitro* by 6-hour reaction with the

corresponding element labeled light green circle. (*D*) XRD analysis of the α-Fe_2O_3 and β-FeOOH and α-FeOOH NMs synthesized *in vitro*. The light green numbers in parentheses represent the JCPDS cards. (*E*) Illustrations of crystalline structures of the biosynthesized α-Fe_2O_3 NM from XRD analysis data. (*F*) Illustrations of crystalline structures of the biosynthesized β-FeOOH NM from XRD analysis data. (*G*) HR-TEM image of *in vivo* synthesized α-Fe_2O_3 NM after calcination at 800°C. (*H*) XRD analysis of the *in vivo* synthesized α-Fe_2O_3 NM after calcination at 800°C. The brown numbers in parentheses represent the JCPDS card. (*I*) HR-TEM image of *in vitro* synthesized α-Fe_2O_3 NM after calcination at 800°C. (*J*) XRD analysis of the *in vitro* synthesized α-Fe_2O_3 NM after calcination. The light green numbers in parentheses represent the JCPDS card. (*K*) Illustrations of the crystalline structures of the biosynthesized crystalline α-Fe_2O_3 NM after calcination at 800°C from XRD analysis data. In the HR-TEM images, the interplanar distance of the lattice (indicated in yellow in *A*, *C*, *G* and *I*) and the Miller indices (shown in numbers in parentheses in *B*, *D*, *H* and *J*) of crystallographic planes within parentheses are shown together. In *E*, *F* and *K*, colored spheres and sticks represent individual atoms and chemical bonds between the atoms, respectively.

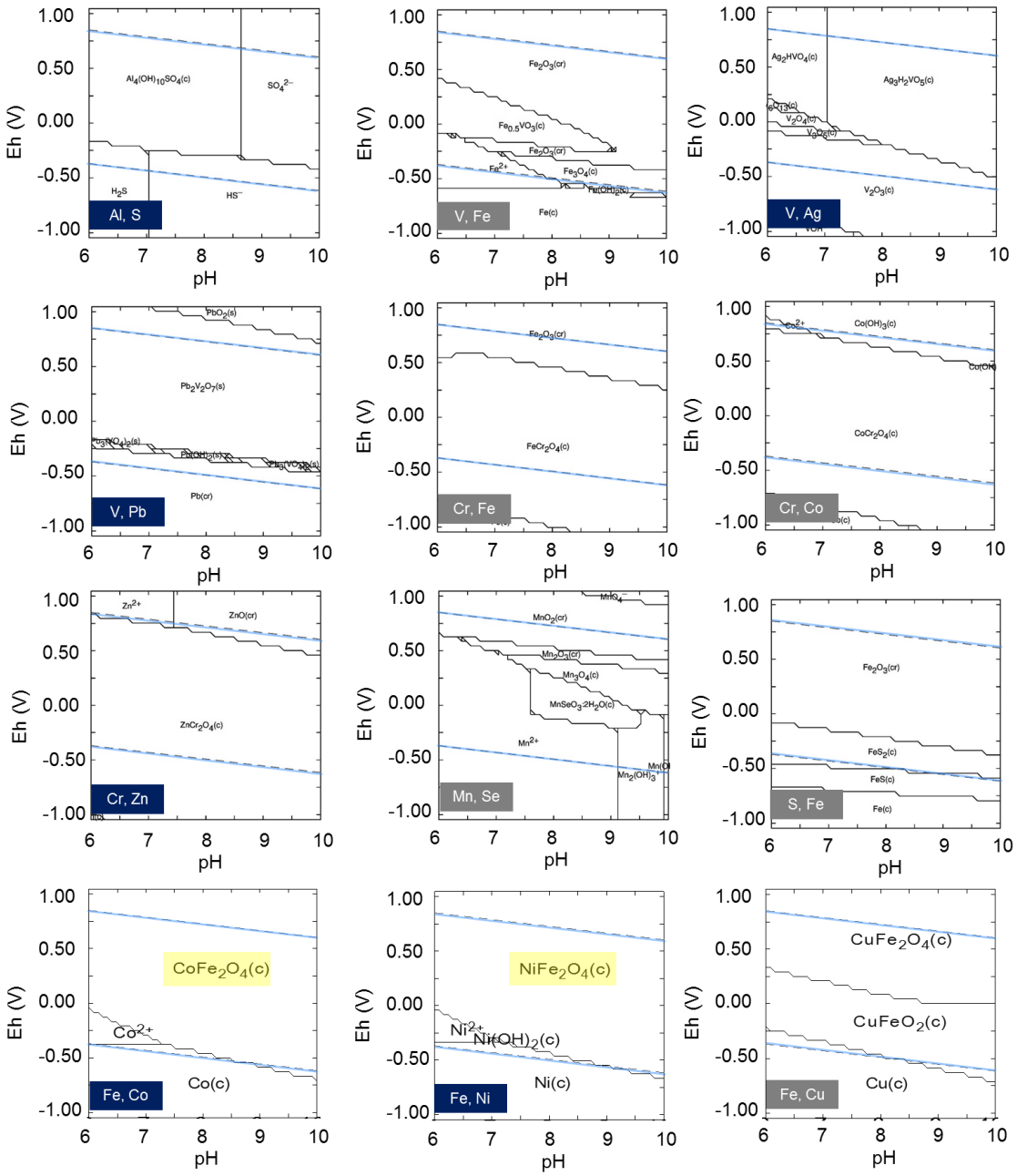

Fig. S32. Pourbaix diagrams for bi-elemental combinations resulting in multi-element crystalline NMs. Pourbaix diagrams of bi-elemental combinations predicted to form multi-element crystalline NMs. Those bi-elemental combinations tested for NM biosynthesis in this study are indicated in light dark blue square. Those bi-elemental combinations not tested are shown in gray square, while those NMs previously biosynthesized (8) are shown in light green square. The compositions of the multi-element crystalline NMs *in vivo* and *in vitro* according to the XRD results (Ag_2S, $CoFe_2O_4$, $NiFe_2O_4$, $ZnFe_2O_4$, $PbMoO_4$, Ag_2WO_4 and $PbWO_4$), which are indicated by the yellow box. (Fig. S32. continued)

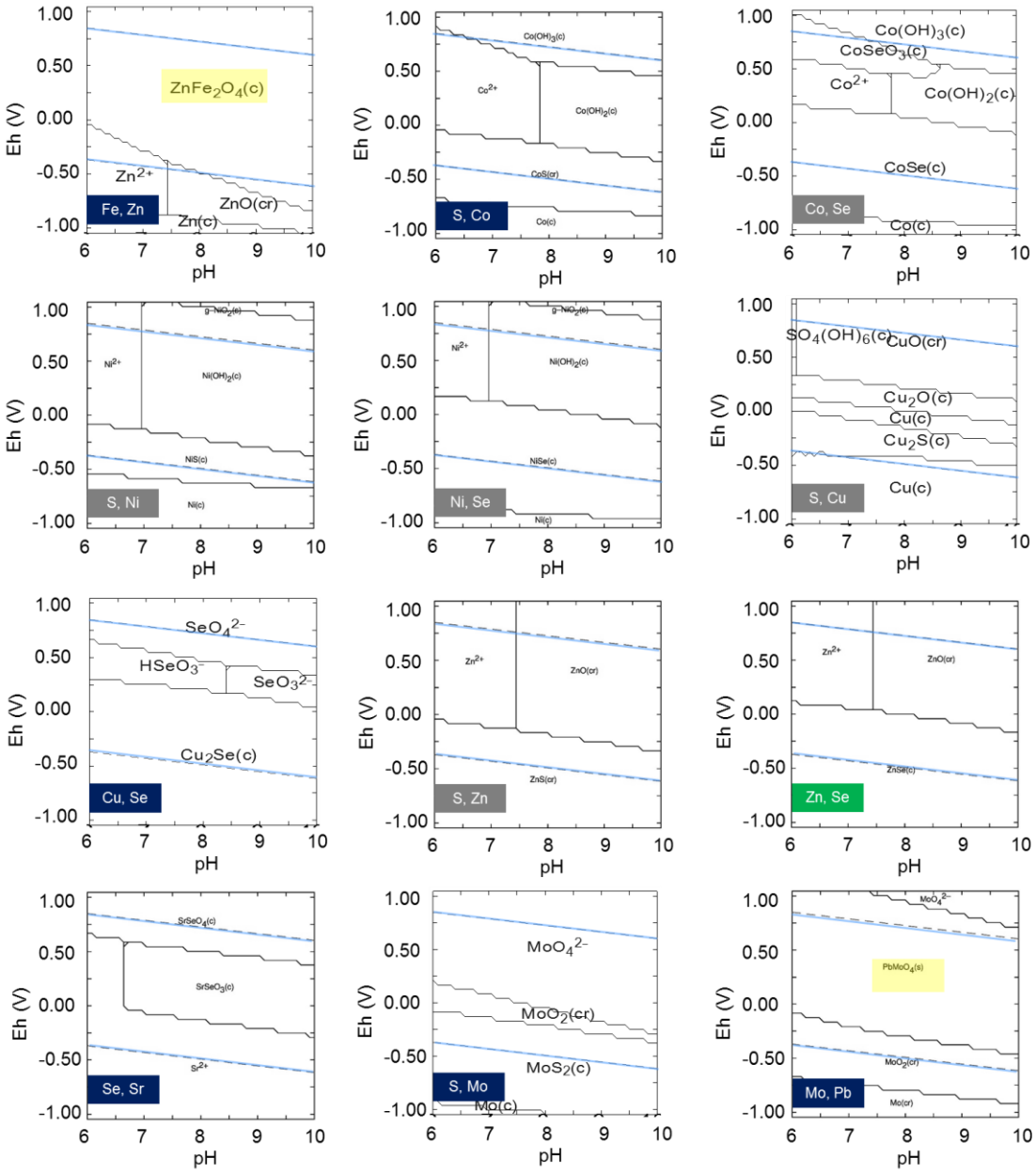
Eh (V)
pH
ZnFe2O4(c)
Zn2+
ZnO(cr)
Zn(c)
Fe, Zn
Co(OH)3(c)
Co2+
Co(OH)2(c)
CoS(cr)
Co(c)
S, Co
CoSeO3(c)
CoSe(c)
Co, Se
Ni2+
Ni(OH)2(c)
NiS(c)
Ni(c)
S, Ni
NiSe(c)
Ni, Se
SO4(OH)6(c)
CuO(cr)
Cu2O(c)
Cu(c)
Cu2S(c)
S, Cu
SeO4 2-
HSeO3-
SeO3 2-
Cu2Se(c)
Cu, Se
Zn2+
ZnO(cr)
ZnS(cr)
S, Zn
ZnSe(c)
Zn, Se
SrSeO4(c)
SrSeO3(c)
Sr2+
Se, Sr
MoO4 2-
MoO2(cr)
MoS2(c)
Mo(c)
S, Mo
PbMoO4(s)
Mo, Pb

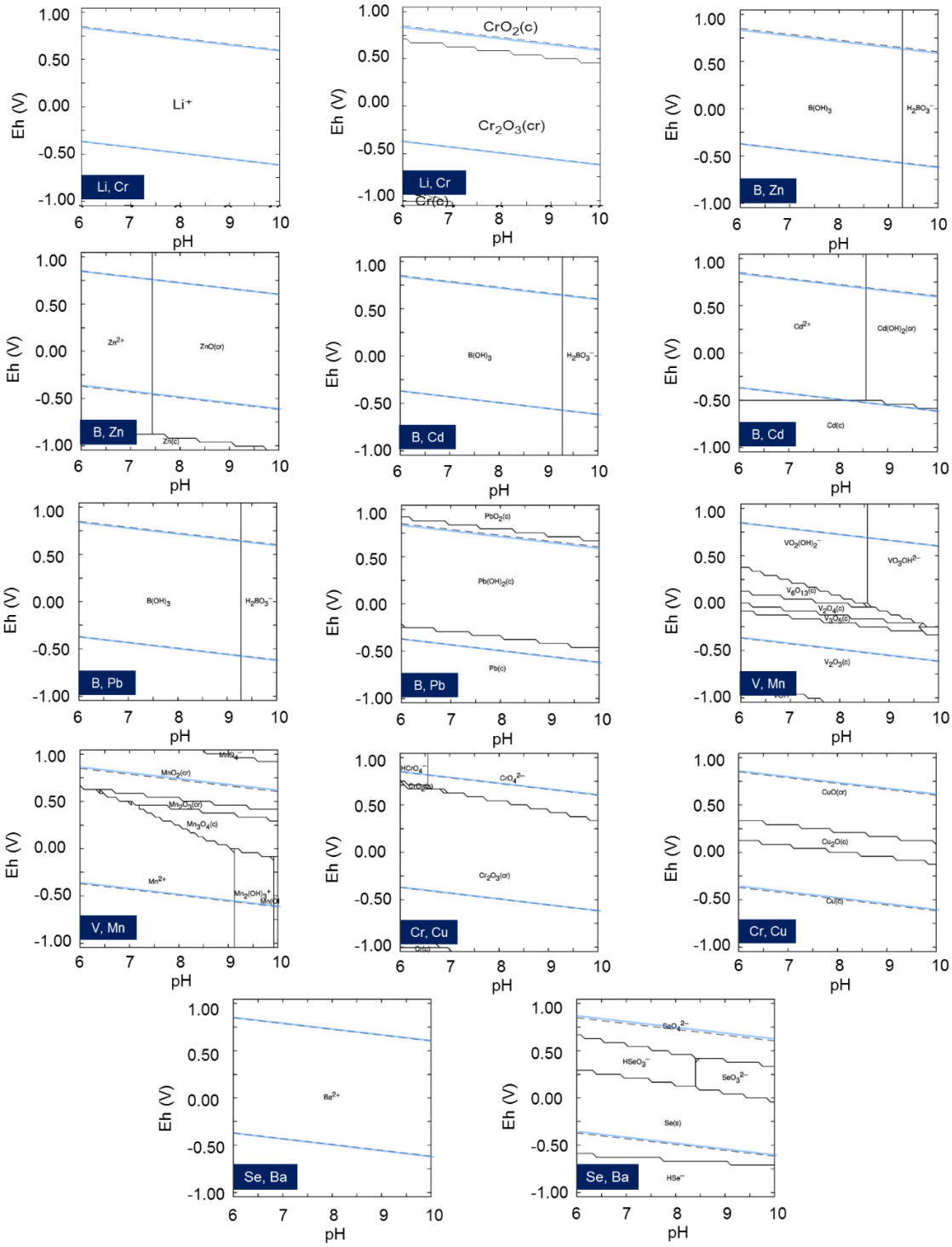

Fig. S33. Pourbaix diagrams of those element combinations that could not be predicted to form bi-elements. These element combinations for the corresponding bi-elements shown in blue square did not exist in the database, and thus could not be predicted by Pourbaix diagram analyses. (Fig. S33. continued)

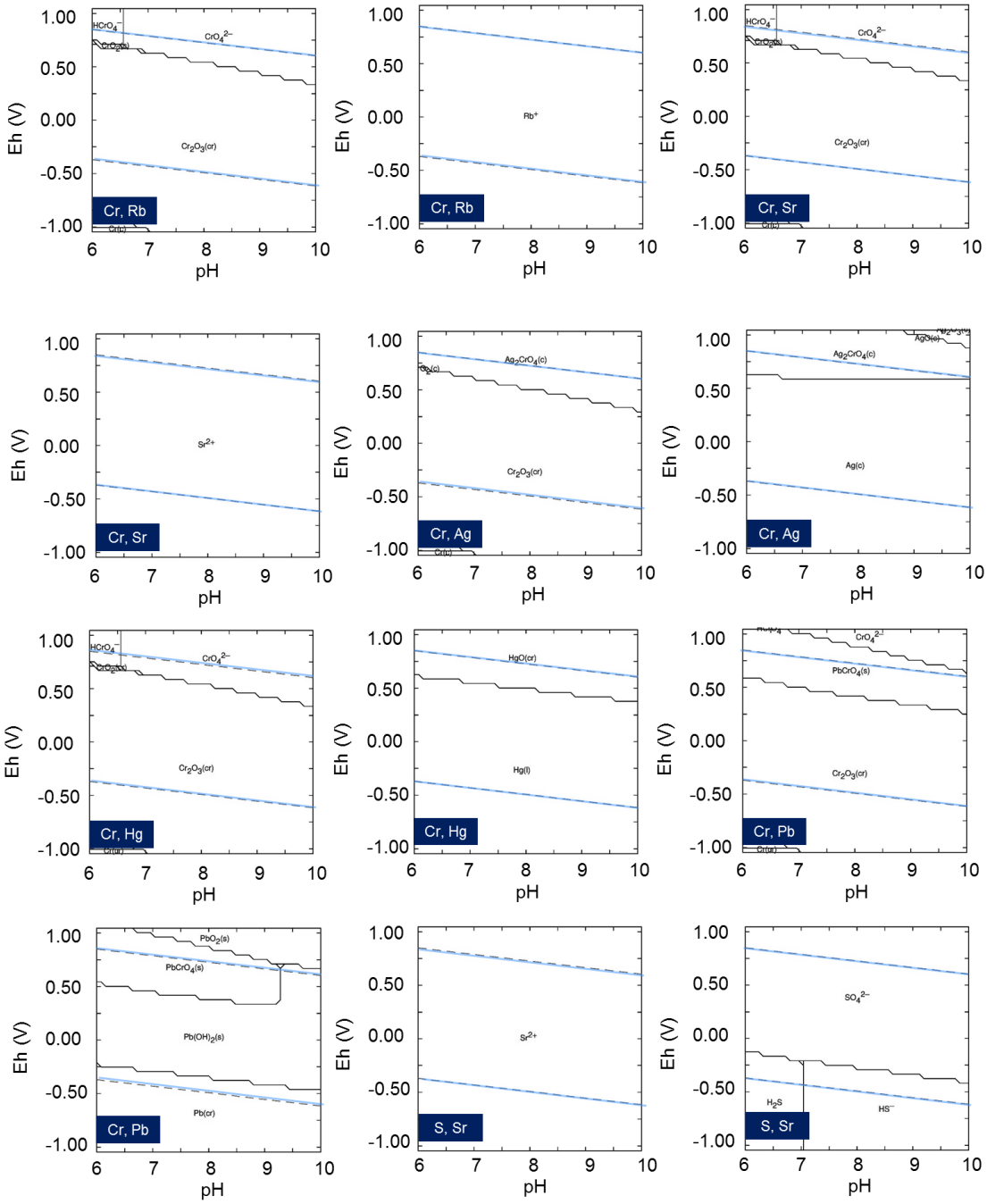
Cr, Rb
Cr, Rb
Cr, Sr
Cr, Sr
Cr, Ag
Cr, Ag
Cr, Hg
Cr, Hg
Cr, Pb
Cr, Pb
S, Sr
S, Sr
Eh (V)
pH
1.00
0.50
0.00
-0.50
-1.00
6
7
8
9
10
HCrO4−
CrO4 2−
Cr2O3(cr)
Cr(c)
Rb+
Sr2+
Ag2CrO4(c)
O2(c)
Ag(c)
HgO(cr)
Hg(l)
PbCrO4(s)
PbO2(s)
Pb(OH)2(s)
Pb(cr)
SO4 2−
H2S
HS−

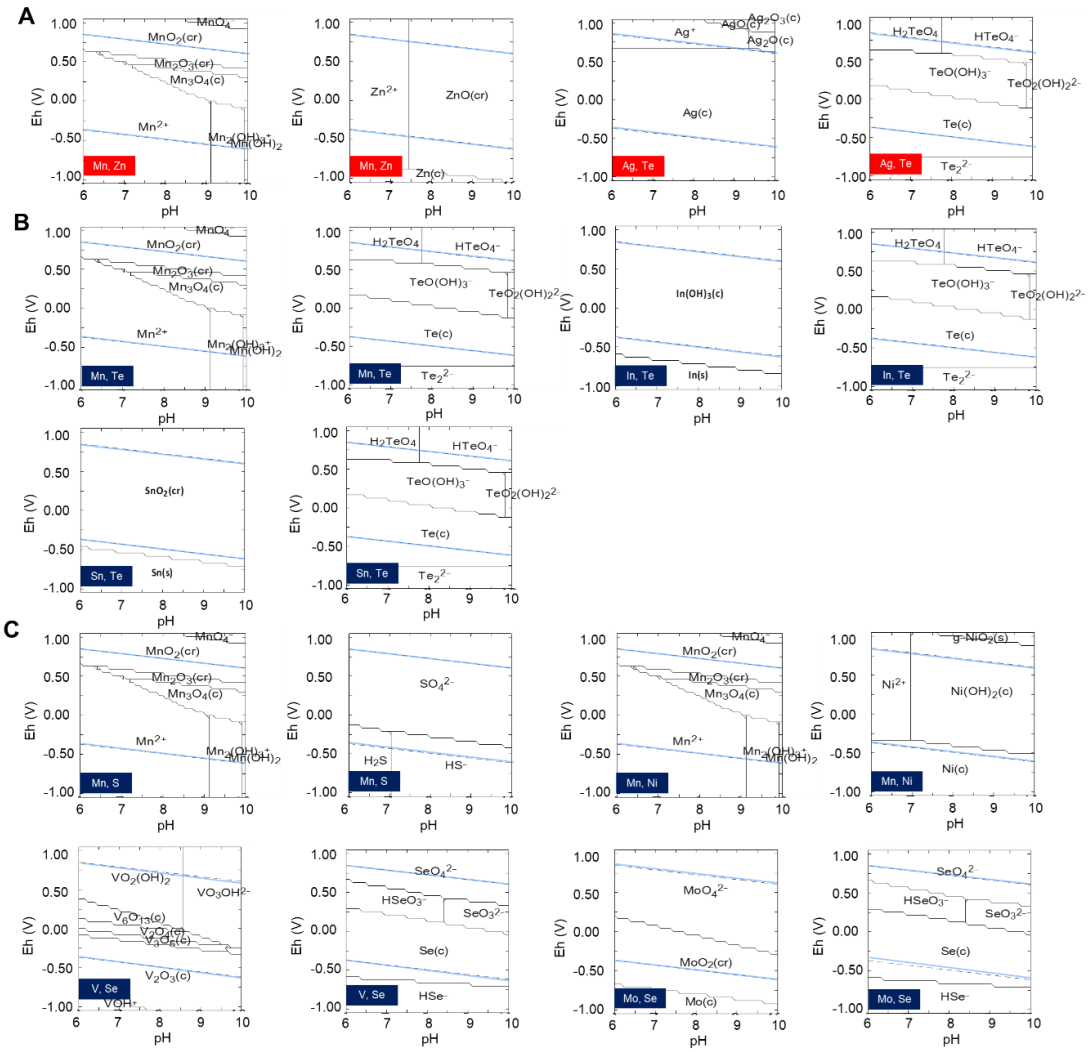

Fig. S34. Pourbaix diagrams of bi-elemental combinations for the multi-element crystalline NMs. (*A*) Pourbaix diagrams of bi-elemental combinations shown in red square for multi-element crystalline NMs synthesized *in vivo*. (*B*) Pourbaix diagrams of two separate single-element NMs synthesized *in vivo*. (*C*) Pourbaix diagrams of single-element NMs synthesized *in vivo*. The corresponding elements are shown in blue square (*B*, *C*). (Fig. S34. continued)

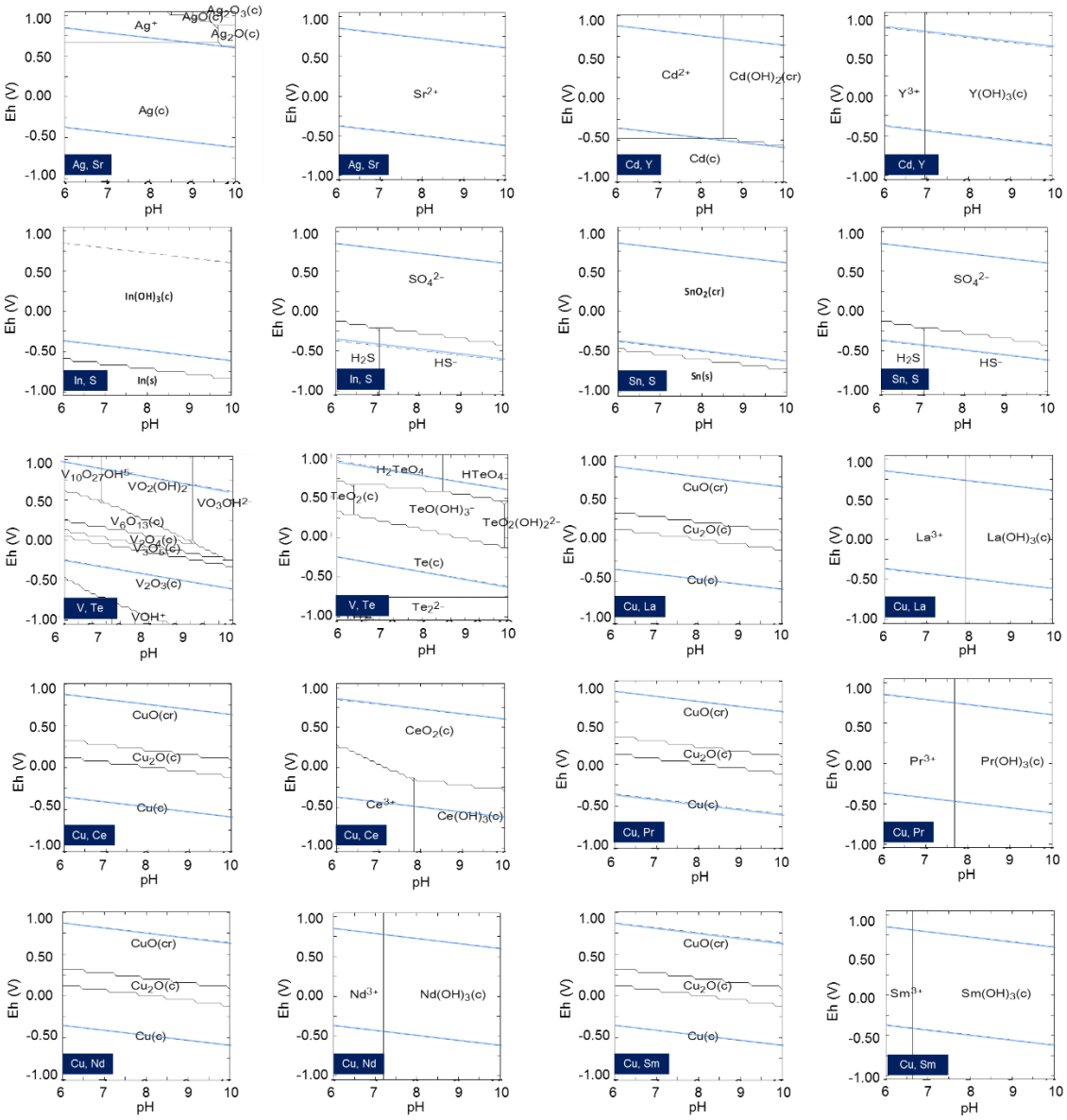

(Fig. S34. continued)

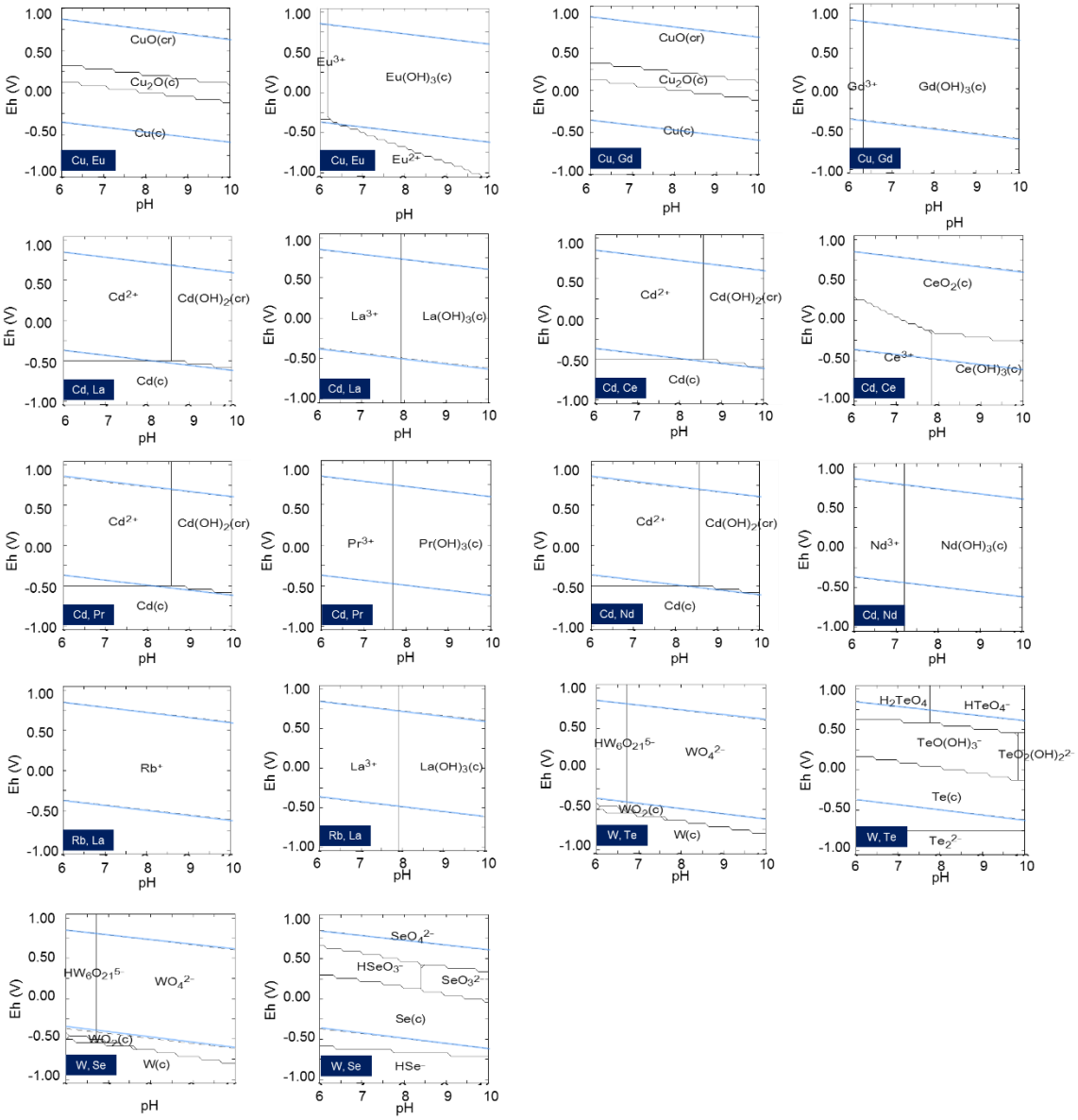
CuO(cr)
Cu2O(c)
Cu(c)
Cu, Eu
Eu3+
Eu(OH)3(c)
Eu2+
Cu, Eu
CuO(cr)
Cu2O(c)
Cu(c)
Cu, Gd
Gd3+
Gd(OH)3(c)
Cu, Gd
Cd2+
Cd(OH)2(cr)
Cd(c)
Cd, La
La3+
La(OH)3(c)
Cd, La
Cd2+
Cd(OH)2(cr)
Cd(c)
Cd, Ce
CeO2(c)
Ce3+
Ce(OH)3(c)
Cd, Ce
Cd2+
Cd(OH)2(cr)
Cd(c)
Cd, Pr
Pr3+
Pr(OH)3(c)
Cd, Pr
Cd2+
Cd(OH)2(cr)
Cd(c)
Cd, Nd
Nd3+
Nd(OH)3(c)
Cd, Nd
Rb+
Rb, La
La3+
La(OH)3(c)
Rb, La
HW6O21 5-
WO4 2-
WO2(c)
W(c)
W, Te
H2TeO4
HTeO4-
TeO(OH)3-
TeO2(OH)2 2-
Te(c)
Te2 2-
W, Te
HW6O21 5-
WO4 2-
WO2(c)
W(c)
W, Se
SeO4 2-
HSeO3-
SeO3 2-
Se(c)
HSe-
W, Se
Eh (V)
pH

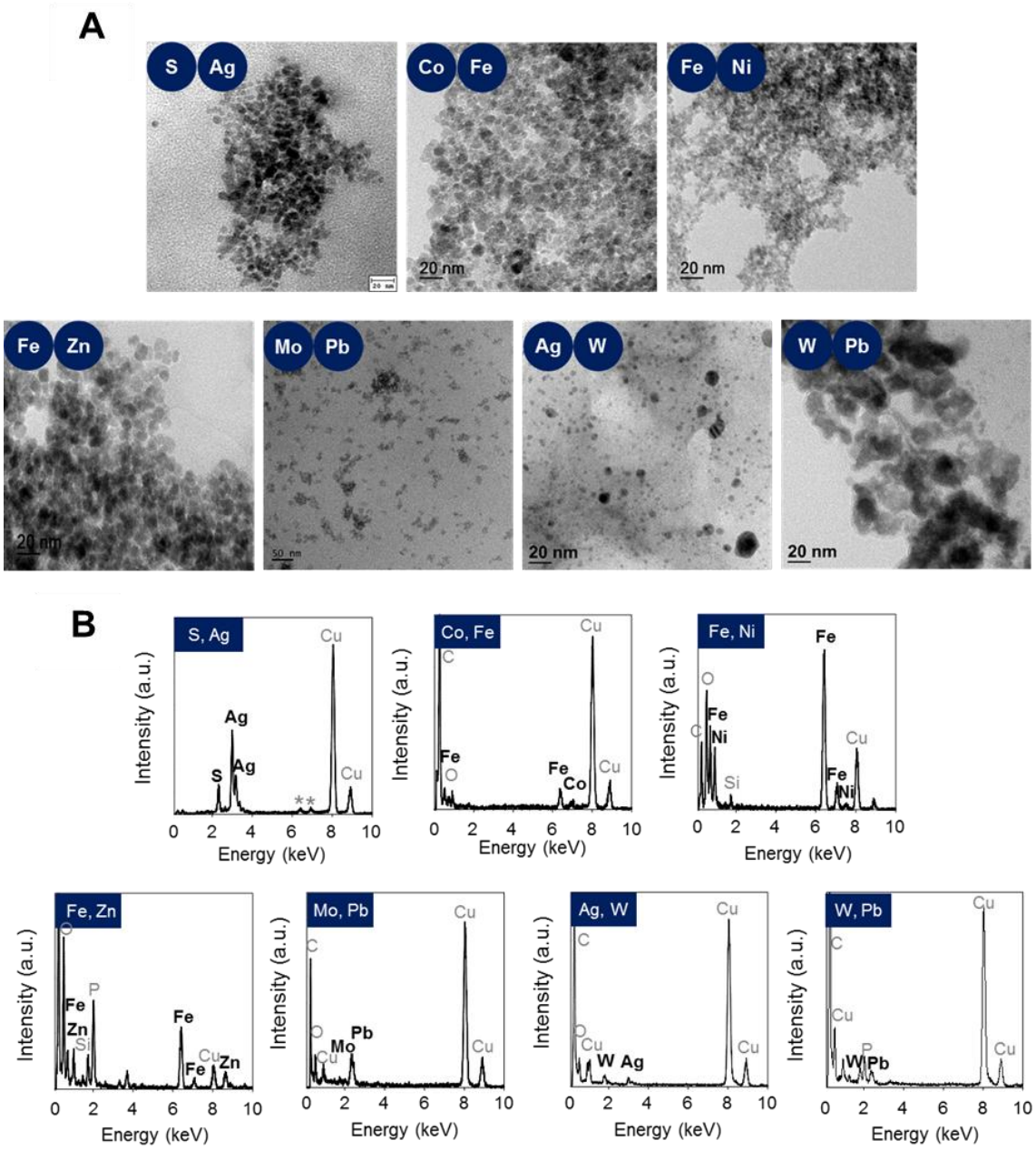

Fig. S35. TEM images and EDS graphs of the multi-element crystalline NMs synthesized *in vivo*. (*A*) TEM images of the multi-element crystalline NMs synthesized *in vivo* with their corresponding elements labeled in dark blue circle. Scale bar, 20 nm. (*B*) The EDS graphs of the multi-element crystalline NMs synthesized *in vivo*. The crystalline NMs synthesized *in vivo* with their corresponding elements labeled in dark blue square.

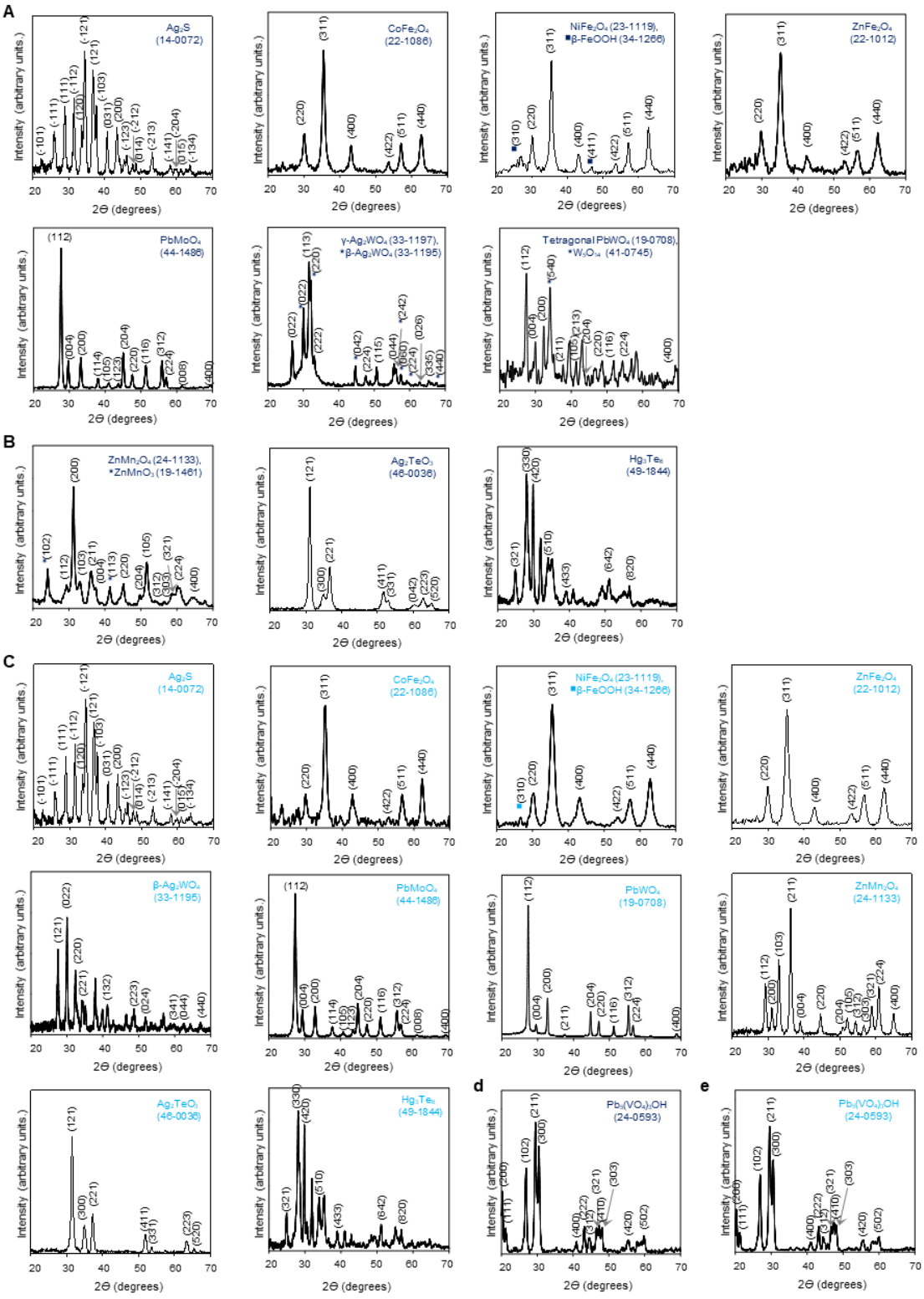

Fig. S36. XRD patterns of multi-element crystalline NMs biosynthesized *in vivo* and *in vitro*. (*A*) The crystalline compositions of multi-element NMs synthesized *in vivo* at pH 6.5. The dark blue numbers in parentheses represent the JCPDS cards. Because cell debris existed for NMs synthesized *in vivo*, background scattering from the some organic

components was also recorded in the XRD patterns. (*B*) The crystalline compositions of multi-element NMs synthesized *in vivo* at pH 6.5. These NMs were predicted not producible from Pourbaix diagram analysis, but could be biosynthesized. The dark blue numbers in parentheses represent the JCPDS cards. (*C*) The crystalline compositions of multi-element NMs synthesized *in vitro* at pH 6.5. The light blue numbers in parentheses represent the JCPDS cards. (*D*) The crystalline compositions of $Pb_5(VO_4)_3OH$ NM synthesized *in vivo* at pH 7.5. The dark blue numbers in parentheses represent the JCPDS cards. (*E*) The crystalline compositions of $Pb_5(VO_4)_3OH$ NM synthesized *in vitro* at pH 7.5. The black numbers in parentheses represent Miller indices corresponding to each scattering peak.

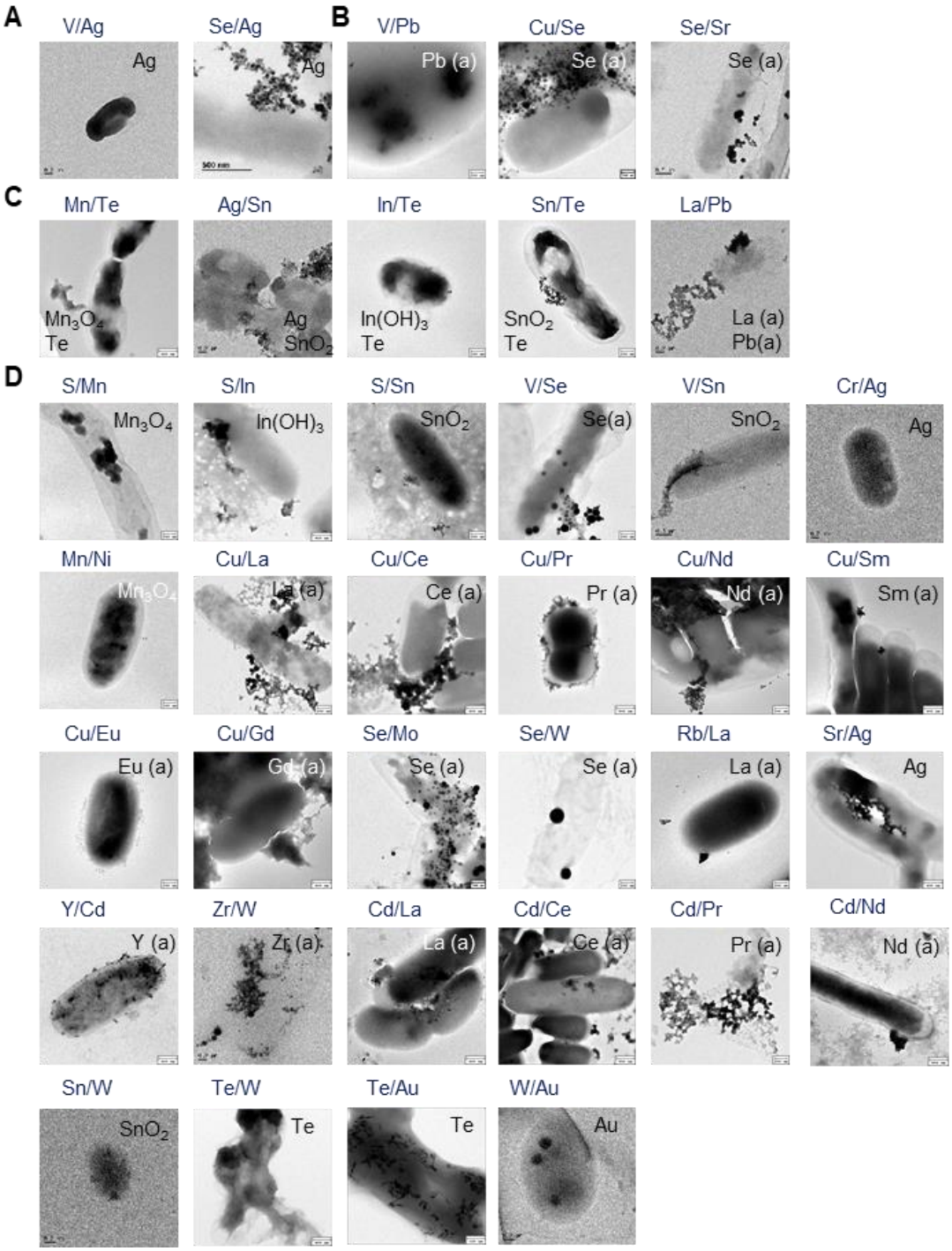

Fig. S37. TEM images of various single-element NMs synthesized *in vivo*. (*A*) TEM images of crystalline Ag NM synthesized *in vivo*. (*B*) TEM images of single amorphous NMs synthesized *in vivo*. (*C*) TEM images of two separate single-element NMs synthesized *in vivo*. (*D*) TEM images of single-element NMs synthesized *in vivo*. Amorphous NMs are indicated with (a) next to the element name.

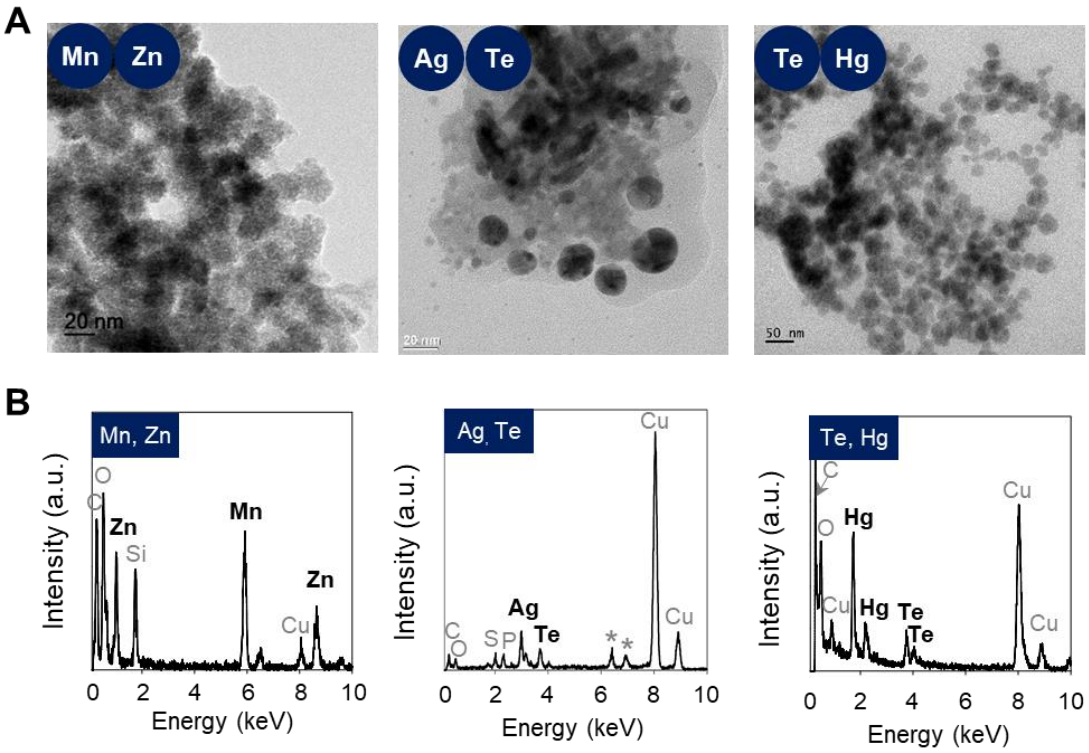

Fig. S38. TEM images and EDS graphs of the multi-element crystalline NMs synthesized *in vivo*. These NMs were biosynthesized *in vivo* even though they were predicted not producible from Pourbaix diagram analysis. (*A*) TEM images of the multi-element crystalline NMs synthesized *in vivo* with their corresponding elements labeled in dark blue circle. (*B*) The EDS graphs of the multi-element crystalline NMs synthesized *in vivo*. The crystalline NMs synthesized *in vivo* with their corresponding elements labeled in dark blue square.

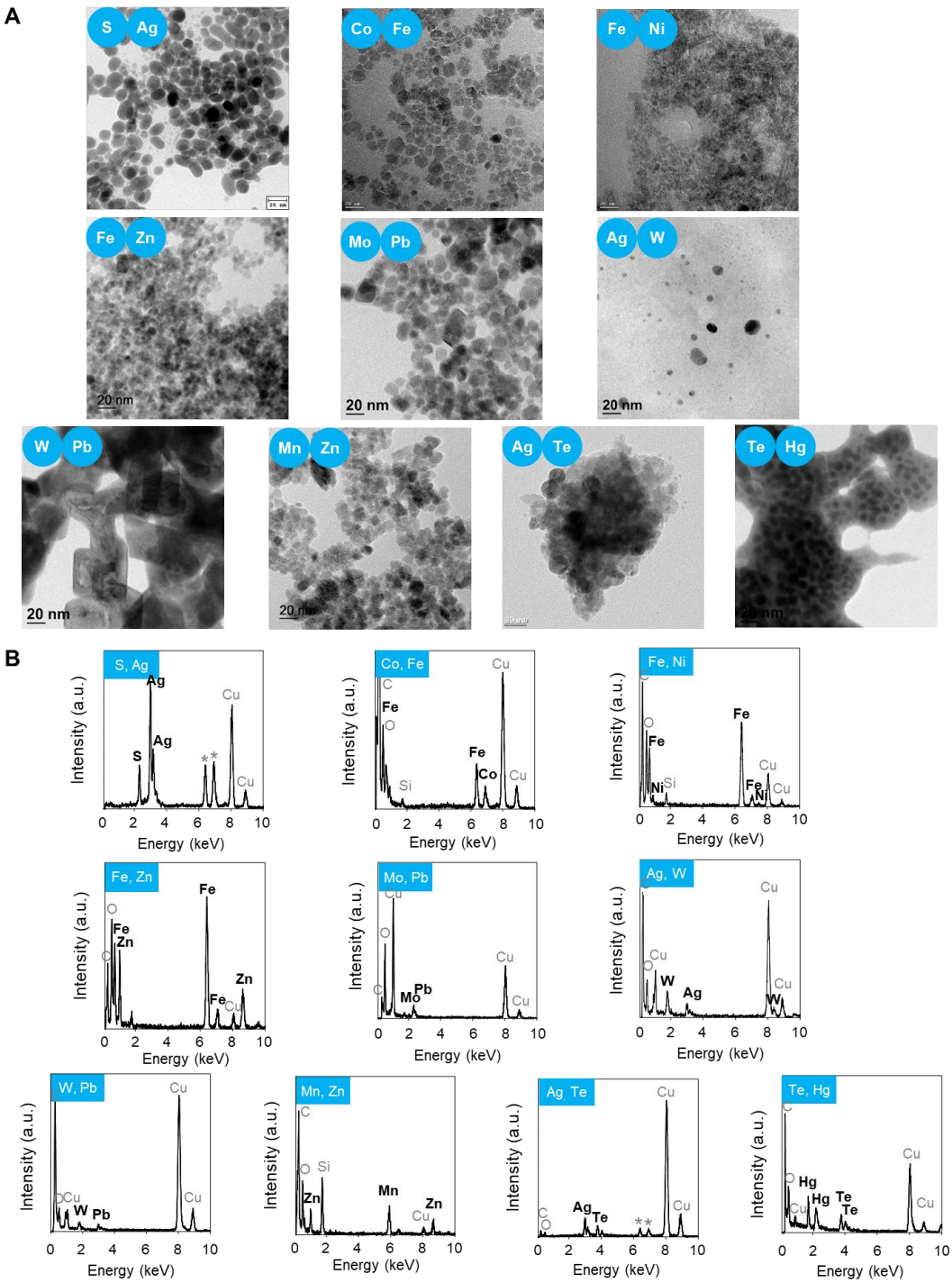

Fig. S39. TEM images and EDS graphs of multi-element crystalline NMs synthesized *in vitro*. (*A*) TEM images of multi-element crystalline NMs synthesized *in vitro* with their corresponding elements labeled in light blue circle. Scale bar, 20 nm. (*B*) The EDS graphs of multi-element crystalline NM synthesized *in vitro*. The crystalline NMs synthesized *in vitro* with their corresponding elements labeled in light blue square.

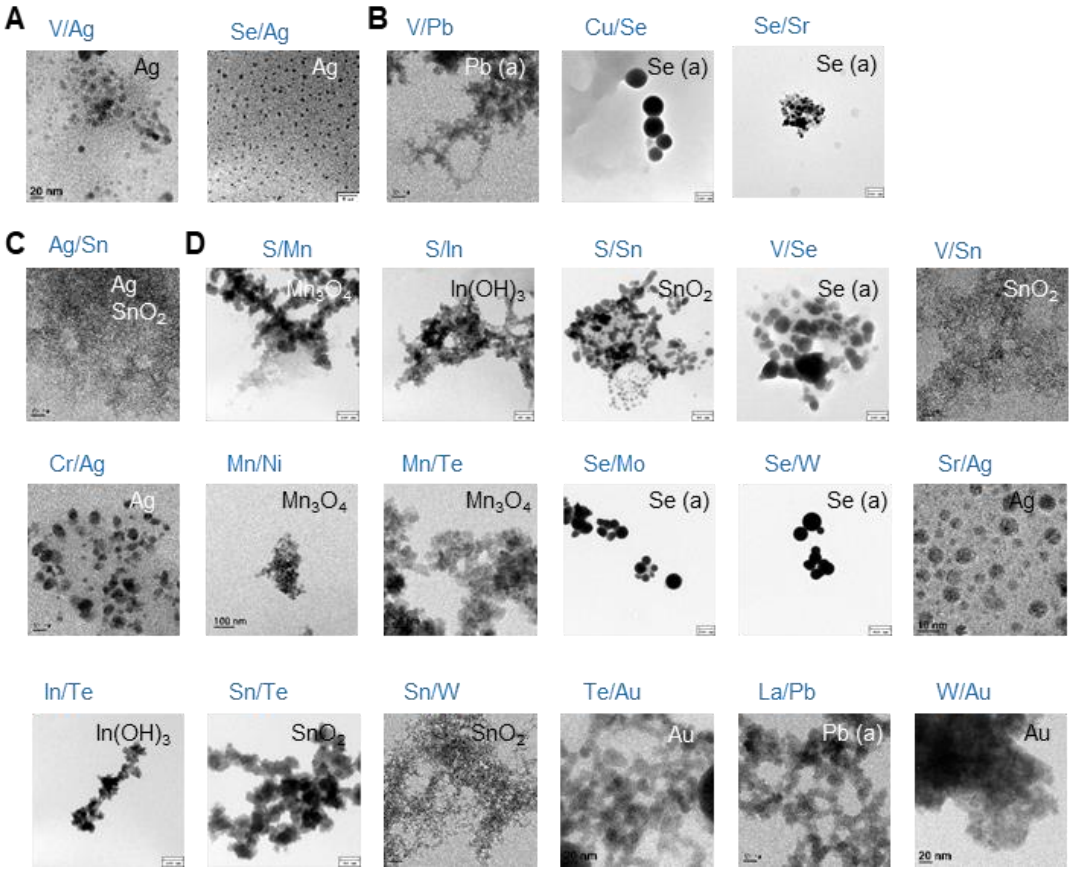

Fig. S40. TEM images of various single-element NMs synthesized *in vitro*. (*A*) TEM images of crystalline Ag NM synthesized *in vitro*. (*B*) TEM images of single amorphous NMs synthesized *in vitro*. (*C*) TEM images of two separate single-element NMs synthesized *in vitro*. (*D*) TEM images of single-element NMs synthesized *in vitro*. Amorphous NMs are indicated with (a) next to the element name.

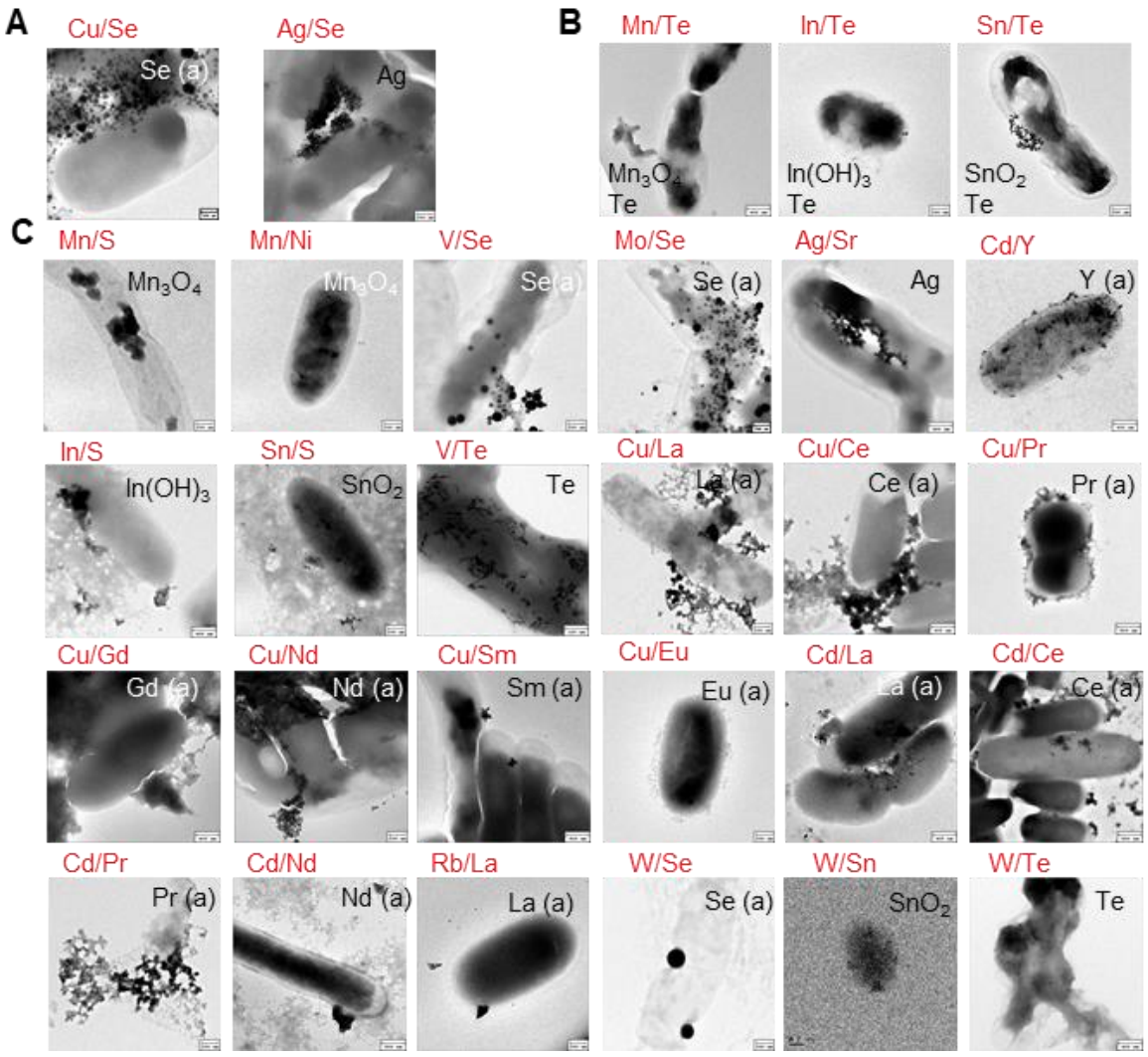

Fig. S41. TEM images of various single-element NMs synthesized *in vivo* at pH 7.5. (*A*) TEM images of crystalline Ag NM synthesized *in vivo*. (*B*) TEM images of two separate single-element NMs synthesized *in vivo. (C*) TEM images of single-element NMs synthesized *in vivo*. Amorphous NMs are indicated with (a) next to the element name.

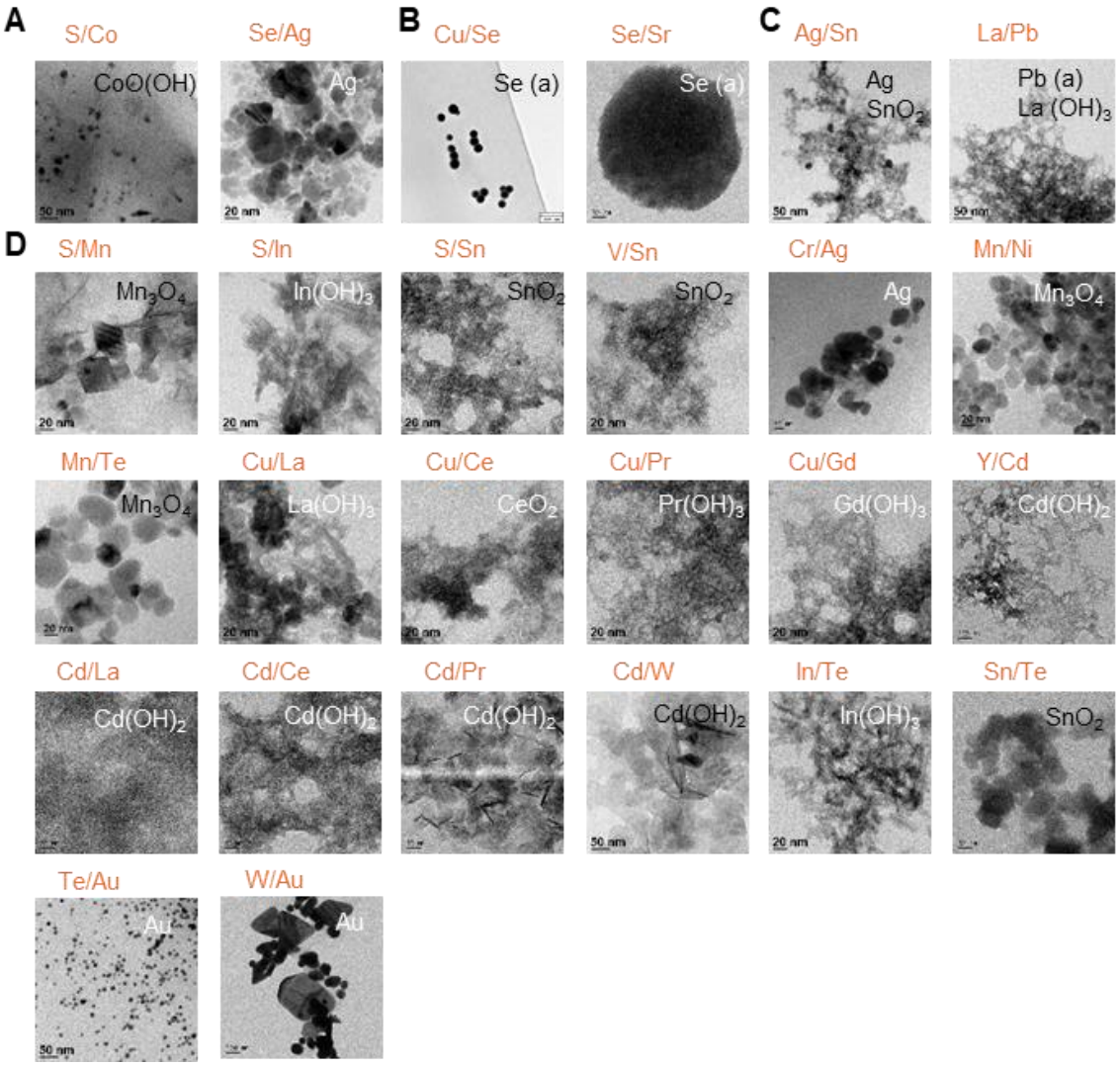

Fig. S42. TEM images of various single-element NMs synthesized *in vitro* at pH 7.5. (*A*) TEM images of single crystalline NMs synthesized *in vitro*. (*B*) TEM images of single amorphous Se NM synthesized *in vitro*. (*C*) TEM images of two separate single-element NMs synthesized *in vitro*. (*D*) TEM images of single-element NMs synthesized *in vitro*. Amorphous NMs are indicated with (a) next to the element name.

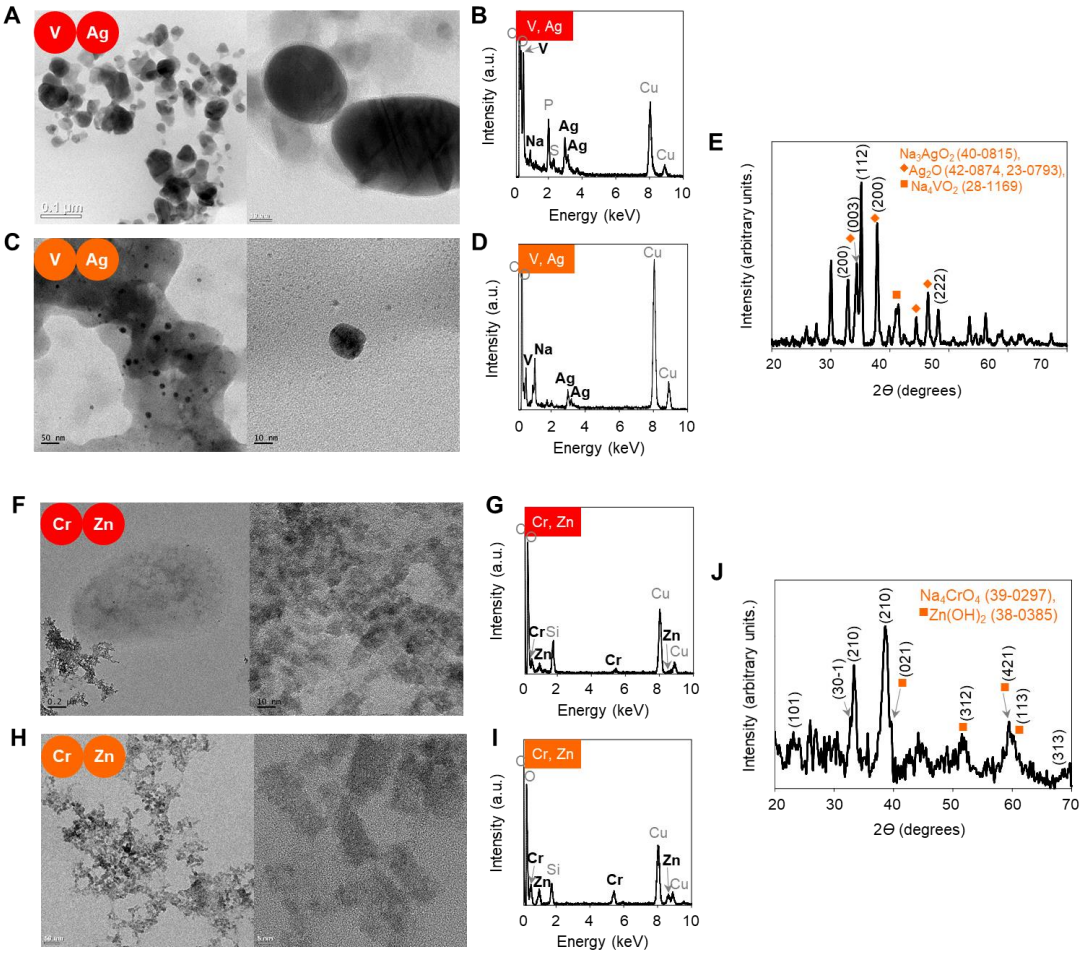

Fig. S43. TEM images, EDS graphs and XRD patterns of V/Ag and Cr/Zn bi-elemental combinations resulting in formation of crystalline NMs *in vivo* and *in vitro* at pH 7.5. For each TEM result with indicated bi-elements, the left is the TEM image and the right is the HR-TEM image. TEM images (*A*) and EDS graph (*B*; with their corresponding element labeled in red square) of Na_4VO_2, Na_3AgO_2 and Ag_2O NMs synthesized *in vivo*. TEM images (*C*) EDS graph (*D*; with their corresponding element labeled in orange square) and XRD patterns (*E*) of Na_4VO_2, Na_3AgO_2 and Ag_2O NMs synthesized *in vitro*. The orange numbers in parentheses represent the JCPDS cards. The black numbers in parentheses represent Miller indices corresponding to each scattering peak. TEM images (*F*) and EDS graph (*G*; with their corresponding element labeled in red square) of Na_4CrO_4 and $Zn(OH)_2$ NMs synthesized *in vivo*. TEM images (*H*) EDS graph (*I*; with their corresponding element labeled in orange square) and XRD patterns (*J*) of Na_4CrO_4 and $Zn(OH)_2$ NMs synthesized *in vitro*.

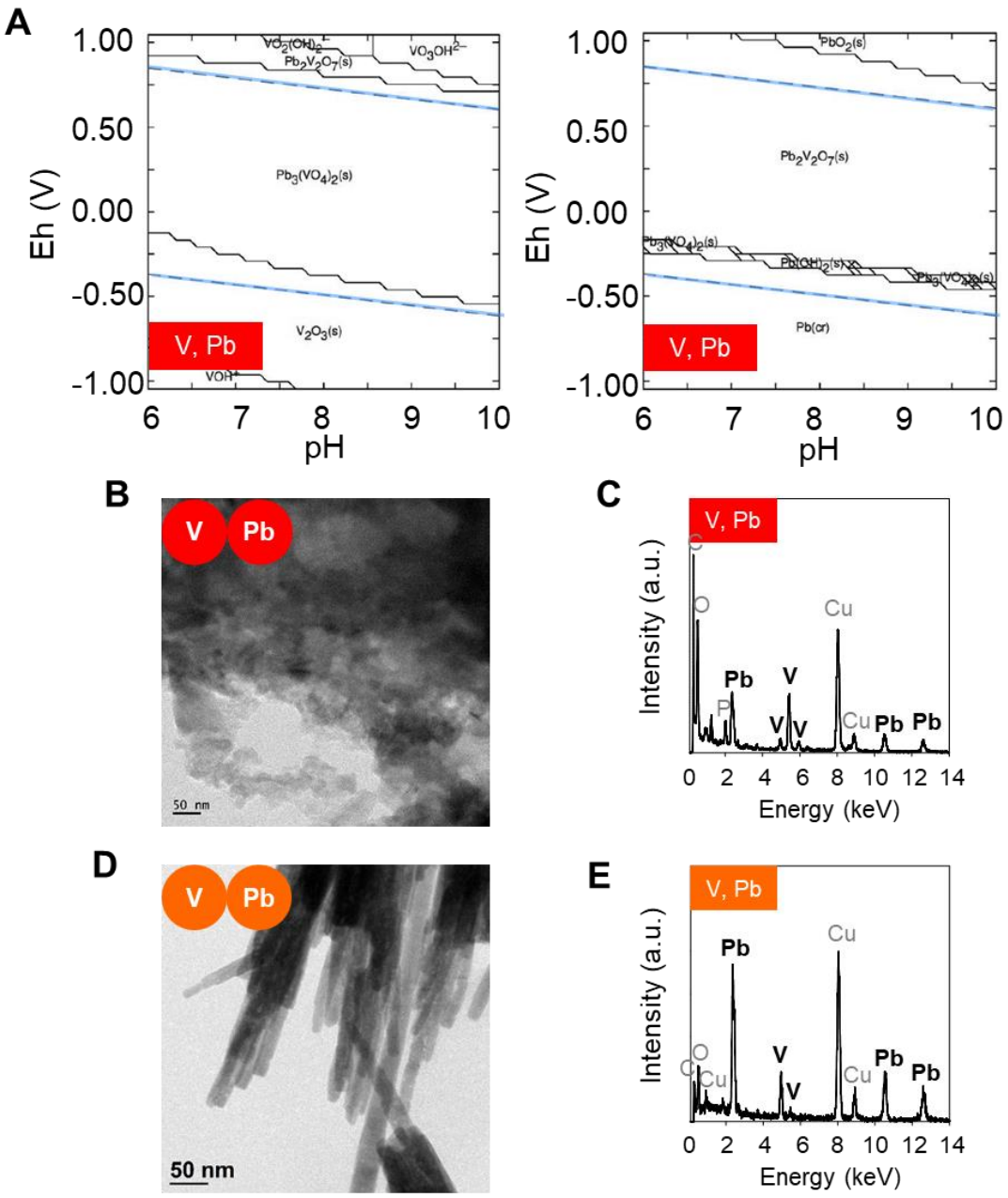

Fig. S44. Pourbaix diagrams for V/Pb, and TEM images and EDS graphs of $Pb_5(VO_4)_3OH$ NM synthesized *in vivo* and *in vitro* at pH 7.5. (*A*) Pourbaix diagrams for V/Pb during biosynthesis crystalline NMs. The predicted compositions of multi-element NMs taken into account include $Pb_3(VO_4)_2$ and $Pb_2V_2O_7$. (*B*) TEM image of $Pb_5(VO_4)_3OH$ NM synthesized *in vivo* with the corresponding elements labeled in red circle. (*C*) The EDS graph of $Pb_5(VO_4)_3OH$ NM synthesized *in vivo* with the corresponding elements labeled in red square. (*D*) TEM image of $Pb_5(VO_4)_3OH$ NM synthesized *in vitro* with the corresponding elements labeled in orange circle. (*E*) The EDS graph of $Pb_5(VO_4)_3OH$ NM synthesized *in vitro* with the corresponding elements labeled in orange square.

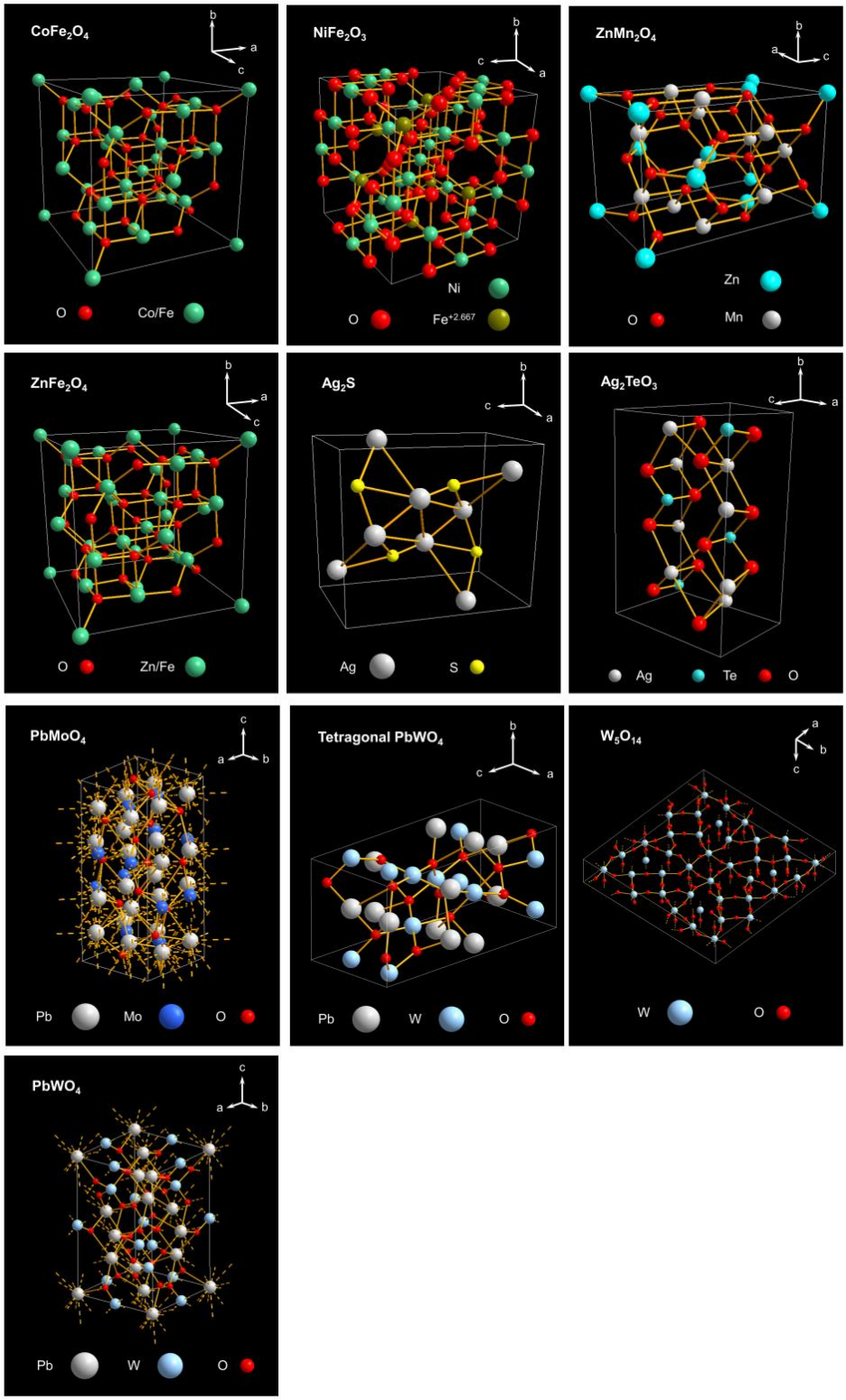

Fig. S45. Reconstructed crystal structures of biosynthesized multi-element crystalline NMs. Illustrations of crystalline structures of the biosynthesized multi-element NMs based on the XRD data. Colored spheres and sticks represent individual atoms and chemical bonds between the atoms, respectively.

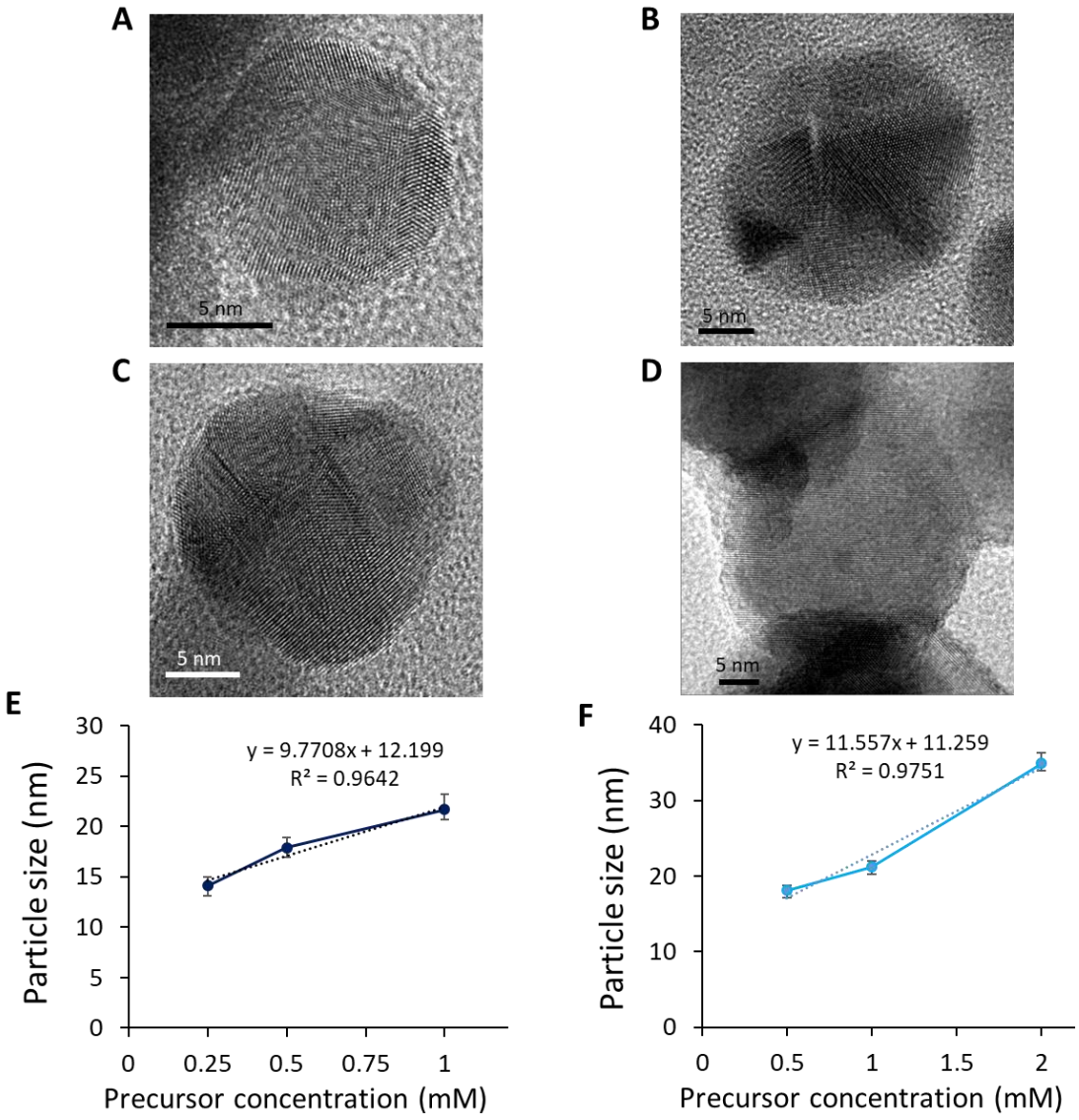

Fig. S46. HR-TEM images of crystalline Ag_2TeO_3 NM synthesized *in vivo* and *in vitro*, and the correlation graphs between particle size and precursor concentration. HR-TEM images of crystalline Ag_2TeO_3 NM synthesized *in vivo* using $AgNO_3$ and Na_2TeO_3 at precursor concentrations of 0.25 and 1 mM each for both elements (*A*, *B*). HR-TEM image obtained with 0.5 mM precursors is shown in Fig. 3*A*. HR-TEM images of the crystalline Ag_2TeO_3 NM synthesized *in vitro* using $AgNO_3$ and Na_2TeO_3 at precursor concentrations of 0.5 and 2 mM each for both elements (*C*, *D*). HR-TEM image obtained with 1 mM precursors is shown in Fig. 3B. The correlation graphs of the crystalline Ag_2TeO_3 NMs synthesized *in vivo* at varying precursor concentrations. (*E*) The sizes of crystalline Ag_2TeO_3 NMs synthesized *in vivo* with corresponding precursors of 0.25 mM each (13.69 ± 0.87 nm), 0.5 mM each (18.90 ± 1.02 nm) and 1 mM each (21.06 ± 1.48 nm), respectively. (*F*) The correlation graphs of the crystalline Ag_2TeO_3 NMs synthesized *in vitro* at varying precursor concentrations. The sizes of crystalline Ag_2TeO_3 NMs synthesized *in vitro* with corresponding precursors of 0.5 mM each (18.1 ± 0.66 nm), 1 mM each (21.21 ± 0.81 nm) and 2 mM each (34.96 ± 1.38 nm), respectively.

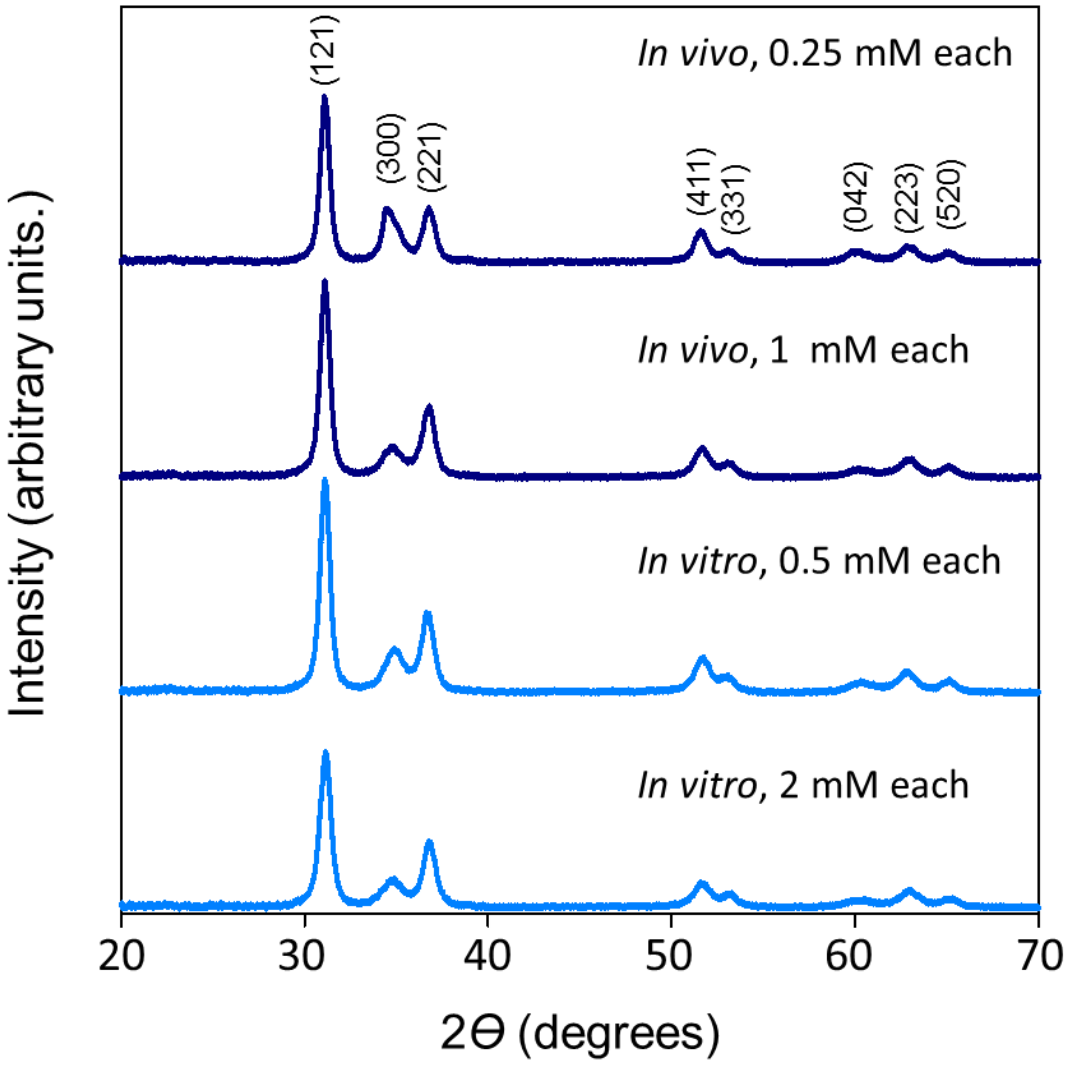

Fig. S47. XRD patterns of the crystalline Ag_2TeO_3 NM synthesized *in vivo* and *in vitro* at varying precursors concentrations. The black numbers in parentheses represent Miller indices corresponding to each scattering peak and matched with JCPDS database (JCPDS card. No. 46-0036). XRD patterns of crystalline Ag_2TeO_3 NM synthesized *in vivo* with the corresponding precursors (0.25 mM each and 1 mM each, respectively) labeled in dark blue line. XRD patterns of crystalline Ag_2TeO_3 NM synthesized *in vitro* with corresponding precursors (0.25 mM each and 1 mM each, respectively) labeled in light blue line.

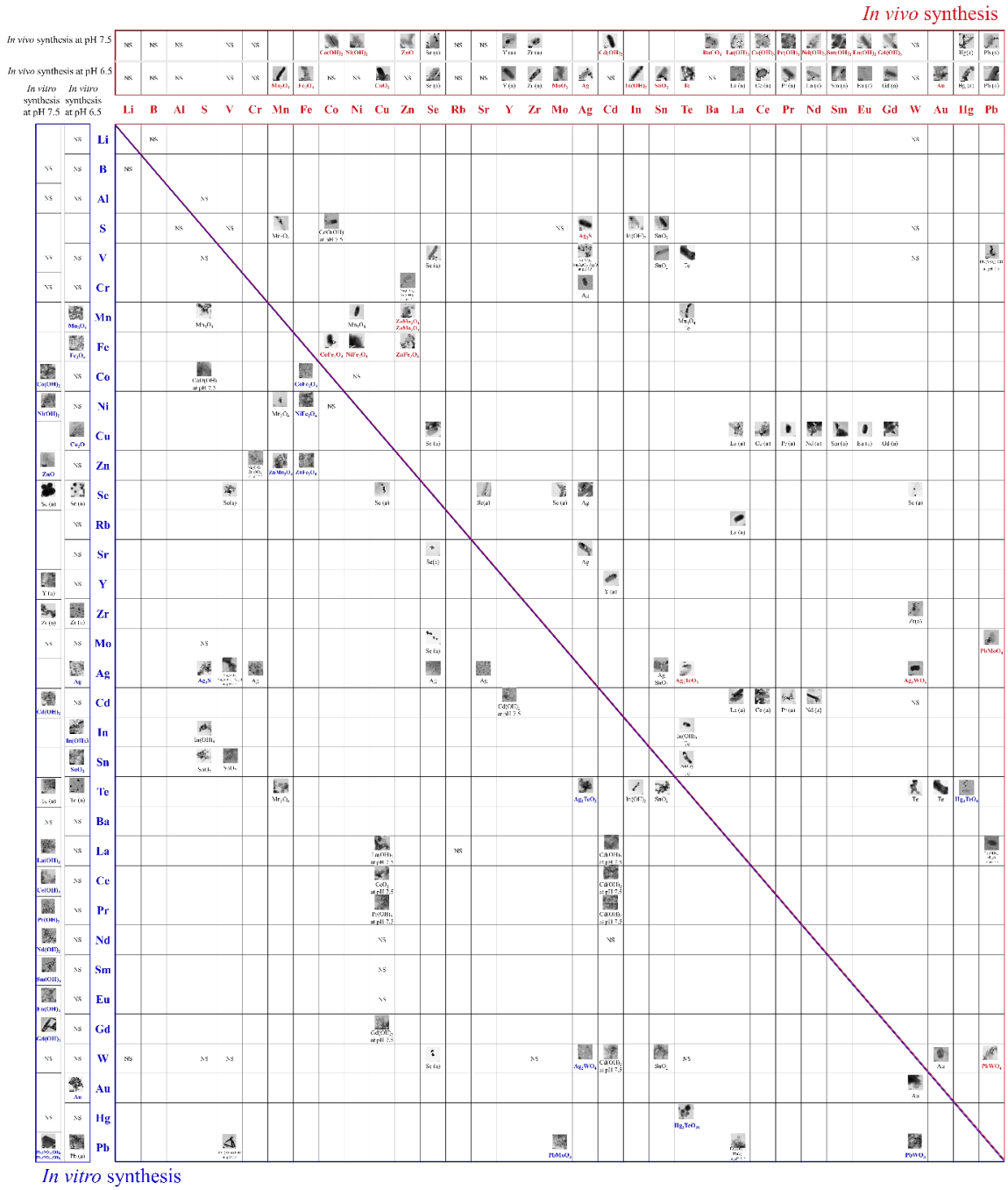

Fig. S48. Summary diagram showing the results of *in vivo* and *in vitro* biosynthesis of various single and multi-element NMs. Single-element NMs synthesized *in vivo* and *in vitro* are shown at the top (in red box) and on the left (in blue box), respectively. Bi-element NMs synthesized *in vivo* and *in vitro* are shown in upper triangle region (with red border) and lower triangle region (with blue border), respectively. NS, No NM synthesis; Amorphous NMs are indicated with (a) next to the element names. A larger image of this figure can be found in Dataset S2.

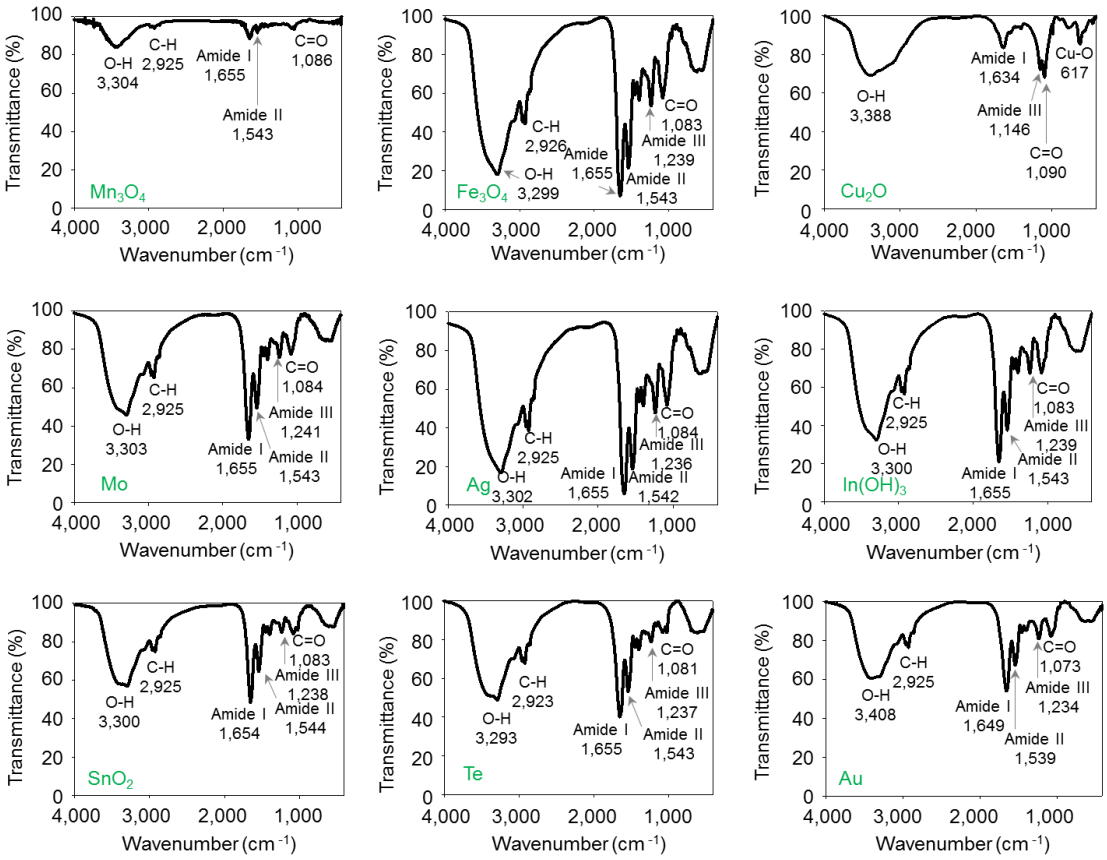

Fig. S49. FTIR graphs of the crystalline NMs synthesized *in vivo*. Numbers in graphs show wavenumbers (cm^{-1}) that correspond to surface functional groups attached to crystalline NMs synthesized *in vivo*.

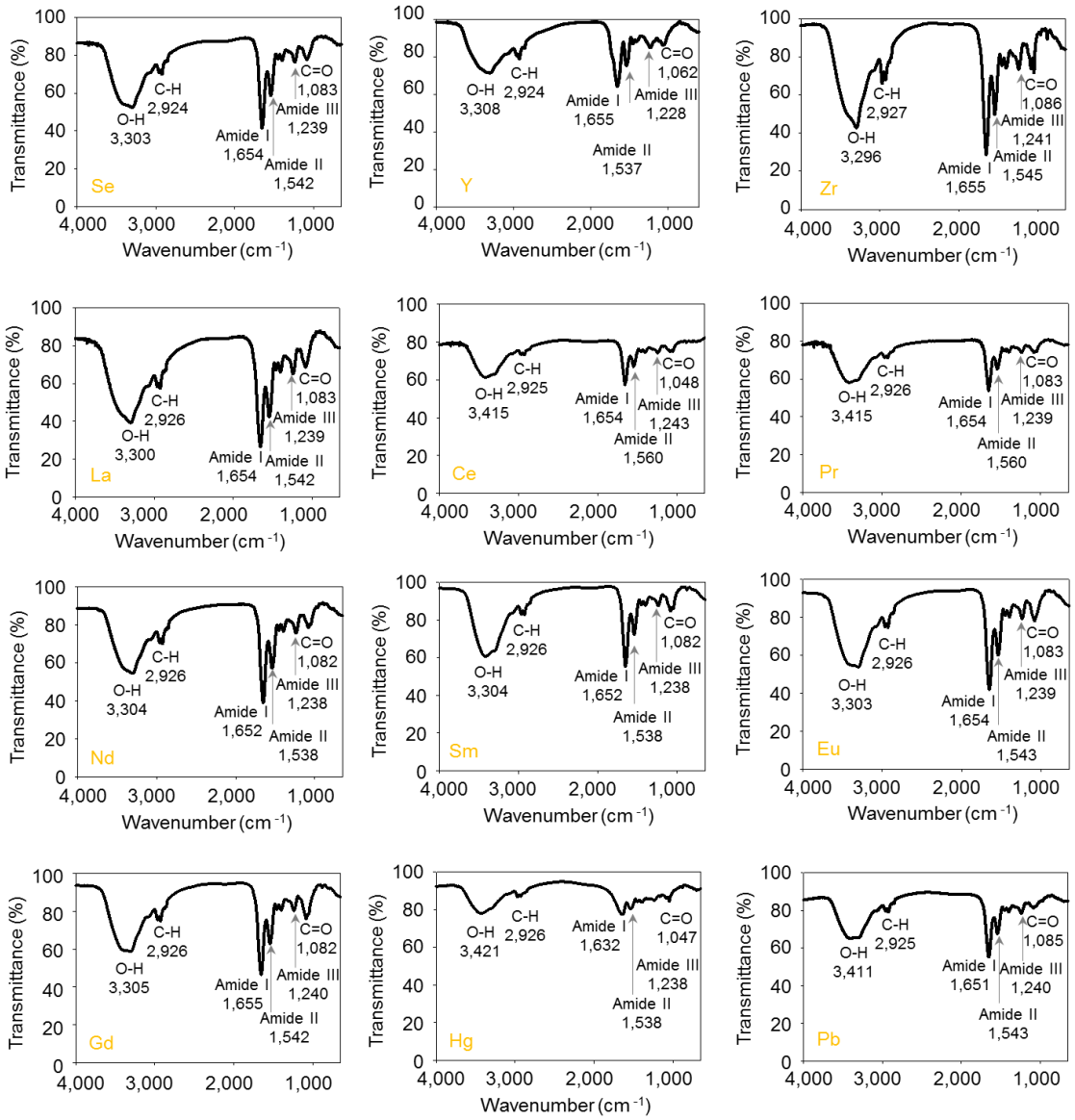

Fig. S50. FTIR graphs of the amorphous NMs synthesized *in vivo*. Numbers in graphs show wavenumbers (cm^{-1}) that correspond to surface functional groups attached to amorphous NMs synthesized *in vivo*.

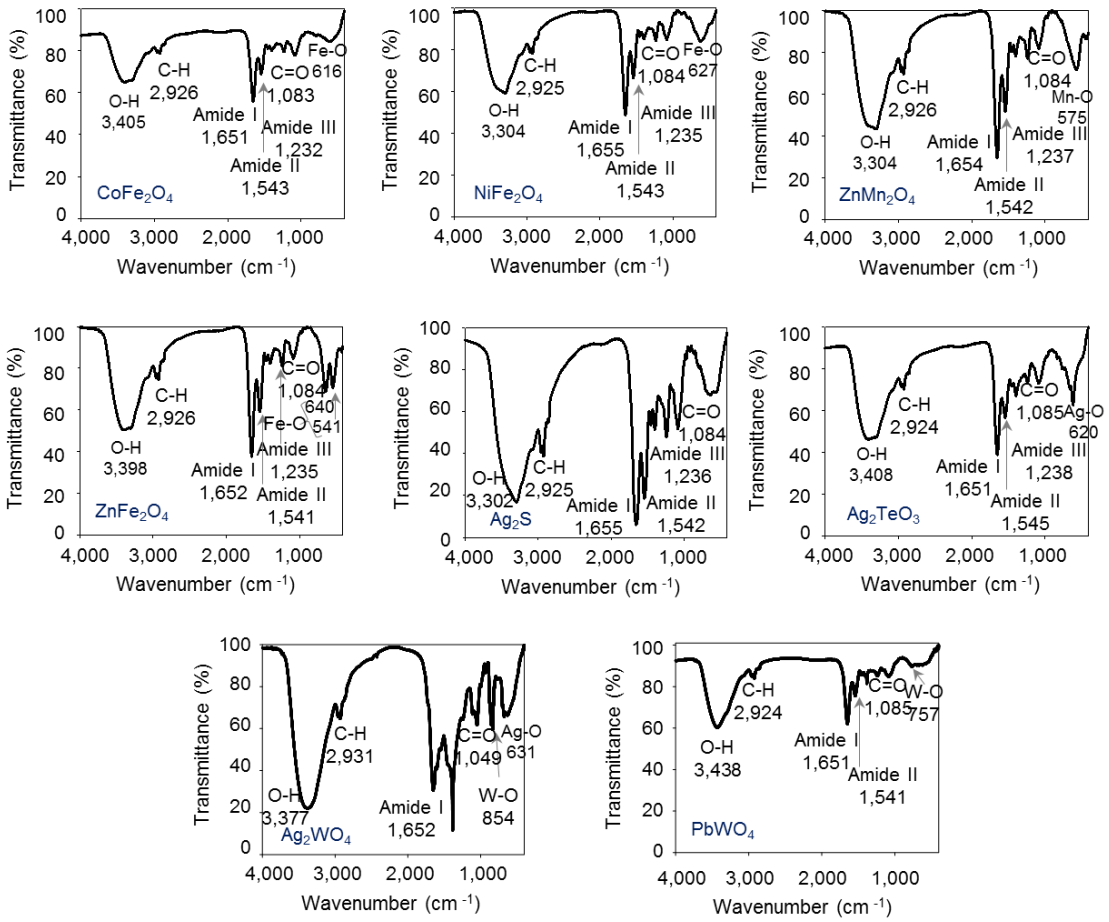

Fig. S51. FTIR graphs of the multi-element crystalline NMs synthesized *in vivo*. Numbers in graphs show wavenumbers (cm^{-1}) that correspond to surface functional groups attached to crystalline multi-element NMs synthesized *in vivo*.

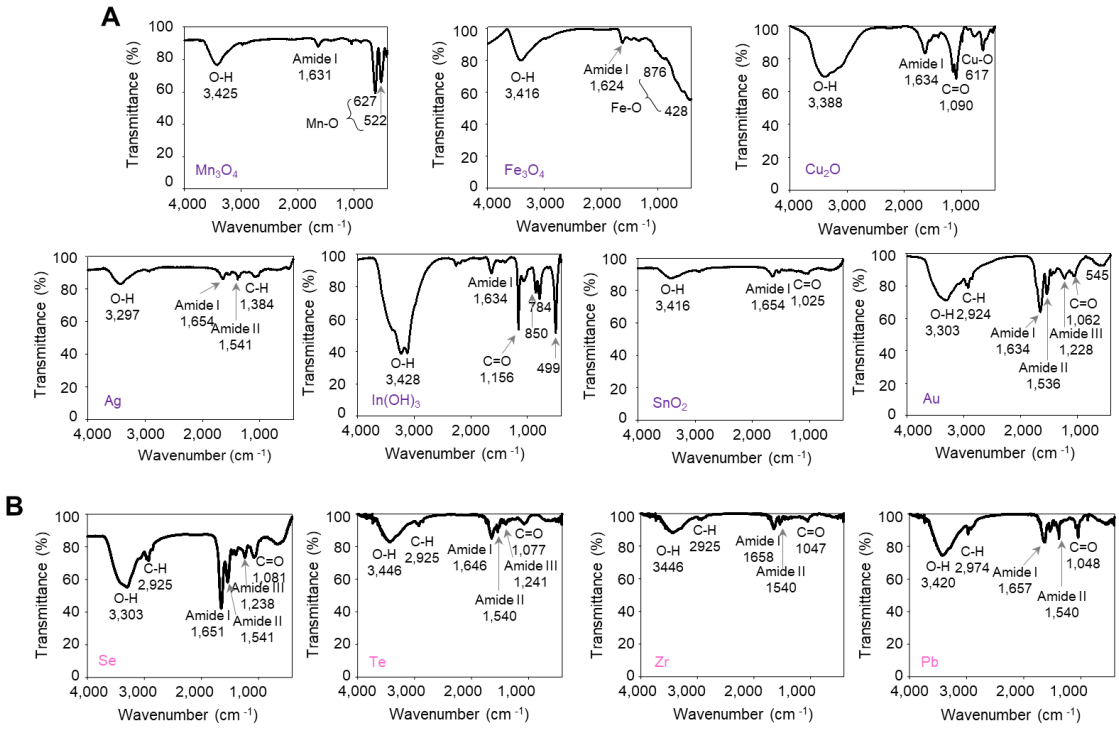

Fig. S52. FTIR graphs of the crystalline and amorphous NMs synthesized *in vitro*. (*A*) FTIR graphs of the crystalline NMs synthesized *in vitro*. Numbers in graphs show wavenumbers (cm^{-1}) that correspond to surface functional groups attached to crystalline NMs synthesized *in vitro*. (*B*) FTIR graphs of the amorphous NMs synthesized *in vitro*. Numbers in graphs show wavenumbers (cm^{-1}) that correspond to surface functional groups attached to amorphous NMs synthesized *in vitro*.

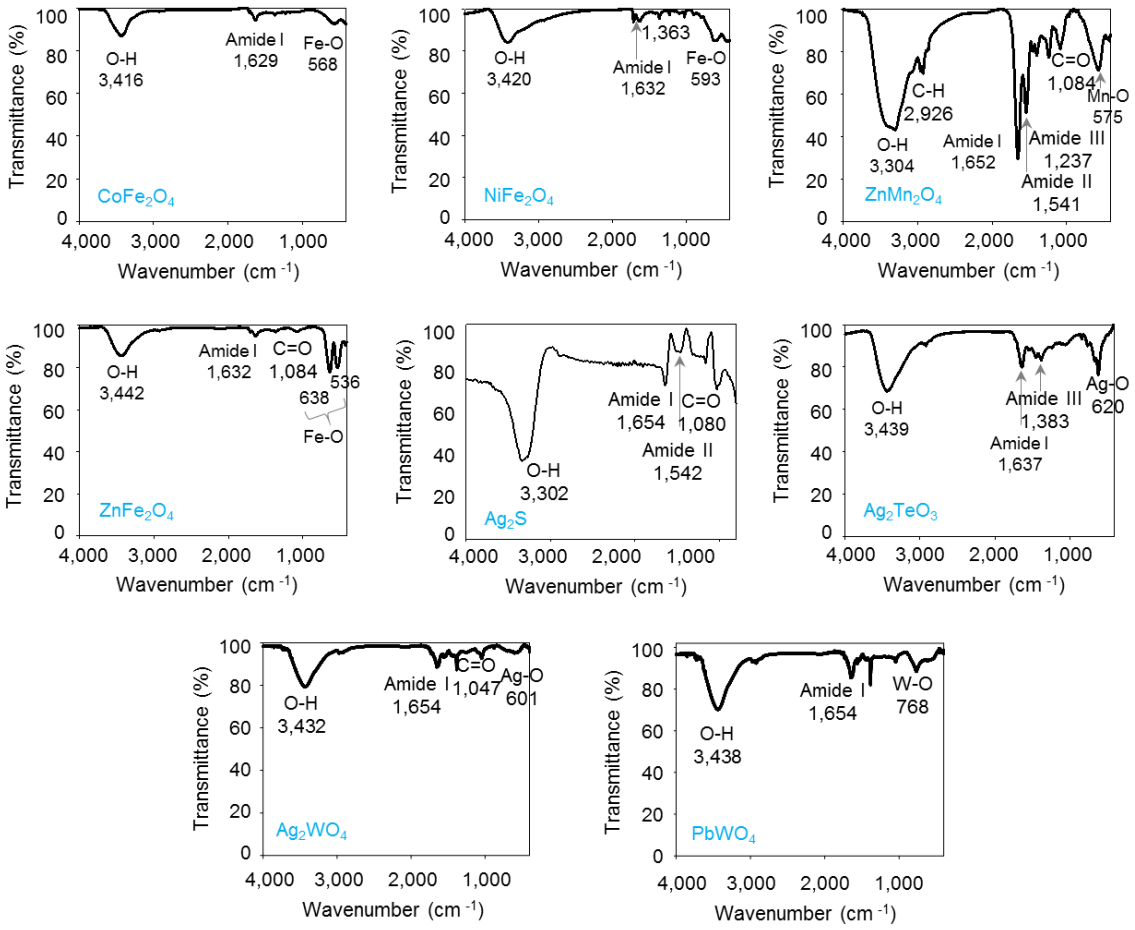

Fig. S53. FTIR graphs of the multi-element crystalline NMs synthesized *in vitro*. Numbers in graphs show wavenumbers (cm^{-1}) that correspond to surface functional groups attached to crystalline multi-element NMs synthesized *in vitro*.

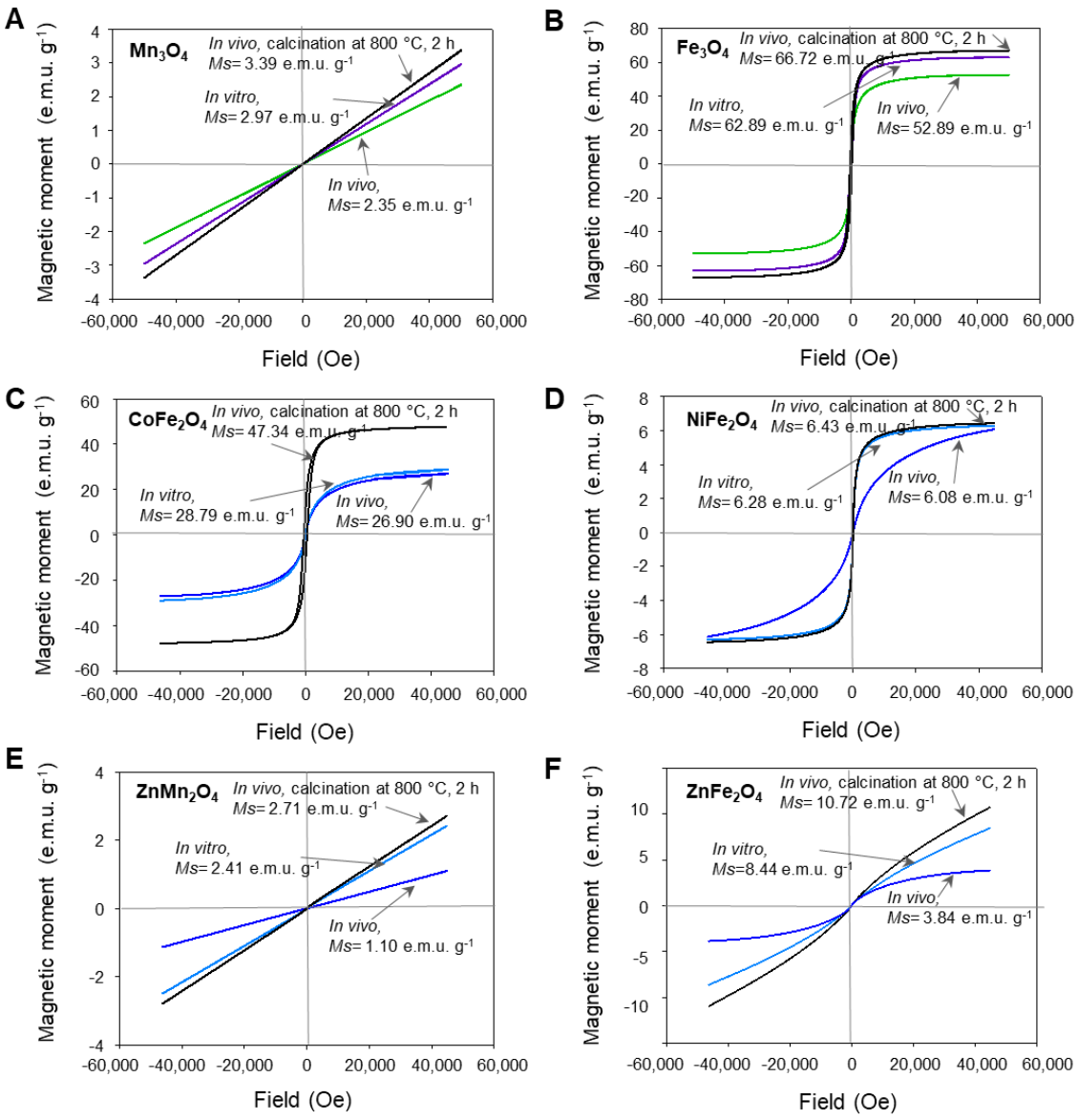

Fig. S54. Magnetic field-dependent magnetization curves (M-H curves) of magnetic NMs synthesized *in vivo* and *in vitro*. M-H curves indicate different magnetic properties of magnetic NMs synthesized *in vivo* and *in vitro*. Magentic moments of crystalline Mn_3O_4 (*A*), Fe_3O_4 (*B*), $CoFe_2O_4$ (*C*), $NiFe_2O_4$ (*D*), $ZnMn_2O_4$ (*E*) and $ZnFe_2O_4$ (*F*) NMs were measured under magnetic field strength of −50,000 to 50,000 Oe at 300 K. Each saturation magnetization (*Ms*) value of the biosynthesized magnetic NM is shown in the graphs.

SI Appendix Tables

Table S1. Bacterial strains and plasmids used in this study

Strains or plasmids	**Relevant characteristics** Abbreviations: Km^r, kanamycin resistance.	**Reference or source**
Strains		
Escherichia coli DH5α	*E. coli* K-12 F^- φ80*lacZ*Δ*M15* Δ(*lacZYA-argF*) U169 *recA1 endA1 hsdR17*($r_k^- m_k^+$) *phoA supE44 thi-1gyrA96 relA1* λ^-	Invitrogen
DH5α-pTac15K	DH5α containing pTac15K, Km^r	This study
YJ-MT-PCS	DH5α containing pYJ-MT-PCS, Km^r	This study
Plasmids		
pTac15K	pACYC177 derivative, p15A origin, *tac* promoter, rrnBT1T2 terminator, Km^r (4.0 kb)	(9)
pYJ-MT	p15A origin, *tac* promoter, rrnB T1 T2 terminator, pTac15K derivative, Km^r, *MT* gene from *Pseudomonas putida* metallothionein (4.2 kb)	This study
pYJ-PCS	p15A origin, *tac* promoter, rrnB T1 T2 terminator, pTac15K derivative, Km^r, *PCS* gene from *Arabidopsis thaliana* ecotype Columbia (leaves) (5.4 kb)	This study
pYJ-MT-PCS	p15A origin, double *tac* promoter, rrnB T1 T2 terminator, pTac15K derivative, Km^r, co-expression of *MT* and *PCS* gene (5.7 kb)	This study

* Abbreviations: Km, Kanamycin; r, resistance.

Table S2. Characteristics of NMs biosynthesized *in vivo* and *in vitro*

***In vivo* synthesized NMs at initial pH 6.5**			
Element	Chemical species	Size (nm)	Shape
Mn	Mn_3O_4	3.93 ± 1.29	Spherical
Fe	Fe_3O_4	4.46 ± 0.27	Spherical
Cu	Cu_2O	17.69 ± 3.23	Spherical
Se	Amorphous	105.25 ± 16.05	Spherical
Y	Amorphous	4.10 ± 0.22	Spherical
Zr	Amorphous	21.78 ± 2.34	Atypical
Mo	MoO_2	20.58 ± 1.70	Rod
Ag	Ag	9.86 ± 1.96	Spherical
In	$In(OH)_3$	3.82 ± 0.33	Spherical
Sn	SnO_2	5.17 ± 0.33	Spherical
Te	Te	35.49 ± 9.16	Rod
La	Amorphous	14.31 ± 1.14	Spherical
Ce	Amorphous	16.18 ± 1.95	Spherical
Pr	Amorphous	14.82 ± 2.03	Spherical
Nd	Amorphous	12.75 ± 1.45	Spherical
Sm	Amorphous	11.16 ± 1.75	Spherical
Eu	Amorphous	15.27 ± 1.35	Spherical
Gd	Amorphous	15.53 ± 1.20	Spherical
Au	Au	20.06 ± 2.27	Spherical
Hg	Amorphous	5.25 ± 0.28	Spherical
Pb	Amorphous	7.04 ± 0.39	Spherical

***In vivo* synthesized NMs at initial pH 7.5**			
Element	Chemical species	Size(nm)	Shape
Co	β-$Co(OH)_2$, Co_3O_4	7.06 ± 0.41	Spherical
Ni	β-$Ni(OH)_2$	25.11 ± 2.67	Rod, Plate
Zn	ZnO	10.51 ± 1.71	Square
Se	Amorphous	187.51 ± 24.34	Atypical
Y	Amorphous	4.55 ± 0.23	Spherical
Zr	Amorphous	2.96 ± 0.12	Atypical
Cd	β-$Cd(OH)_2$	4.16 ± 0.37	Spherical
Ba	$BaCO_3$	5.02 ± 0.15	Spherical
La	$La(OH)_3$	28.99 ± 1.87	Rod
Ce	$Ce(OH)_3$, CeO_2	4.09 ± 0.31	Spherical
Pr	$Pr(OH)_3$	67.44 ± 5.19	Rod
Nd	$Nd(OH)_3$	61.19 ± 4.17	Square
Sm	$Sm(OH)_3$	171.77 ± 15.47	Rod
Eu	$Eu(OH)_3$	6.52 ± 0.93	Rod
Gd	$Gd(OH)_3$	5.49 ± 0.50	Rod
Hg	Amorphous	6.01 ± 0.58	Spherical
Pb	Amorphous	56.15 ± 6.17	Atypical

***In vivo* synthesized Fe NM for 6-hour cultivation**			
Element	Chemical species	Size (nm)	Shape
Fe	α-Fe_2O_3, β-FeOOH, α-FeOOH	9.74 ± 1.19	Spherical

***In vivo* synthesized multi-element crystalline NMs at initial pH 6.5**			
Element	Chemical species	Size (nm)	Shape
Mn, Zn	$ZnMn_2O_4$, $ZnMnO_3$	6.87 ± 0.42	Spherical
Fe, Co	$CoFe_2O_4$	6.83 ± 0.45	Spherical
Fe, Ni	$NiFe_2O_4$, β-FeOOH	6.23 ± 0.54	Spherical
Fe, Zn	$ZnFe_2O_4$	8.45 ± 0.61	Spherical
Mo, Pb	$PbMoO_4$	9.91 ± 0.46	Spherical, Square
Ag, S	Ag_2S	10.93 ± 1.94	Spherical
Ag, Te	Ag_2TeO_3	18.90 ± 1.02	Spherical
Ag, W	Ag_2WO_4	12.67 ± 4.28	Spherical
W, Pb	$PbWO_4$	18.61 ± 3.59	Spherical
Hg, Te	Hg_3TeO_6	14.09 ± 2.74	Spherical

***In vivo* synthesized multi-element crystalline NM at initial pH 7.5**			
Elements	Chemical species	Size (nm)	Shape
V, Pb	$Pb_5(VO_4)_3OH$	9.60 ± 1.46	Spherical

***In vitro* synthesized NMs at initial pH 6.5**			
Element	Chemical species	Size (nm)	Shape
Mn	Mn_3O_4	20.84 ± 1.39	Square
Fe	Fe_3O_4	6.32 ± 1.47	Spherical
Cu	Cu_2O	4.90 ± 0.25	Spherical
Se	Amorphous	93.36 ± 12.05	Spherical
Zr	Amorphous	34.89 ± 3.38	Atypical
Ag	Ag	11.87 ± 2.46	Spherical
In	$In(OH)_3$	31.69 ± 2.85	Square
Sn	SnO_2	7.72 ± 1.41	Spherical
Te	Amorphous	21.58 ± 2.16	Spherical
Au	Au	18.24 ± 3.24	Spherical
Pb	Amorphous	4.94 ± 0.24	Spherical

***In vitro* synthesized NMs at initial pH 7.5**			
Element	Chemical species	Size (nm)	Shape
Co	β-$Co(OH)_2$	4.01 ± 0.37	Spherical
Ni	β-$Ni(OH)_2$	28.28 ± 4.49	Rod, Plate
Zn	ZnO	6.62 ± 0.35	Spherical
Se	Amorphous	447.43 ± 36.32	Atypical
Y	Amorphous	5.36 ± 0.43	Spherical
Zr	Amorphous	6.65 ± 0.41	Atypical
Cd	β-$Cd(OH)_2$	54.71 ± 7.40	Rod
Te	Amorphous	30.71 ± 2.74	Spherical
La	$La(OH)_3$	32.11 ± 1.57	Rod
Ce	CeO_2	32.95 ± 1.81	Rod
Pr	$Pr(OH)_3$	59.25 ± 5.30	Rod
Nd	$Nd(OH)_3$	80.58 ± 2.63	Rod
Sm	$Sm(OH)_3$	173.83 ± 4.53	Rod
Eu	$Eu(OH)_3$	6.89 ± 0.57	Rod
Gd	$Gd(OH)_3$	1,794.08 ± 21.02	Rod
Pb	$Pb_3(NO)_3(OH)_5$, $Pb_2(NO)_3(OH)_3$	204.57 ± 43.86	Plate

***In vitro* synthesized Fe NM for 6-hour incubation**			
Element	Chemical species	Size (nm)	Shape
Fe	α-Fe_2O_3, β-FeOOH, α-FeOOH	10.38 ± 2.04	Spherical

***In vitro* synthesized multi-element crystalline NMs at initial pH 6.5**			
Element	Chemical species	Size (nm)	Shape
Mn, Zn	$ZnMn_2O_4$	9.28 ± 0.47	Spherical
Fe, Co	$CoFe_2O_4$	7.69 ± 0.51	Spherical
Fe, Ni	$NiFe_2O_4$, β-FeOOH	7.45 ± 1.07	Spherical
Fe, Zn	$ZnFe_2O_4$	8.75 ± 0.53	Spherical
Mo, Pb	$PbMoO_4$	13.01 ± 1.28	Spherical, Square
Ag, S	Ag_2S	13.47 ± 1.21	Spherical
Ag, Te	Ag_2TeO_3	21.21 ± 0.81	Spherical
Ag, W	Ag_2WO_4	7.56 ± 1.02	Spherical
W, Pb	$PbWO_4$	42.38 ± 4.81	Spherical
Hg, Te	Hg_3TeO_6	42.71 ± 13.80	Spherical

***In vitro* synthesized multi-element crystalline NM at initial pH 7.5**			
Elements	Chemical species	Size (nm)	Shape
V, Pb	$Pb_5(VO_4)_3OH$	1318.31 ± 171.05	Rod

Table S3. Oligo nucleotides used for PCR amplification in this study

Primers	Sequences*(5'→3')
P1	ATAGAATTCATGAACGATCAACGCTGCGC
P2	TATCTGCAGTCAGGGCGAGATCGGATCACTC
P3	ATAGAATTCATGGCTATGGCGAGTTTATATCGG
P4	TATGCATGCTTAATAGGCAGGAGCAGCGAGATC
P5	ATACTGCAGTTGACAATTAATCATCGGCTCGTATA
P6	TATGCATGCTTAATAGGCAGGAGCAGCGAGA

*Underlines indicate restriction enzyme sites.

Table S4. List of classified chemical types as the precursors for NM synthesis

No.	Elements	Elements category	Chemical types
1	Li	Alkali metal	$CH_3COOLi{\cdot}2H_2O$
2	B	Metalloid	H_3BO_3
3	Al	Post-transition metal	$AlCl_3{\cdot}6H_2O$
4	S	Nonmetal	Na_2S
5	V	Transition metal	$NaVO_3$
6	Cr	Transition metal	$CrCl_3{\cdot}6H_2O$
7	Mn	Transition metal	$MnCl_2{\cdot}4H_2O$
8	Fe	Transition metal	$FeCl_2{\cdot}6H_2O$
9	Co	Transition metal	$CoCl_2{\cdot}6H_2O$
10	Ni	Transition metal	$NiCl_2{\cdot}6H_2O$
11	Cu	Transition metal	$CuCl_2{\cdot}2H_2O$
12	Zn	Transition metal	$ZnSO_4{\cdot}7H_2O$
13	Se	Diatomic nonmetal	Na_2SeO_3
14	Rb	Alkali metal	$RbCl_2$
15	Sr	Alkali earth metal	$Sr(NO_3)_2$
16	Y	Transition metal	$Y(NO_3)_3{\cdot}6H_2O$
17	Zr	Transition metal	K_2ZrF_6
18	Mo	Transition metal	$Na_2MoO_4{\cdot}2H_2O$
19	Ag	Transition metal	$AgNO_3$
20	Cd	Transition metal	$CdCl_2$
21	In	Post-transition metal	$InCl_2{\cdot}4H_2O$
22	Sn	Post-transition metal	$SnCl_2{\cdot}2H_2O$
23	Te	Metalloid	Na_2TeO_3
24	Ba	Alkali earth metal	$Ba(CH_3COO)_2$
25	La	Lanthanide	$La(NO_3)_3{\cdot}6H_2O$
26	Ce	Lanthanide	$Ce(NO_3)_3{\cdot}6H_2O$
27	Pr	Lanthanide	$Pr(NO_3)_3{\cdot}6H_2O$
28	Nd	Lanthanide	$Nd(NO_3)_3{\cdot}6H_2O$
29	Sm	Lanthanide	$Sm(NO_3)_3{\cdot}6H_2O$
30	Eu	Lanthanide	$Eu(NO_3)_3{\cdot}6H_2O$
31	Gd	Lanthanide	$GdNO_3)_3{\cdot}6H_2O$
32	W	Transition metal	$Na_2WO_4{\cdot}6H_2O$
33	Au	Transition metal	$HAuCl_4$
34	Hg	Transition metal	$HgCl_2$
35	Pb	Post-transition metal	$Pb(NO_3)_2$

SI Appendix Text

SI Appendix Text S1. Comparison of biosynthesis of NMs using bacteria and plant extracts. The use of bacteria is better than using plant extract as the latter requires strong acids and heat for the preparation of the extract and additional reducing agents (i.e., sodium borohydride) for the supply of reducing power.

SI Appendix Text S2. Previous study on biosynthesis of various NMs using recombinant *E. coli* co-expressing MT and PCS. For the production of more various NMs by bacterial system, we previously developed a recombinant *E. coli* strain co-expressing MT and PCS, which allowed biosynthesis of noble NMs (Ag and Au), magnetic NMs (Fe, FeMn, FeCo, FeCoMn, FeCoNi and FeAg), quantum dots (QDs; ZnSe, CdZn, CdSe, CdSeZn, CdSeZnTe, CdTe, CdCs, PrGd, SrPr, SrGd, EuSe and AuCdSeZn) and metalloid NM (Te) upon addition of the corresponding precursors during the cultivation (8, 10, 11).

SI Appendix Text S3. Expression of MT and PCS in *E. coli* DH5α strain during the NMs synthesis. Expression of MT and PCS in *E. coli* was already investigated in the previous study (7). We further examined the changes of expression levels of the proteins over the time. MT is not visible due to its small size (~7.9 kDa) in the SDS-PAGE. The expression of PCS (~54.5 kDa) increased gradually up to 8 h after induction in the presence of Sn precursor, whereas it showed a slight decrease at 12 h after induction. In the culture supernatant, PCS was not observed in 16 h cultivation, suggesting that there was no leakage of PCS at least.

SI Appendix Text S4. *In vitro* synthesis of single-element NMs. Seven crystalline NMs synthesized *in vitro* were Mn_3O_4, Fe_3O_4, Cu_2O, Ag, $In(OH)_3$, SnO_2 and Au (Fig. 1*G*, *SI Appendix*, Figs. S7 and S8); the crystal structures of these NMs reconstructed based on the XRD data are shown in *SI Appendix*, Fig. S4. On the other hand, amorphous NMs were formed *in vitro* for Se, Zr, Te and Pb (Fig.1*H* and *SI Appendix*, Fig. S9). The other 23 elements, including Li, B, Al, V, Cr, Co, Ni, Zn, Rb, Sr, Y, Mo, Cd, Ba, La, Ce, Pr, Nd, Sm, Eu, Gd, W and Hg, resulted in no NM formation *in vitro*. Interestingly, seven lanthanide elements (La, Ce, Pr, Nd, Sm, Eu and Gd) tested all led to the formation of amorphous NMs *in vivo*, but no NM formation *in vitro*. *In vitro* synthesis of Mn, Ag and Sn NMs using the cell extract of the control *E. coli* strain harboring an empty vector resulted in crystalline Mn_3O_4, Ag and SnO_2 NMs, but again they were heterogeneous in size and shape (Fig. 1*I*), as observed above for *in vivo* biosynthesis.

SI Appendix Text S5. Pourbaix diagram analysis to predict NMs producibility. The Eh and pH values were measured during the *in vivo* syntheses of NMs for 12 h for each element, and the stability and predominant forms of elements were studied through Pourbaix diagram analyses (*SI Appendix*, Figs. S11-S13 and see *SI Appendix*, *Materials and Methods*). During the *in vivo* synthesis of NMs, Eh values decreased from +351.1~+356.4 mV to −182.2~−463.6 mV while the pH increased from 6.50 to 7.13~8.23. The results of Pourbaix diagram analyses were consistent with the *in vivo* experimental results; NM biosynthesis of correct product for 21 elements was confirmed (*SI Appendix*, Figs. S11 and S12).

SI Appendix Text S6. Pourbaix diagram analyses and measurements of the Eh and pH during *in vitro* biosynthesis. For *in vitro* synthesis of NMs, the Eh decreased from +349.4~+351.2 mV to −280.5~−445.2 mV and pH increased from 6.50 to 7.13~8.72 during the 12 h incubation (*SI Appendix*, Figs. S14-S16). As in the case of *in vivo* NM biosynthesis, the results of Pourbaix diagram analyses were consistent with the *in vitro* experimental results as well: among 34 elements examined, NM synthesis from 11 elements (*SI Appendix*, Figs. S14 and S15) and no NM synthesis from 14 elements are recapitulated in the Pourbaix diagram analysis (*SI Appendix*, Fig. S16). However, no NM synthesis from nine elements (B, Al, V, Cr, Y, Mo, Sm, Eu and Gd) are unexplainable using Pourbaix diagram.

SI Appendix Text S7. Two separate single-element crystalline NMs synthesized *in vivo* at pH 7.5. In the case of Co and Ce, two separate single-element crystalline NMs were synthesized *in vivo* at pH 7.5: β-$Co(OH)_2$ and Co_3O_4; $Ce(OH)_3$ and CeO_2 (*SI Appendix*, Fig. S19*B*). For the former case, it has been reported that chemical synthesis of Co NM resulted in the formation of thermodynamically less stable α-$Co(OH)_2$, which is rapidly converted to β-$Co(OH)_2$ (12). Then, β-$Co(OH)_2$ is gradually transformed into Co_3O_4, resulting in the detection of only β-$Co(OH)_2$ and Co_3O_4, but no α-$Co(OH)_2$ by XRD analysis. For the latter case, Pourbaix diagram analysis indicates that the *in vivo* biosynthesis condition is initially favorable for the formation of CeO_2 and gradually shifts to a condition favorable for the formation of $Ce(OH)_3$ (*SI Appendix*, Fig. S17).

SI Appendix Text S8. Formation of crystalline NMs or amorphous NMs, or no NM formation *in vitro* at pH 7.5. Li, Rb, Sr and W (*SI Appendix*, Fig. S16) were excluded due to the same reason described for *in vivo* reactions. Pourbaix diagrams of 23 elements, that did not form crystalline NMs at pH 6.5, were analyzed and the Eh and pH of *in vitro* reactions were mapped (*SI Appendix*, Figs. S22 and S23). By raising the pH of *in vitro* reactions to 7.5 for 12 h, 11 crystalline NMs were synthesized as their predicted crystalline phases: β-$Co(OH)_2$, β-$Ni(OH)_2$, ZnO, β-$Cd(OH)_2$, $La(OH)_3$, CeO_2, $Pr(OH)_3$, $Nd(OH)_3$, $Sm(OH)_3$, $Eu(OH)_3$ and $Gd(OH)_3$ (Fig. 2*D*, *SI Appendix*, Figs. S25 and S27); the crystal structures of these NMs reconstructed based on the XRD data are shown in *SI Appendix*, Fig. S27. It should be noted that abrupt change of the initial pH to 7.5 caused appearance of some precipitates (i.e., Ni, Zn, Nd, and Sm) in 30 min (*SI Appendix*, Fig. S24), which seemed to grow to crystalline NMs after prolonged reaction for 12 h. In the case of Pb, the Pourbaix diagram predicted formation of $Pb(OH)_2$, but $Pb_3(NO)_3(OH)_5$ and $Pb_2(NO)_3(OH)_3$ NMs were synthesized *in vitro*. For Se, Y, Zr and Te, amorphous NMs were synthesized by *in vitro* reaction at pH 7.5 (Fig. 2*E* and *SI Appendix*, Fig. 28). In the cases of B, Al, V, Cr, Mo and Ba, NMs were not synthesized by *in vitro* reactions even at pH 7.5 (*SI Appendix*, Fig. S23*B*).

SI Appendix Text S9. Amorphous NMs synthesized *in vivo* and *in vitro* at pH 7.5. It was previously reported that biosynthesized Se NM is typically amorphous under ambient conditions (10). In the case of Y, $Y(OH)_3$ crystalline NM could be obtained by increasing the initial pH higher than 13 under hydrothermal precipitation methods (11). However, amorphous Y NM was synthesized *in vivo* and *in vitro* at initial pH 7.5 (Fig. 2*C*, *E*). For

Mo and Ba, the Pourbaix diagram predicted biosynthesis of crystalline MoO_2 and $BaCO_3$ by both *in vivo* and *in vitro* reactions, but only *in vivo* reaction resulted in their biosynthesis in our experiments (*SI Appendix*, Fig. S23*B*). For these several elements, further studies are needed to better understand the mechanisms underlying the formation of NMs with respect to crystallinity and producibility.

SI Appendix Text S10. α-Fe_2O_3 NM synthesized *in vivo* and *in vitro* by 6-hour reaction. Biosynthesis of α-Fe_2O_3 NM was accompanied with generation of two byproducts β-FeOOH and α-FeOOH (*SI Appendix*, Figs. S30*A*-*D* and S31*A*-*F*). To obtain only α-Fe_2O_3 NM without the byproducts, the mixture of α-Fe_2O_3, β-FeOOH and α-FeOOH was calcinated at 800°C in the presence of air for 2 h. The resulting α-Fe_2O_3 NMs synthesized *in vivo* and *in vitro* showed different sizes of 12.27 ± 3.37 nm and 14.68 ± 4.97 nm, respectively; the crystalline structure was reconstructed based on the XRD data (*SI Appendix*, Figs. S30*E*-*H* and S31*G*-*K*).

SI Appendix Text S11. Formation of single crystalline NMs or amorphous NMs, or no NM formation *in vivo* for those elements that were predicted to form crystalline multi-element NMs. Although the Pourbiax diagram analysis predicted possibility of synthesizing nine crystalline NMs for $Ag_3H_2VO_5$, Ag_2Se, $Pb_2V_2O_7$, Cu_2Se, $SrSeO_3$, $Al_4(OH)_{10}SO_4$, $ZnCr_2O_4$, CoS and MoS_2 by *in vivo* biosynthesis (*SI Appendix*, Fig. S32), single crystalline Ag NM was synthesized for V/Ag and Se/Ag combinations (*SI Appendix*, Fig. S37*A*), single amorphous Pb NM was synthesized for V/Pb combination, and single amorphous Se NM was synthesized for Cu/Se and Se/Sr combinations (*SI Appendix*, Fig.

S37*B*). The other four bi-elemental combinations (Al/S, S/Co, S/Mo and Cr/Zn) resulted in no *in vivo* NM biosynthesis.

SI Appendix Text S12. Fourty-two bi-elemental combinations to biosynthesize multi-element crystalline NMs. We examined producibility of the folloing 42 bi-elemental combinations: magnetic NMs including Mn/Ni, Mn/Zn and Co/Ni; heavy metal free QDs including S/Mn, S/In, S/Sn, S/W, Mn/Te, Se/Mo, Ag/Te, In/Te, Sn/Te and Te/Hg; and various randomly selected NMs including Li/B, Li/W, S/V, V/Se, V/Sn, V/Pb, Cr/Ag, Cu/La, Cu/Ce, Cu/Pr, Cu/Nd, Cu/Sm, Cu/Eu, Cu/Gd, Se/W, Rb/La, Sr/Ag, Y/Cd , Zr/W, Ag/Sn, Cd/La, Cd/Ce, Cd/Pr, Cd/Nd, Cd/W, Sn/W, Te/Au, La/Pb and W/Au (*SI Appendix*, Fig. S34)

SI Appendix Text S13. Formation of single crystalline NMs or amorphous NMs, or no NM formation *in vivo* for those elements that were predicted not to form multi-element NMs. For the five bi-elemental combinations, including Mn/Te, Ag/Sn, In/Te, Sn/Te and La/Pb, two separate NMs (e.g., Mn NM and Te NM for Mn/Te) were biosynthesized (*SI Appendix*, Fig. S37*C*). Six combinations including Li/B, Li/W, S/V, S/W, Co/Ni and Cd/W produced no *in vivo* NM synthesis. The other 28 bi-elemental combinations resulted in biosynthesis of NMs of only one element (*SI Appendix*, Figs. S34*C* and S37*D*). In single element experiments shown above, lanthanides including Y, La, Ce, Pr, Gd, Nd, Sm and Eu formed amorphous NMs. Bi-element combinations including these lanthanides resulted in formation of single lanthanide amorphous NMs. Two elements, V and Rb, which did not form NMs in bi-element experiments as observed

in single-element experiments. Although Se and Pb formed amorphous NMs while Cd and W did not form NMs in single-element experiments, they formed multi-element crystalline NMs as in Ag_2WO_4, CdSe, $PbMoO_4$ and $PbWO_4$. When bi-element NM biosynthesis involving Cu and lanthanides such as Cu/La, Cu/Ce, Cu/Pr, Cu/Gd, Cu/Nd, Cu/Sm and Cu/Eu was performed, it was interesting to observe that single amorphous lanthanide NMs without crystalline Cu_2O NM were formed. Further studies are needed to understand the mechanisms underlying these phenomena.

SI Appendix Text S14. Formation of single crystalline or amorphous NMs, two separate single-element NMs, or no NM synthesized *in vitro*. Single crystalline Ag NM was biosynthesized for V/Ag and Se/Ag combinations (*SI Appendix*, Fig. S40*A*), only single amorphous Pb NM for V/Pb combination, and single amorphous Se NM for Cu/Se and Se/Sr combinations (*SI Appendix*, Fig. S40*B*); these results are the same as those observed in *in vivo* experiments. In the case of Ag/Sn combination, two separate single-element NMs were *in vitro* synthesized as observed in *in vivo* experiment (*SI Appendix*, Fig. S40*C*). In the cases of combinations including Te element (i.e. Mn/Te, In/Te and Sn/Te), single crystalline Mn_3O_4, $In(OH)_3$ and SnO_2 NMs without single Te NM formation (*SI Appendix*, Fig. S40*D*), which are different from *in vivo* biosynthesis results. The other 19 combinations resulted in no *in vitro* NM synthesis. Among these, no NM formation for 10 combinations (i.e. S/V, S/Mo, Co/Ni, Rb/La, Cd/Y, Cd/La, Cd/Ce, Cd/Pr, Cd/Nd and La/Pb) is consistent with that observed in *in vitro* single elemental screening results. Differently from *in vivo* biosynthesis experiments, no NM was *in vitro* synthesized for bi-

elemental combinations of Cu and lanthanides, while Cu_2O crystalline NM was *in vitro* biosynthesized when only Cu was present.

SI Appendix Text S15. Multi-element NMs synthesized *in vivo* and *in vitro* at pH 7.5. In the four case of S/Co, Se/Ag, Cu/Se and Se/Sr bi-elemental combinations, single crystalline NMs, including CoO(OH) and Ag (*SI Appendix*, Figs. S41*A* and S43*A*) and single amorphous Se NM were biosynthesized (*SI Appendix*, Fig. S43*B*). For Ag/Sn and La/Pb, two individual NMs were *in vitro* synthesized in both cases (*SI Appendix*, Fig. S42*C*). For most of the bi-elemental combinations tested *in vivo* and *in vitro,* single NMs were biosynthesized even at pH 7.5 (*SI Appendix*, Figs. S41*C* and S42*D*). For V/Ag, crystalline $NaVO_2$, $NaAg_3O_2$ and Ag_2O NMs were biosynthesized both *in vivo* and *in vitro* at pH 7.5 (*SI Appendix*, Fig. S43*A*-*E*), differently from formation of single crystalline Ag NM at pH 6.5 (*SI Appendix*, Figs. S37*A* and S40*A*). For Cr/Zn, crystalline Na_4CrO_4 and $Zn(OH)_2$ NMs were produced at pH 7.5 (*SI Appendix*, Fig. S43*F*-*J*) while no NM biosynthesis was observed at pH 6.5. For V/Pb combination, crystalline $Pb_5(VO_4)_3OH$ NM was biosynthesized at pH 7.5, although solid phase $Pb_3(VO_4)_2$ or $Pb_2V_2O_7$ were predicted by Pourbaix diagram analysis (*SI Appendix*, Figs. S36*D*, S36*E* and S44). No NM was biosynthesized for Al/S and S/Mo at pH 7.5, although the Pourbaix diagram predicted formation of $Al_4(OH)_{10}SO_4$ and MoS_2 (*SI Appendix*, Fig. S32).

SI Appendix Text S16. Magnetic properties of the crystalline NMs synthesized *in vivo* after calcination. For *in vivo* biosynthesized NMs, the magnetic properties were measured with the centrifuged samples containing NMs as well as cell debris co-precipitated. When

using the *in vitro* method, the supernatant of centrifuged cell lysate was used for NM biosynthesis, and thus no cell debris was present. After cell debris of *in vivo* synthesized magnetic NMs were removed by calciation at 800 °C, the NMs showed paramagnetic (Mn_3O_4 and $ZnMn_2O_4$), ferromagnetic (Fe_3O_4 and $CoFe_2O_4$) and superparamagnetic ($NiFe_2O_4$ and $ZnFe_2O_4$) properties (black lines in *SI Appendix*, Fig. S54).

References

1. Sambrook J, Fritsch EF, Maniatis T (1989) *Molecular cloning: a laboratory manual* (Cold spring harbor laboratory press).
2. Mitchell DR (2008) DiffTools: electron diffraction software tools for DigitalMicrograph. *Microsc Res Tech* 71(8):588-593.
3. Schägger H (2006) Tricine-SDS-PAGE. *Nat Protoc* 1:16-22.
4. Hydra/Medusa chemical equilibrium database and plotting software, (http://www.kth.se/che/medusa/downloads-1.386254, Accessed: April 11, 2018).
5. Takahashi M, Takano M, Asada K (1981) Tris-induced cross-linking of thylakoid peptides; thiol oxidation catalyzed by Tris-Cu^{2+} complexes as a possible mechanism. *J Biochem* 90:87-94.
6. Kitayaporn S, Zhou W, Schwartz DT, Baneyx F (2012) Laying out ground rules for protein-aided nanofabrication: ZnO synthesis at 70°C as a case study. *Biotechnol Bioeng* 109:1912-1918.
7. Seo JM, Kim EB, Hyun MS, Kim BB, Park TJ (2015) Self-assembly of biogenic gold nanoparticles and their use to enhance drug delivery into cells. *Colloids Surf B* 135:27-34.
8. Park TJ, Lee SY, Heo NS, Seo TS (2010) *In vivo* synthesis of diverse metal nanoparticles by recombinant *Escherichia coli*. *Angew Chem Int Ed 49:7019-7024.*
9. Lee SY, et al. (2008) Recombinant microorganism having an ability of using sucrose as a carbon source. *US patent* 20110269183.
10. Wadhwani SA, Shedbalkar UU, Singh R, Chopade BA (2016) Biogenic selenium nanoparticles: current status and future prospects. *Appl Microbiol Biotechnol* 100:2555-2566.
11. Shiba F, Tamagawa T, Kojima T, Okawa Y (2013) Hydrothermal synthesis of one-dimensional yttrium hydroxide particles by a two-step alkali-addition method. *CrystEngComm* 15:1061-1067.
12. Huang Z, et al. (2016) Study on the oxidation process of cobalt hydroxide to cobalt oxides at low temperatures. *RSC Adv* 6:80059-80064.